

FILE COPY

LIST
87448

1 of 2 cys.

2

Solid State Research

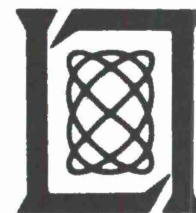
1977

Prepared
under Electronic Systems Division Contract F19628-76-C-0002 by

Lincoln Laboratory

MASSACHUSETTS INSTITUTE OF TECHNOLOGY

LEXINGTON, MASSACHUSETTS



Approved for public release; distribution unlimited.

ADA044795

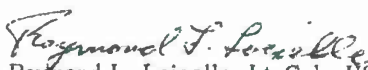
The work reported in this document was performed at Lincoln Laboratory, a center for research operated by Massachusetts Institute of Technology, with the support of the Department of the Air Force under Contract F19628-76-C-0002.

This report may be reproduced to satisfy needs of U.S. Government agencies.

The views and conclusions contained in this document are those of the contractor and should not be interpreted as necessarily representing the official policies, either expressed or implied, of the United States Government.

This technical report has been reviewed and is approved for publication.

FOR THE COMMANDER


Raymond L. Loiselle, Lt. Col., USAF
Chief, ESD Lincoln Laboratory Project Office

Non-Lincoln Recipients

PLEASE DO NOT RETURN

Permission is given to destroy this document
when it is no longer needed.

MASSACHUSETTS INSTITUTE OF TECHNOLOGY
LINCOLN LABORATORY

SOLID STATE RESEARCH

QUARTERLY TECHNICAL SUMMARY REPORT

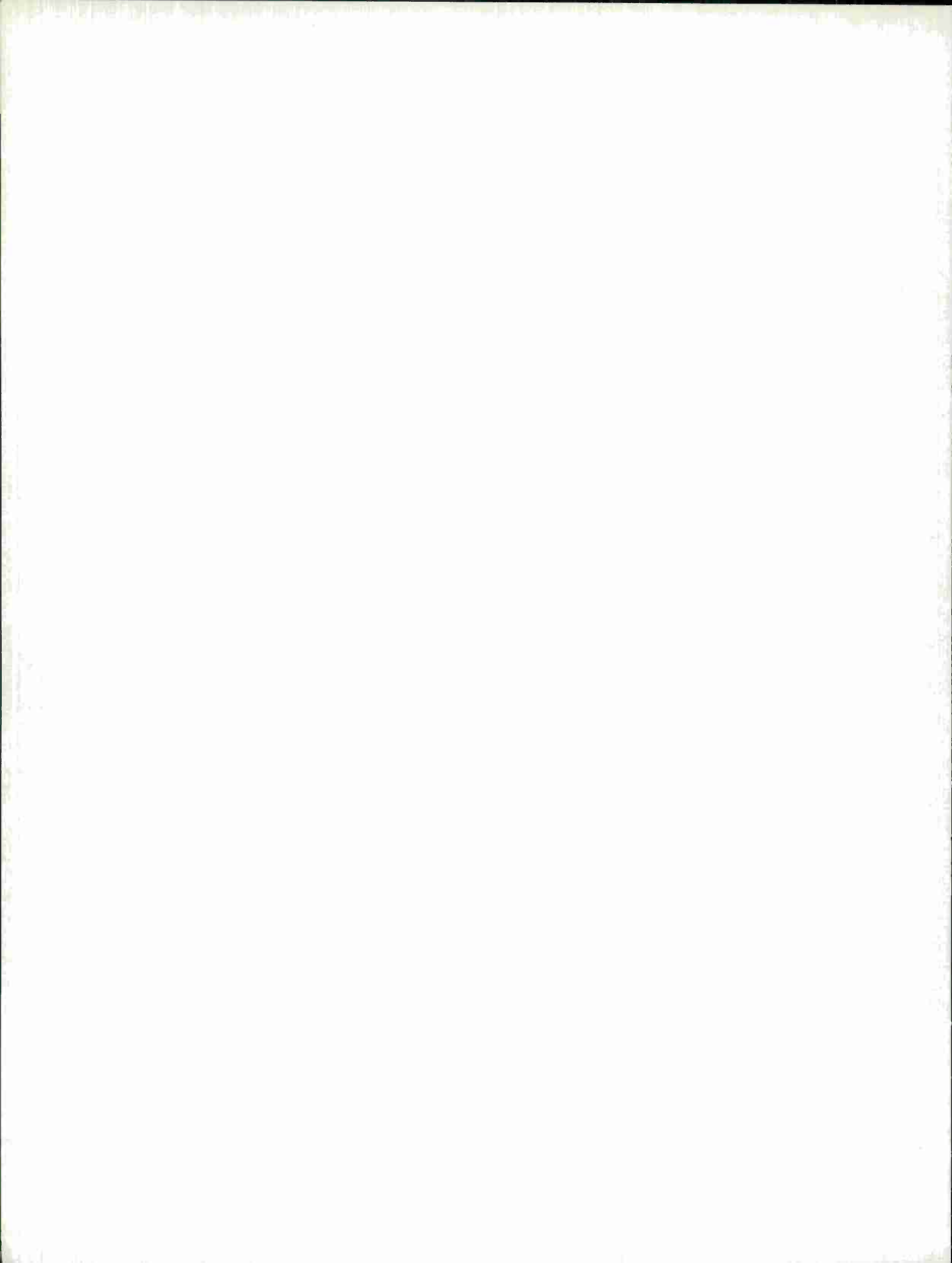
1 FEBRUARY - 30 APRIL 1977

ISSUED 25 JULY 1977

Approved for public release; distribution unlimited.

LEXINGTON

MASSACHUSETTS



ABSTRACT

This report covers in detail the solid state research work of the Solid State Division at Lincoln Laboratory for the period 1 February through 30 April 1977. The topics covered are Solid State Device Research, Quantum Electronics, Materials Research, Microelectronics, and Surface-Wave Technology. Funding is primarily provided by the Air Force, with additional support provided by the Army, ARPA, NSF, and ERDA.

CONTENTS

Abstract	iii
Introduction	v
Reports on Solid State Research	ix
Organization	xiv
 I. SOLID STATE DEVICE RESEARCH	 1
A. GaAs Directional-Coupler Switch With Stepped $\Delta\beta$ Reversal	1
B. Determination of the p-n Junction Location in Double-Heterostructure GaInAsP/InP Laser Diodes	4
C. Proton Bombardment in InP	6
D. Ion Implantation in InP	12
E. Si Contamination of LPE InP	13
 II. QUANTUM ELECTRONICS	 17
A. Flashlamp-Excited NdP ₅ O ₁₄ Laser	17
B. Efficient Second-Harmonic Generation in AgGaSe ₂	21
C. Detection of Doubled CO ₂ Radiation Scattered From a Remote Target	21
D. Grating-Tuning of the O ¹³ CS and C ₂ H ₂ Lasers	22
E. Second Vibrational Overtone Absorption Spectrum of the ν_3 Mode of SF ₆	23
F. Vibrational Energy Relaxation of CH ₃ F Dissolved in Liquid O ₂ and Ar	26
G. Vibrational Two-Photon Resonance Linewidths in Liquid Media	31
H. Blackbody Heterodyne NEP Measurements of Schottky-Diode Receivers	33
 III. MATERIALS RESEARCH	 37
A. Growth of Ni-Doped MgF ₂ Single Crystals	37
B. Compositions and Laser Wavelengths of Ga _x In _{1-x} As _y P _{1-y} Layers Lattice-Matched to InP Substrates	41
 IV. MICROELECTRONICS	 47
A. Charge-Coupled Devices (CCDs): Programmable Transversal Filter	47
B. Charged-Coupled Devices: Imagers	49
C. A Two-Level Interconnect System for Ceramic Hybrid Integrated-Circuits' Substrates Utilizing Aluminum-Silicon Dioxide-Aluminum	50
 V. SURFACE-WAVE TECHNOLOGY	 55
A. Polyimide-Membrane X-Ray-Lithography Mask	55
B. Integrating Correlator	55

INTRODUCTION

I. SOLID STATE DEVICE RESEARCH

A GaAs 2×2 electrooptic waveguide switch in which the power isolation in both switch states can be electrically optimized has been demonstrated. The device exhibits up to 25 dB power isolation in both states with total power output constant to within ≤ 0.3 dB.

The p-n junction location in double-heterostructure (DH) GaInAsP/InP laser diodes was determined by using a scanning electron microscope. Even though undoped or Sn-doped quaternary layers are n-type if grown on insulating substrates, the quaternary layer in the grown DH is p-type, presumably due to Zn diffusion from the Zn-doped InP capping layer.

An investigation of the proton bombardment of InP indicates that the resistivity of n-type InP can be increased only to a level of about $10^3 \Omega\text{-cm}$, while the resistivity of p-type InP can be increased to $>10^8 \Omega\text{-cm}$ for an optimum multiple-energy dose or an optimum combination of dose and post-bombardment anneal. The results can be explained by a model which assumes that the proton bombardment creates both deep donor and deep acceptor levels.

The ion implantation of Se, Si, Be, Mg, Cd, and Fe in InP was investigated. Implantation of Fe was found to be quite effective in creating high-resistivity layers in n-type InP. A multi-energy Fe implant in n-type InP ($n \approx 4 \times 10^{16} \text{ cm}^{-3}$) followed by annealing at 725°C for 15 min. yielded layers with a resistivity $\approx 10^7 \Omega\text{-cm}$.

A high distribution coefficient impurity, identified as silicon, was shown to be a key problem in achieving the goal of growing high-purity InP layers by liquid-phase epitaxy (LPE). We found that not only is the Si concentration of as-received In too high, but also the LPE growth solution can be contaminated with Si through direct or indirect contact with quartz if a strongly reducing gas such as dry H_2 is present in the growth tube.

II. QUANTUM ELECTRONICS

A simple miniature room-temperature pulsed $\text{NdP}_5\text{O}_{14}$ laser excited by a small Xe flashlamp has been made, with threshold energies of a few hundred millijoules. Output energies of 4.5 mJ have been obtained with less than 1 J input, and further improvement is expected.

Efficient second-harmonic generation has been achieved in AgGaSe_2 . Using a CO_2 laser with a 0.5-nsec pulse length, a second-harmonic energy conversion efficiency of 33 percent was observed.

The second harmonic generated by a CdGeAs_2 crystal pumped by a passively Q-switched CO_2 laser has been scattered from a remote topographic target and the return signals detected. This system can be used for differential absorption measurements of the concentrations of atmospheric constituents.

Grating tuning of the optically pumped O^{13}CS and C_2H_2 lasers has been demonstrated. From the measured 53 laser lines of the O^{13}CS laser, the band center for the laser transition has been determined.

The second vibrational overtone absorption spectrum of the ν_3 mode of SF_6 has been measured using a 1-m grating spectrometer. Only a single Q-branch transition was observed.

Infrared double-resonance and saturation techniques have both been used to measure the V-T relaxation of the ν_3 mode of CH_3F in dilute solution in the cryogenic hosts liquid O_2 and liquid Ar. With the double-resonance technique, a relaxation time of 375 ± 35 nsec was found in liquid O_2 , while in liquid Ar the relaxation time was 1.30 ± 0.15 μsec . An induced $\nu_3 \rightarrow 2\nu_3$ absorption was observed in the double-resonance measurement; the observed anharmonicity is in good agreement with the gas-phase literature value.

The previously developed rotation-vibration interaction model for the widths of two-photon resonances in liquid media has been used in an analysis of recently reported results for the temperature dependence of the Raman linewidth in liquid N_2 . The results indicate that this process contributes significantly to the observed linewidths.

Heterodyne radiometry with blackbody sources was used to determine the sensitivities of GaAs Schottky-diode submillimeter receivers. At 500 μm , an NEP of 2×10^{-18} W/Hz was measured for the system.

III. MATERIALS RESEARCH

A vertical gradient-freeze technique has been developed for growing single crystals of Ni-doped MgF_2 which will be used to determine whether this material can be used as a tunable source of near-infrared laser radiation. Crystals of excellent optical quality, as determined by interferometer evaluation, have been grown in self-sealing graphite crucibles in a tungsten-element resistance furnace.

To assist in the development of near-infrared lasers and detectors utilizing $\text{Ga}_x\text{In}_{1-x}\text{As}_y\text{P}_{1-y}$ layers lattice-matched to InP substrates, the alloy compositions of such layers have been determined by electron microprobe analysis, and the emission wavelengths of lattice-matched $\text{Ga}_x\text{In}_{1-x}\text{As}_y\text{P}_{1-y}/\text{InP}$ double-heterostructure diode lasers have been measured at 300 and 77 K. Over the entire lattice-matching range, the composition data are well represented by $x = 0.40y + 0.067y^2$, and the laser photon energies at 300 K are given by $h\nu$ (eV) = $1.307 - 0.60y + 0.03y^2$.

IV. MICROELECTRONICS

The optimum channel-stop implants and field oxide growth conditions have been determined for the MOS transistors which will be part of the static shift register being added to the programmable transversal filter to control the binary multiplication. An optimum value for channel doping was found to be $3.8 \times 10^{16} \text{ cm}^{-3}$, which could be achieved by implanting boron at 200 keV at a dose of $1 \times 10^{13} \text{ cm}^{-2}$. The 0.8- μm -thick field oxide was grown by a steam oxidation for 4 hr at 1000°C, followed by an 1100°C gate oxidation in dry O_2 plus 3% HCl for 18 min., followed by a 15-min. N_2 anneal. This process yielded an acceptably small flatband voltage of -4 V.

Several wafers of the 100- \times 400-cell CCD imaging devices for the GEODSS (Ground Electro-Optical Deep Space Surveillance) Program have been fabricated incorporating an integral light shield over the input and output shift registers. A total of 12 of 84 devices have passed a DC probe test and will be dynamically evaluated. Devices which pass the dynamic test will be used to assemble a 2-chip prototype hybrid imaging array.

A two-level interconnect system has been developed for fabricating hybrid integrated circuits on alumina substrates. Sputtered aluminum is used for both metallization levels, and insulation between levels is provided by either sputtered or low-temperature CVD SiO_2 . Substrates for two complex, multi-chip hybrid circuits have been fabricated by this process — one an 8-bit multiplier utilizing 8 microprocessor chips and the other a 16-chip CCD sensor array. Best results were obtained using a CVD oxide and a 99.5-percent alumina substrate polished to 1- to 2- μ -in. surface finish.

V. SURFACE-WAVE TECHNOLOGY

A process has been developed for fabricating polyimide-membrane x-ray-lithography masks with membrane thicknesses ranging from 0.5 to several micrometers. Thin membranes are required so that they are relatively transparent to soft x-rays. The process produces large-area rugged x-ray masks suitable for use at the 13.3- \AA Cu_L wavelength as well as at the 44.7- \AA C_K and 8.34- \AA Al_K wavelengths.

The first results have been obtained with a new acoustoelectric surface-acoustic-wave device, the integrating correlator. The basic operation of the device is similar to a correlation receiver. An array of Schottky diodes held in close proximity to a LiNbO_3 delay line provides mixing of two counter-propagating surface waves, and each diode integrates the mixer product over time. Integration times of 50 msec or more have been achieved. For a device with a bandwidth of 20 MHz, this provides a potential correlation gain in excess of 50 dB.

REPORTS ON SOLID STATE RESEARCH

15 February through 15 May 1977

PUBLISHED REPORTS

Journal Articles

JA No.

4621	Minority Carriers in Graphite and the H-Point Magnetoreflexion Spectra	W. W. Toy* M. S. Dresselhaus* G. Dresselhaus	Phys. Rev. B <u>15</u> , 4077 (1977)
4622	Infrared Third-Harmonic Generation in Phase Matched CO Gas	H. Kildal	IEEE J. Quantum Electron. <u>QE-13</u> , 109 (1977)
4629	Graphite Intercalation Compounds: Electronic Properties in the Dilute Limit	M. S. Dresselhaus* G. Dresselhaus J. E. Fischer*	Phys. Rev. B <u>15</u> , 3180 (1977)
4647	Multiple-Energy Proton Bombardment in n ⁺ -GaAs	J. P. Donnelly F. J. Leonberger	Solid-State Electron. <u>20</u> , 183 (1977)
4666	Temperature-Gradient LPE Growth of Pb _{1-x} Sn _x Te	S. H. Groves	J. Electron. Mater. <u>6</u> , 195 (1977)
4667	Frequency Dependence of the Dissociation of Polyatomic Molecules by Radiation	D. M. Larsen	Opt. Commun. <u>19</u> , 404 (1976)
4684	Microscopic Theory of the Lattice Dynamics of hcp Rare-Earth Metals	J. C. Upadhyaya* A. O. E. Animalu	Phys. Rev. B <u>15</u> , 1867 (1977)
4693	Resonant Infrared Third-Harmonic Generation in Cryogenic Liquids	H. Kildal S. R. J. Brueck	Phys. Rev. Lett. <u>38</u> , 347 (1977)
4700	Low-Dose n-Type Ion Implantation into Cr-Doped GaAs Substrates	J. P. Donnelly C. O. Bozler W. T. Lindley	Solid-State Electron. <u>20</u> , 273 (1977)
4703	1500-h Continuous cw Operation of Double-Heterostructure GaInAsP/InP Lasers	C. C. Shen J. J. Hsieh T. A. Lind	Appl. Phys. Lett. <u>30</u> , 353 (1977)
4705	Room-Temperature cw Operation of Buried-Stripe Double-Heterostructure GaInAsP/InP Diode Lasers	J. J. Hsieh C. C. Shen	Appl. Phys. Lett. <u>30</u> , 429 (1977)

* Author not at Lincoln Laboratory.

Meeting Speeches

MS No.

4177E	Wavelength-Selective Surfaces for Solar Energy Utilization	J. C. C. Fan	Proc. SPIE Vol. 85: <u>Optics in Solar Energy Utilization II</u> (Society of Photo-Optical Instrumentation Engineers, Bellingham, Washington, 1976), pp. 39-46
4238	Preparation of Polycrystalline Si Thin Films by Laser Crystallization	J. C. C. Fan H. J. Zeiger P. M. Zavracky	Proc. National Workshop on Low Cost Polycrystalline Solar Cells, Dallas, Texas, 18-19 May 1976, pp. 89-104
4262	The Physical Properties of Cadmium Telluride	A. J. Strauss	Rev. Phys. Appl. <u>12</u> , 167 (1977)
4280	CdTe Optical Waveguide Modulators	D. L. Spears A. J. Strauss	Rev. Phys. Appl. <u>12</u> , 401 (1977)

* * * * *

UNPUBLISHED REPORTS

Journal Articles

JA No.

4694	X-Ray Photoemission Spectroscopy Studies of Sn-Doped Indium-Oxide Films	J. C. C. Fan J. B. Goodenough	Accepted by J. Appl. Phys.
4709	Selective Black Absorbers Using RF-Sputtered $\text{Cr}_2\text{O}_3/\text{Cr}$ Cermet Films	J. C. C. Fan S. A. Spura	Accepted by Appl. Phys. Lett.
4718	$\text{Ag}_2\text{Se}-\text{Ga}_2\text{Se}_3$ Pseudobinary Phase Diagram	J. C. Mikkelsen, Jr.	Accepted by Mat. Res. Bull.
4721	CW Operation of Distributed Feedback $\text{Pb}_{1-x}\text{Sn}_x\text{Te}$ Lasers	J. N. Walpole A. R. Calawa S. R. Chinn S. H. Groves T. C. Harman	Accepted by Appl. Phys. Lett.
4724	Second Vibrational Overtone Absorption Spectrum of the ν_3 Mode of SF_6	H. Kildal	Accepted by J. Chem. Phys.
4726	Thin-Film VO_2 Submillimeter-Wave Modulators and Polarizers	J. C. C. Fan H. R. Fetterman F. J. Bachner P. M. Zavracky C. D. Parker	Accepted by Appl. Phys. Lett.

JA No.

4728	Flash-Lamp Excited NdP ₅ O ₁₄ Laser	S. R. Chinn W. K. Zwicker*	Accepted by Appl. Phys. Lett.
4734	Optoacoustic Measurements of Energy Absorption in CO ₂ TEA Laser Excited SF ₆ at 293 and 145 K	T. F. Deutsch	Accepted by Opt. Lett.
MS-4271	X-Ray Lithography	H. I. Smith D. C. Flanders	Accepted by Jap. J. Appl. Phys.

Meeting Speeches†

MS No.

4230E	GaInAsP/InP Double- Heterostructure Diode Lasers	J. J. Hsieh	Electrical Engineering and Computer Science Seminar, M.I.T., 16 February 1977
4361A,B	GaInAsP/InP Double- Heterostructure Diode Lasers for Optical Fiber Communications	J. J. Hsieh	Seminar, IBM Thomas Watson Research Center, Yorktown Heights, New York, 21 March 1977; Philips Re- search Laboratory, Briar- cliff Manor, New York, 22 March 1977
4362A	Surface State Studies on SrTiO ₃ Electrodes	J. G. Mavroides	Electrochemistry and Physics of Semiconductor-Liquid Solu- tion Interfaces Under Illumina- tion Meeting, Airlie, Virginia, 3 May 1977
4378	1000-Hour Continuous cw Operation of Double- Heterostructure GaInAsP/ InP Lasers	C. C. Shen J. J. Hsieh T. A. Lind	Optical Fiber Transmission Meeting, Williamsburg, Vir- ginia, 22-24 February 1977
4379	Room-Temperature cw Operation of Buried Stripe, Double-Heterostructure GaInAsP/InP Diode Lasers	J. J. Hsieh C. C. Shen	
4381A	Interaction of O ₂ and H ₂ O with Surface Defects on TiO ₂ and SrTiO ₃	H. J. Zeiger V. E. Henrich G. Dresselhaus	American Physical Society Meeting, San Diego, 21-24 March 1977
4398	Theory of Spin-Disorder- Raman Scattering in Magnetic Semiconductors	S. A. Safran* G. Dresselhaus B. Lax*	
4402	Surface States on SrTiO ₃	V. E. Henrich G. Dresselhaus H. J. Zeiger	

* Author not at Lincoln Laboratory.

† Titles of Meeting Speeches are listed for information only. No copies are available for distribution.

MS No.

4382	Selective Black Absorbers Using rf-Sputtered $\text{Cr}_2\text{O}_3/\text{Cr}$ Cermets Films	J. C. C. Fan S. A. Spura	} 151st Meeting of the Electro- chemical Society, Philadelphia, 8-13 May 1977
4383	Defect Surface States on SrTiO_3 Photoelectrolytic Electrodes	J. G. Mavroides V. E. Henrich H. J. Zeiger G. Dresselhaus J. A. Kafalas D. F. Kolesar	
4384	New Lithium Solid Electrolytes	H. Y-P. Hong	
4392	Tunable Infrared Lasers	A. Mooradian	3rd International Conference on Lasers and Their Applica- tions, Dresden, Germany, 27 March - 2 April 1977
4405A	Efficient Infrared Third- Harmonic Generation in Cryogenic Liquids	H. Kildal	Seminar, M.I.T., 16 March 1977
4407,A	Heterodyne Sensitivity Evaluation of GHz Bandwidth 10.6 μm Photodiodes	D. L. Spears	IRIS Detector Specialty Group Meeting, U.S. Air Force Academy, Colorado, 22-24 March 1977; Symposium on 10.6 Micron Laser and De- tector Technology for Com- pact Military Devices, Ft. Monmouth, New Jersey, 10 May 1977
4415	Ternary Semiconductor Crystals for Nonlinear Optical Applications	G. W. Iseler H. Kildal N. Menyuk	Third International Conference on Ternary Compounds, Edinburgh, Scotland, 14-15 April 1977
4416	Double Resonance Spectroscopy of SF_6	P. F. Moulton D. M. Larsen J. N. Walpole A. Mooradian	Laser Induced Chemistry Conference, Park City, Utah, 14-16 February 1977
4417	Resonant Infrared Third- Harmonic Generation in Cryogenic Liquids	S. R. J. Brueck H. Kildal	7th Winter Colloquium on High Power Visible Lasers, Park City, Utah, 16-18 February 1977
4428,A	GHz Bandwidth HgCdTe Photodiodes for Heterodyne Radiometry	D. L. Spears	Seminar, NASA Langley Re- search Center, Langley, Vir- ginia, 16 February 1977; Seminar, University of Mary- land, College Park, 17 Feb- ruary 1977
4442	Submicrometer Engineering	H. I. Smith	Electrical Engineering Collo- quium, Rensselaer Polytechnic Institute, Troy, New York, 10 March 1977

MS No.

4450	Spanning the Gap Between Microelectronic and Surface Wave Signal Processors with Acoustoelectrics	R. W. Ralston	IEEE Groups on Sonics and Ultrasonics and on Electron Devices, Technical Meeting of Boston Chapters, MITRE Corp., Bedford, Massachusetts, 13 April 1977
4463	GaAs Thin-Film Solar Cells	J. C. C. Fan	ERDA Solar Photovoltaic R&D Review Meeting, Washington, D.C., 22-23 March 1977
4474	New Na ⁺ and Li ⁺ Superionic Conductors	J. A. Kafalas	Fourth Biennial Air Force Electrochemistry Conference, Colorado Springs, 28-29 April 1977
4485	Advance Schottky Diode Concepts	H. R. Fetterman	SPIE/SPSE Technical Symposium, Reston, Virginia, 18-21 April 1977

ORGANIZATION

SOLID STATE DIVISION

A. L. McWhorter, *Head*
I. Melngailis, *Associate Head*
C. R. Grant, *Assistant*
P. E. Tannenwald

QUANTUM ELECTRONICS

A. Mooradian, *Leader*
P. L. Kelley, *Associate Leader*

Barch, W. E.	Hancock, R. C.
Brueck, S. R. J.	Kildal, H.
Burke, J. W.	Larsen, D. M.
Chinn, S. R.	Menyuk, N.
DeFeo, W. E.	Moulton, P. F.
Deutsch, T. F.	Osgood, R. M.
Fetterman, H. R.	Parker, C. D.
Fleming, M. W.*	Pine, A. S.

ELECTRONIC MATERIALS

A. J. Strauss, *Leader*
H. J. Zeiger, *Associate Leader*

Anderson, C. H., Jr.	Kafalas, J. A.
Button, M. J.	Kolesar, D. F.
Chapman, R. L.	Krohn, L., Jr.
Delaney, E. J.	LaFleur, W. J.
Dresselhaus, G.	Mastromattei, E. L.
Dwight, K., Jr.	Mavroides, J. G.
Fahey, R. E.	Mroczkowski, I. H.
Fan, J. C. C.	Owens, E. B.
Feldman, B.	Palm, B. J.
Finn, M. C.	Pantano, J. V.
Gay, R. R.*	Pierce, J. W.
Henrich, V. E.	Reed, T. G.
Hong, H. Y-P.	Tchernev, D. I.
Hsieh, J. J.	Tracy, D. M.
Iseler, G. W.	Vohl, P.

APPLIED PHYSICS

A. G. Foyt, *Leader*
T. G. Harman, *Assistant Leader*
C. E. Hurwitz, *Assistant Leader*

Armiento, C. A.*	Lind, T. A.
Belanger, L. J.	McBride, W. F.
Calawa, A. R.	Paladino, A. E.
Carter, F. B.	Plonko, M. C.
DeMeo, N. L., Jr.	Shen, C. C.
Donnelly, J. P.	Spears, D. L.
Ferrante, G. A.	Tsang, D. Z.*
Groves, S. H.	Walpole, J. N.
Leonberger, F. J.	

SURFACE WAVE TECHNOLOGY

E. Stern, *Leader*
R. C. Williamson, *Assistant Leader*

Baker, R. P.	Li, R. C. M.
Brogan, W. T.	Melngailis, J.
Cafarella, J. H.	Ralston, R. W.
DeGraff, P. D.	Reible, S. A.
Dolat, V. S.	Schulz, M. B.
Efremow, N., Jr.	Shaver, D.*
Flanders, D. C.	Smith, H. I.
Hurlbut, D. H.	Vlannes, N.*
Kernan, W. C.	

MICROELECTRONICS

W. T. Lindley, *Leader*
F. J. Bachner, *Assistant Leader*

Beatrice, P. A.	Gray, R. V.
Bozler, C. O.	Hansell, G. L.*
Burke, B. E.	Lincoln, G. A., Jr.
Chiang, A. M.	McGonagle, W. H.
Clifton, B. J.	Mountain, R. W.
Clough, T. F.	Murphy, R. A.
Cohen, R. A.	Pichler, H. H.
Daniels, P. J.	Silversmith, D. J.
Durant, G. L.	Smythe, D. L., Jr.
Foley, G. H.	Wilde, R. E.
Grant, L. L.	

* Research assistant

I. SOLID STATE DEVICE RESEARCH

A. GaAs DIRECTIONAL-COUPLER SWITCH WITH STEPPED $\Delta\beta$ REVERSAL

A necessary component for the development of many GaAs-based integrated optical circuits is an electrooptic 2×2 waveguide switch having high-power isolation (e.g., >20 dB) in each switch state. To achieve such power isolation, it is desirable to be able to electrically optimize performance so that light incident on one of the two guides can be confined to either guide at the device output by application of an appropriate bias. One method of realizing such a device is to fabricate a directional-coupler switch in which the sign of $\Delta\beta$, the propagation constant difference between the two coupled guides, is reversed midway along the sample length. This scheme was originally proposed¹ by Kogelnik and Schmidt and was subsequently demonstrated by them² in LiNbO_3 . In principle, this stepped $\Delta\beta$ -reversal switch is superior to the conventional directional-coupler switch,³ in which only one of the switch states can be electrically optimized. Here, we report the first successful demonstration of a GaAs directional-coupler switch with stepped $\Delta\beta$ reversal. The switch is characterized at $1.06 \mu\text{m}$ by up to 25 dB power isolation in both states, which to our knowledge is the largest isolation reported to date for a GaAs-based device. (Previously, 17-dB isolation in a conventional GaAs directional-coupler switch has been reported.^{4,5}) The total power output for this $\Delta\beta$ -reversal device was constant to within ≤ 0.3 dB between zero bias and the optimum bias for each switch state.

The switch we have fabricated is shown schematically in Fig. I-1(a). The structure consists of three closely spaced Pt-Au Schottky-barrier strip electrodes electroplated through openings in an SiO_2 film on a $2.7\text{-}\mu\text{m}$ -thick n^- ($6 \times 10^{14} \text{ cm}^{-3}$) layer which was grown by vapor-phase epitaxy on an n^+ ($1 \times 10^{18} \text{ cm}^{-3}$) substrate. A back contact was formed on the n^+ substrate by electroplating AuSn. For the devices reported here, the two outer Schottky-barrier electrodes were $75 \mu\text{m}$ wide and were separated from the central $4\text{-}\mu\text{m}$ -wide electrode by $8\text{-}\mu\text{m}$ spaces. Light is guided in the n^- layer and is laterally confined to the two channels between the electrodes. The structure thus forms a pair of closely spaced three-dimensional waveguides (referred to as metal-clad optical striplines^{6,7}) and can function as a directional coupler.⁸ To permit the modes of switch operation to be described here, each strip electrode had a $25\text{-}\mu\text{m}$ gap midway along its length [as shown in Fig. I-1(b)], so that the device actually had six equal-length electrodes. For each switch state, the two appropriate outer electrodes were biased and the other electrodes were left open-circuited. The waveguides were formed on (100) surfaces with propagation in the [011] direction to minimize power loss.^{4,5} The device length (11.9 mm) was about 50 percent greater than the coupling length.

In discussing the operation of the $\Delta\beta$ -reversal switch, it is convenient to identify¹ the switch states as the straight-through state and the crossover state, and to refer to the waveguide into which light is end-fire-coupled as the input guide and to the other waveguide as the coupled guide. Thus, for the straight-through state the light at the device output face is confined to the input guide, and for the crossover state the light at the device output face is confined to the coupled guide.

To obtain the straight-through state, the device is operated as a conventional directional-coupler switch. The two outer electrodes along one of the channels are reverse-biased, creating via the electrooptic effect a $\Delta\beta$ uniform along the length of the device. This destroys the

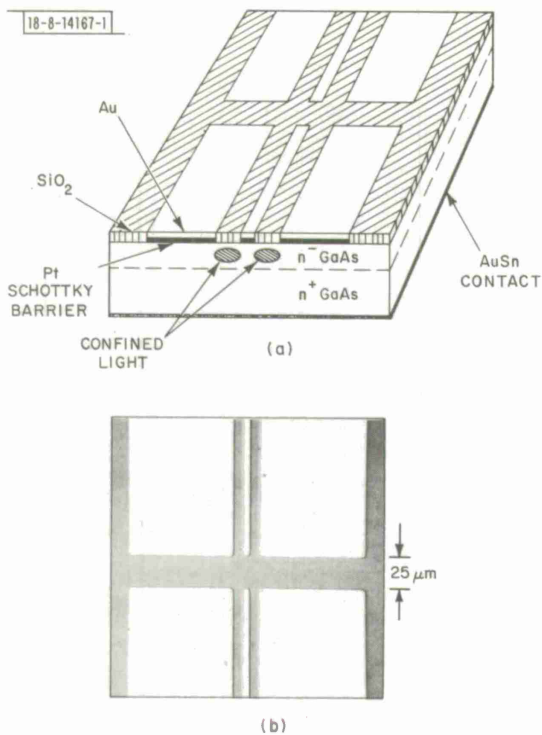
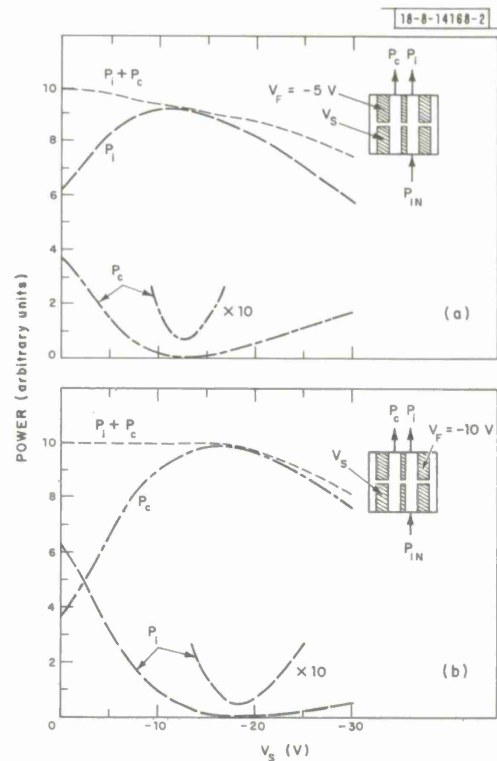


Fig.I-1. (a) Schematic diagram of GaAs directional-coupler $\Delta\beta$ -reversal switch fabricated from metal-clad optical striplines showing gap in strip Schottky-barrier electrodes and light propagating in two guiding channels in n^- layer. Light can be confined to either guide by reverse-biasing appropriate Schottky barriers. Drawing is not to scale. (b) Photomicrograph of portion of top surface of a switch showing two 8- μm -wide guides with 4- μm spacing and 25- μm gap that provides electrical isolation between sections of strip Schottky barriers.

Fig.I-2. Power vs bias for each guide of GaAs switch for (a) uniform- $\Delta\beta$ bias arrangement, and (b) reversed- $\Delta\beta$ bias arrangement. Measured total power for $V_S = 0$ is same for both cases. Diagrams in upper-right portion of each figure indicate bias configuration.



phase synchronism of the two guides, resulting in a decrease of both the coupling length and the fraction of power transferred. For the appropriate $\Delta\beta$, the light originally exiting from the coupled guide will be transferred to the input guide. To obtain the crossover state, two outer electrodes that are diagonally opposed are reverse-biased so that the sign of $\Delta\beta$ is reversed midway along the device length. For a broad range of sample lengths greater than a coupling length, the light at the device output face can be confined to the coupled guide. As explained in detail in Refs. 1 and 2, this effect can be thought of as resulting from two conventional directional-coupler switches in series. For equal-length electrodes and ideal structures, the required value of $\Delta\beta$ for each length is that which causes the light to be equally divided between the two guides midway along the sample (i.e., at the strip electrode gap); since the difference in propagation constant between the two guides is reversed at this point, the light at the output face must emerge from the coupled guide. In principle, both switch states can be achieved using the $\Delta\beta$ -reversal biasing scheme; however, the value of $\Delta\beta$ (and hence the applied bias) to confine the light to the input guide is considerably larger than necessary if a uniform- $\Delta\beta$ biasing scheme is used. The best performance for a $\Delta\beta$ -reversal switch, in practice, will generally be obtained by biasing each electrode individually to compensate for any inherent $\Delta\beta$ between the guides (e.g., due to asymmetries introduced in fabrication) and for any difference in electrode length.

The devices were evaluated at $1.06\text{ }\mu\text{m}$ using end-fire coupling and a phase-sensitive detection method previously described.^{4,5} Measurements were made using a Nd:YAG laser polarized to excite the lowest-order TE mode. Switching performance was determined, and losses due to attenuation along the guide length and to the strip electrode gap were evaluated.

Transmission measurements through single-mode $8\text{-}\mu\text{m}$ -wide guides with no electrode gap fabricated on the same chip with the switches indicated that the loss coefficient α was $\sim 1.6\text{ cm}^{-1}$ (6.9 dB/cm). Comparison of transmission through single guides and couplers with and without a gap fabricated on the same chip indicated that loss due to the gap was small ($\leq 0.2\text{ dB}$). A small loss is consistent with theoretical loss estimates based on the spreading of a waveguide mode (modeled as a Gaussian) over a region where the refractive index difference responsible for lateral confinement is removed.⁹ A small loss is also predicted from simple diffraction arguments, since the $8\text{-}\mu\text{m}$ guide width is equivalent to about 26 wavelengths at $1.06\text{ }\mu\text{m}$ in GaAs.

The switching performance of these devices is shown in Fig. I-2(a-b) which indicates the variation with bias of the output power P_i from the input guide, P_c from the coupled guide, and the total power $P_i + P_c$. The data were obtained by biasing the electrodes individually as shown in the upper-right portion of each plot. To obtain these plots, the voltage V_F on the biased electrode nearest the output was fixed at its predetermined optimum value (i.e., highest power isolation), and the voltage V_S on the biased electrode nearest the input was varied. Figure I-2(a) indicates that for the straight-through state, the optimum biases are $V_F = -5\text{ V}$ and $V_S = -12.5\text{ V}$. This results in 21-dB power isolation between the guides. The total output power decreases 0.3 dB between zero and optimum bias. For the crossover state, shown in Fig. I-2(b), 23-dB power isolation is obtained for $V_F = -10\text{ V}$ and $V_S = -18\text{ V}$. In this case, the total power output is constant to within 0.1 dB between zero and optimum bias. The optimum power isolations reported here could be obtained for a range of $\pm 1\text{ V}$ about the given V_F values by adjusting V_S by $\lesssim 1\text{ V}$ for each V_F . When equal voltages were applied to both electrodes, power isolation in both switch states was degraded from the optimum values. For the straight-through state, 19-dB isolation was obtained at -10 V ; and for the crossover state, 15-dB isolation was obtained at -25 V .

A similar degradation was reported for LiNbO_3 devices.² The need for separate biases for optimum isolation can probably be attributed to asymmetries in the device introduced in fabrication. In fact, initial experiments on switches carefully fabricated to minimize asymmetry show 23-dB isolation in both switch states for equal-voltage bias arrangements. Optimum performance of 25-dB isolation for these switches was obtained for voltage differences of < 4 V.

As is evident in Fig. 1-2, there is appreciable power loss for biases greater in magnitude than 20 V, with the effect somewhat more pronounced for the uniform- $\Delta\beta$ arrangement. Although the bias range greater than 20 V is not of interest here, similar power loss was reported for conventional GaAs directional-coupler switches fabricated from metal-clad guides.⁸ The problem can perhaps be avoided by fabricating $\Delta\beta$ -reversal switches using $p^+n^-n^+$ channel-stop strip guides, since conventional switches made with this type of guide exhibited power conservation to within 0.2 dB for voltages corresponding to comparable electric fields.^{4,5} [Also, the $p^+n^-n^+$ guides have exhibited lower attenuation^{10,11} ($\alpha \sim 1 \text{ cm}^{-1}$) than the metal-clad guides reported here.]

For a number of applications (e.g., large bandwidth), a $\Delta\beta$ -reversal switch of minimum length would be useful. This can be achieved by using a sample only slightly longer than a coupling length. In this case, the device would be in the crossover state at zero bias. The power isolation in this crossover state could be optimized by application of a few volts in the reversed- $\Delta\beta$ bias arrangement. Preliminary results demonstrating this concept were obtained with an 8.5-mm-long GaAs switch having 7- μm -wide guides and 5- μm spacing. This device was about 10-percent longer than the coupling length. The zero-bias value of 13-dB isolation in the coupled guide was improved to 19 dB by biases of $V_F = 0$ V and $V_S = -4$ V. Light confinement of 19 dB was also obtained in the straight-through state by a uniform- $\Delta\beta$ bias arrangement with $V_F = V_S = -30$ V.

The small value of the loss associated with the strip electrode gap suggests that it should be feasible to use similar gaps to electrically isolate waveguide devices on a common GaAs substrate. For example, a pair of passive waveguides could be fabricated with one section, separated by gaps, serving as a switch. Also, low-loss right-angle GaAs waveguide intersections could be fabricated. The 25- μm gaps used here are not a lower limit on gap size, and the loss associated with the gap theoretically would be expected to decrease as the gap became smaller. For the $\Delta\beta$ -reversal GaAs switches of the type reported here, edge-breakdown considerations suggest that the smallest gap between biased electrodes is on the order of twice the epitaxial-layer thickness.

F. J. Leonberger
C. O. Bozler

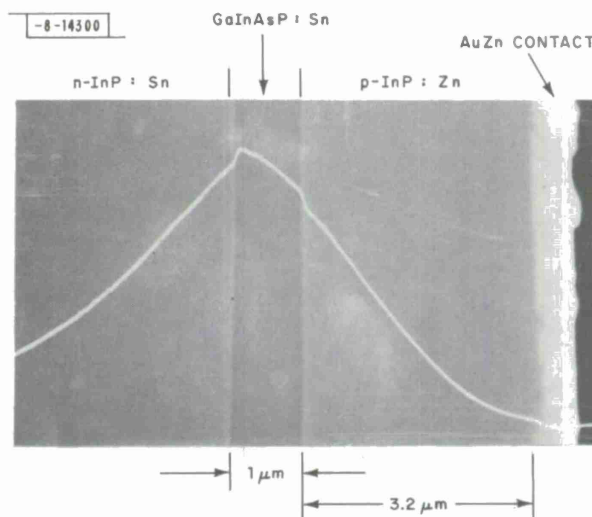
B. DETERMINATION OF THE p-n JUNCTION LOCATION IN DOUBLE-HETEROSTRUCTURE GaInAsP/InP LASER DIODES

Double-heterostructure (DH) GaInAsP/InP lasers were investigated by using a scanning electron microscope (SEM). The DH samples, which are similar to those reported previously,¹² were prepared by growing successive liquid-phase-epitaxial (LPE) layers of n-InP, n-GaInAsP, and p-InP on (111)B-oriented melt-grown n-InP substrates. The two barrier layers, namely n-InP and p-InP, were doped with Sn and Zn, respectively, to a carrier concentration $\sim 3 \times 10^{18} \text{ cm}^{-3}$. The GaInAsP active layer was either undoped or Sn-doped, and its carrier concentration varied from 10^{16} to 10^{17} cm^{-3} . The GaInAsP layers were determined to be n-type from Hall measurements, which were made on GaInAsP layers grown on semi-insulating InP

substrates under the same growth conditions. Both InP layers are 2 to 3 μm thick, while the thickness of the GaInAsP layer varied from 0.1 to 1 μm . The growth temperature and the growth time for the p-InP layer are typically 620°C and 10 min., respectively.

The samples were made into broad-area devices, following the fabrication procedures described earlier.¹² Devices with ideal I-V characteristics and mirror-like cleaved facets were selected for further investigations.

Fig. I-3. SEM photomicrograph of cleaved and etched cross section of a DH GaInAsP/InP laser. An induced current trace was superimposed on secondary emission image ($\times 13,000$).



The heterojunction interfaces were delineated by etching the cleaved cross section in a solution of $3\text{H}_2\text{SO}_4:1\text{H}_2\text{O}_2:1\text{H}_2\text{O}$ at room temperature for 20 sec. An SEM photomicrograph of the cleaved section of a typical broad-area device is shown in Fig. I-3. The two heterojunction interfaces between the InP and the GaInAsP layers are revealed in the secondary emission image, and the location of the p-n junction is identified by the peak of the superimposed current trace. For all the devices tested in this work, the p-n junction was found to coincide with the n-InP/GaInAsP interface to within 0.1 μm , which indicates that the GaInAsP layer has been converted to p-type during the growth of the p-InP layer. This phenomenon is caused by the diffusion of Zn from the p-InP layer through the GaInAsP and further into the n-InP region. It is noted that the n-InP layer remained n-type, due to the fact that since the n-InP layer is more heavily doped, the amount of Zn which diffused into this layer was not able to compensate sufficiently to convert the n-InP layer to p-type. As a result, the p-n junction was pinned at the n-InP/GaInAsP interface. For the sample shown in Fig. I-3, the effective Zn diffusion coefficient in the GaInAsP region is estimated to be $1.4 \times 10^{-11} \text{ cm}^2 \text{ sec}^{-1}$ at 620°C. This value is the same order of magnitude as that reported for InP (Ref. 13) at a diffusion temperature of 650°C using a chemical diffusion method.

These results thus suggest that the fast diffusion rate of Zn in GaInAsP causes a shift of the p-n junction during the growth process. In order to prevent the p-n junction from occurring in the n-InP, a heavily doped n-InP layer (i.e., $3 \times 10^{18} \text{ cm}^{-3}$) is required.

C. C. Shen
J. J. Hsieh

C. PROTON BOMBARDMENT IN InP

It has previously been shown that proton bombardment can be used to make high-resistivity layers in both p- and n-type GaAs (Refs. 14 to 19), $\text{Al}_x\text{Ga}_{1-x}\text{As}$ (Refs. 19 and 20), and GaP (Ref. 21), and that this technique is useful in device processing.¹⁵ It has been used in the fabrication of avalanche photodiodes,^{22,23} IMPATT diodes,²⁴⁻²⁶ planar transferred electron logic devices,²⁷ planar Schottky-barrier detector diodes,²⁸ "stripe-geometry" lasers,²⁹ field-effect transistors,³⁰ and optical waveguides.³¹⁻³³ Recently, proton bombardment in InP was used in the fabrication of stripe-geometry InP/InGaAsP lasers.¹² Although the resistivity of the bombarded region was apparently increased sufficiently to confine the diode current to the stripe, no actual measurements of the electrical properties of the bombarded p-InP were made. In this section we will present results of a study on the effects of proton bombardment on the electrical properties of n- and p-type InP. Unlike results in the Ga-based III-V compounds, we found that the resistivity of n-type InP can be increased only to $\approx 10^3 \Omega\text{-cm}$; that of p-type InP, however, can be increased to $> 10^8 \Omega\text{-cm}$ for an optimum proton dose. A simple model is presented which explains all the results obtained to date.

The InP samples used in these experiments were cut from bulk (111)-oriented n-type, p-type, and high-resistivity Fe-doped ($\rho \approx 10^7 \Omega\text{-cm}$) crystals. The carrier concentration of the n-type samples ranged from 1×10^{16} to $1 \times 10^{18} \text{ cm}^{-3}$, and that of the p-type samples from 5×10^{17} to $5 \times 10^{18} \text{ cm}^{-3}$. After polishing, the B face of each sample was etched in a 1-part acetic acid: 1-part perchloric acid: 5-parts nitric acid: 1-part hydrochloric acid solution.³⁴ For initial experiments, thin gold contacts ($< 1000 \text{ \AA}$) were electroplated on the InP prior to bombardment. For subsequent experiments in which the bombarded samples were annealed, a 1000- \AA layer of SiO_2 was first pyrolytically deposited at 320°C . After the bombardment and anneal, holes were opened in the SiO_2 and gold contacts were electroplated or evaporated. The gold contacts in all cases were 20 mils in diameter. For the purposes of these experiments, the effects of the SiO_2 and the thin gold contacts on the range of protons could generally be neglected. A large-area, plated-gold back contact was usually used to contact the substrate. To evaluate the effects of the bombardments, the equivalent parallel resistance and capacitance of these Au-InP structures were measured.³⁵ In addition, Hall measurements of the van der Pauw type³⁶ were made on several samples.

Both single-energy 400-keV and multi-energy proton bombardments were carried out with the InP samples at room temperature. As in earlier results on $n^+\text{-GaAs}$ (Ref. 35), a multiple-energy proton bombardment was generally found to be superior to a single-energy bombardment. The multi-energy bombardment schedule used was based on a dose of N at 400 keV, 0.6 N at 300 keV, 0.3 N at 200 keV, and 0.2 N at 100 keV (where N is given in units of cm^{-2}). (There is some indication that an additional dose of 0.1 N at 50 keV may provide an even more "uniform-damage" region.) Neglecting the energy loss in the gold contact or SiO_2 , the depth to which this bombardment schedule affects the resistivity of the InP was found to be approximately $3.8 \mu\text{m}$. This was determined from the capacitance (5.8 pF for a 20-mil-diameter Au contact) measured on p-type InP bombarded with an optimum dose (see below).

For bombarded n-type InP, the current-voltage characteristics of the Au-InP devices were generally linear. The contact-to-substrate resistance increased with proton dose up to a maximum of 600 to 800 Ω , irrespective of the initial carrier concentration of the samples. This resistance is much greater than the initial resistance of the Au-InP, especially for samples with initial concentrations $\geq 1 \times 10^{17} \text{ cm}^{-3}$. Using a depth of $3.8 \mu\text{m}$ and the area of the gold

contacts, the maximum resistance corresponds to an average resistivity in the bombarded region of $\approx (3 \text{ to } 4) \times 10^3 \Omega\text{-cm}$. The minimum dose required to achieve this resistivity increases slightly with increasing initial carrier concentration. A multi-energy bombardment with $N = 1 \times 10^{15} \text{ cm}^{-2}$ (see above schedule) is generally sufficient for $n \approx 1 \times 10^{18} \text{ cm}^{-3}$ material. At higher doses, the resistivity decreases slightly with increasing dose.

On unbombarded or lightly bombarded p-type InP, the electrical characteristics of the Au-InP devices are those of a Schottky barrier on p-type material. With increasing dose, the current-voltage characteristics become more symmetrical and the capacitance decreases to a minimum of $\approx 5.8 \text{ pF}$. For an optimum dose, the current is linear with voltage out to $\geq \pm 25 \text{ V}$. The observed resistance corresponds to a resistivity $> 10^8 \Omega\text{-cm}$. For p-type samples with an initial concentration of $5 \times 10^{18} \text{ cm}^{-3}$, the optimum multiple-energy dose corresponds to an N of approximately $1 \times 10^{14} \text{ cm}^{-2}$. The optimum dose for $p = 5 \times 10^{17} \text{ cm}^{-3}$ material is about 0.3 of that required for $p \approx 5 \times 10^{18} \text{ cm}^{-3}$ material. For doses higher than the optimum, the resistivity of the bombarded layer decreases and the I-V characteristics of the Au-InP devices begin to look like diodes. For high doses ($N \approx 3 \times 10^{15} \text{ cm}^{-2}$), the diffusion voltage extrapolated from the forward I-V characteristics of these diodes is 0.8 to 0.9 V, and the forward series resistance is approximately 900Ω .

All these results can be explained using the simple model shown in Fig. I-4(a-c). In this model it is assumed that the proton bombardment creates deep donors and deep acceptors which, when they become sufficiently greater than the initial number of net shallow donors or acceptors, pin the Fermi level at about 0.30 to 0.34 eV above the intrinsic Fermi level E_i (or 0.26 to 0.30 eV below the conduction-band edge). There could be only one deep-donor level and one deep-acceptor

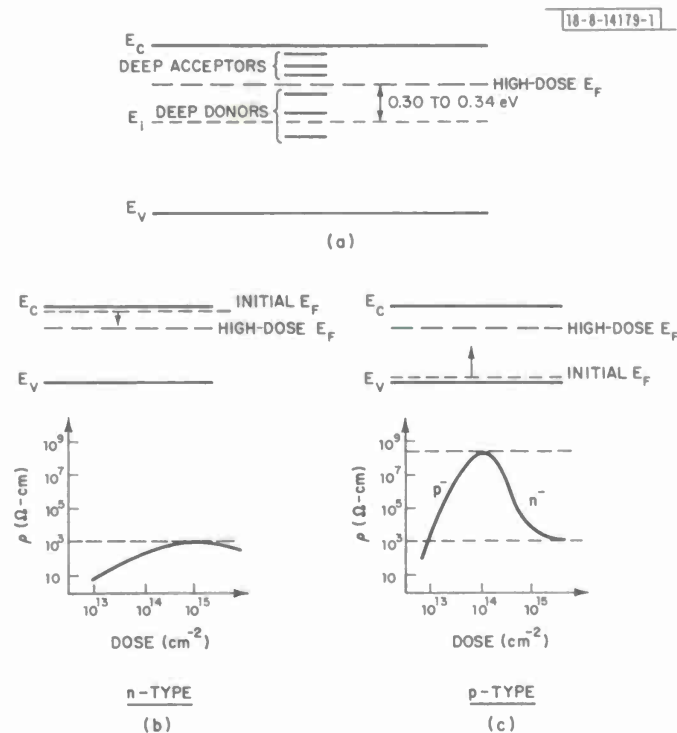


Fig. I-4. Simple theory of proton bombardment in InP: (a) position of Fermi level for high doses; (b) effects on n-type material; and (c) effects on p-type material.

TABLE I-1
MULTIPLE-ENERGY PROTON BOMBARDMENT IN $p \approx 5 \times 10^{18} \text{ cm}^{-3} \text{ InP}$

Sample	Proton Bombardment		No Anneal		200°C Anneal		300°C Anneal		400°C Anneal	
	Energy (keV)	Dose (cm^{-2})	R_o ($M\Omega$)	C^* (pF)	R_o ($M\Omega$)	C^* (pF)	R_o ($M\Omega$)	C^* (pF)	R_o ($M\Omega$)	C^* (pF)
1	400	1.0×10^{14}	≥ 50	6.5	≥ 100	6.0	Schottky barrier	83.2	—	—
	300	6.0×10^{13}								
	200	3.0×10^{13}								
	100	2.0×10^{13}								
2	400	3.0×10^{14}	n^- -p Junction	11.1	$\approx 5 M\Omega$	5.8	≥ 25	6.0	Schottky barrier	28.0
	300	1.8×10^{14}								
	200	9.0×10^{13}								
	100	6.0×10^{13}								
3	400	3.0×10^{15}	n^- -p Junction	76.5	n^- -p Junction	40.7	n^- -p Junction	29.2	≥ 30	6.0
	300	1.8×10^{15}								
	200	9.0×10^{14}								
	100	6.0×10^{14}								

*Capacitance measured at 500 kHz.

For 20-mil-diameter contact on ideal $3.8\text{-}\mu\text{m}$ -thick $10^8 \Omega\text{-cm}$ layer, $R_o = 18 M\Omega$ and $C = 5.8 \text{ pF}$.

level or a whole series of donor and acceptor levels as shown in Fig. I-4(a). It is not material to this simple model if the donors or acceptors are closer to the conduction-band edge. If they are associated with the same defects or complexes, however, the acceptor levels for any particular center would be closer to the conduction-band edge. In n-type material, as shown in Fig. I-4(b), the Fermi level moves downward with increasing proton dose until it becomes pinned at a position designated as the high-dose Fermi level. At this point, the resistivity is nominally $10^3 \Omega\text{-cm}$. At very high doses, banding of the defect levels will probably reduce the resistivity. In p-type material, as shown in Fig. I-4(c), the Fermi level moves upward with increasing proton dose. At a dose when the Fermi level is near the intrinsic Fermi level (probably just below, depending on the ratio of hole to electron mobility), the resistivity achieves a maximum. For higher doses, the Fermi level continues to move toward the conduction-band edge and the bombarded layer becomes weakly n-type. Based on this model, the Au-InP devices on p-type material will look like Schottky barriers for low doses, metal semi-insulating semiconductor structures near the optimum dose, and, for higher doses, $n^+ - p$ junctions with a high forward resistance due to the n^+ layers.

As a check on the model, Hall measurements of the van der Pauw type³⁶ were made on heavily bombarded layers in p-type and Fe-doped ($\rho \approx 10^7 \Omega\text{-cm}$) material. Several of the Fe-doped samples had a thin Mg ion-implanted p-type layer (see Sec. D below) with a sheet concentration of $4 \times 10^{13} \text{ cm}^{-2}$ and a mobility of $80 \text{ cm}^2/\text{V-sec}$. After a standard multi-energy bombardment with $N = 1 \times 10^{15}$ or $3 \times 10^{15} \text{ cm}^{-2}$, n-type conductivity was observed on all samples. Using a depth of $3.8 \mu\text{m}$ for the bombarded region, these measurements, however, generally give resistivities in the range of 200 to $1000 \Omega\text{-cm}$ with $n \approx (0.4 \text{ to } 1) \times 10^{14} \text{ cm}^{-3}$ and $\mu \approx 100 \text{ to } 500 \text{ cm}^2/\text{V-sec}$. These resistivity values are considerably lower than those obtained from I-V measurements on the Au-InP devices. The resistivities determined from the I-V measurements could be too high due to unaccounted-for contact resistance. On the other hand, the resistivity determined from the van der Pauw measurements could be too low due to current leakage through the substrates. At the present time, the resistivities obtained by the two methods can be considered an upper and lower limit, respectively. Therefore, a fairly wide range for the position of the high-dose Fermi level has been given, and the high-dose resistivity has been nominally shown as about $10^3 \Omega\text{-cm}$ in Fig. I-4.

Since many of the devices in which proton bombardment may be used could be subjected to elevated temperatures through post-bombardment fabrication procedures and/or operating conditions, the annealing characteristics of the proton-bombarded layers in p-type InP were investigated. The annealing behavior was found to be qualitatively similar to that reported for proton-bombarded GaP (Ref. 24) and $n^+ - \text{GaAs}$ (Ref. 35). For p-type InP bombarded with the optimum dose for maximum resistivity without an anneal, the resistivity decreases with increasing anneal temperature. For higher doses, the resistivity is initially lower but increases with anneal temperature until it reaches a maximum in the $10^8 \Omega\text{-cm}$ range. The optimum anneal temperature increases with dose. Table I-1 summarizes the pertinent results obtained on p-type material with an initial carrier concentration of $5 \times 10^{18} \text{ cm}^{-3}$. This table lists the DC resistance R_0 (measured on a curve tracer) and the capacitance C (measured at 500 kHz) of three samples bombarded with different doses, portions of which were annealed for 15 min. at several different temperatures up to 400°C . For an ideal $3.8\text{-}\mu\text{m}$ -thick layer of $10^8 \Omega\text{-cm}$ material, the resistance and capacitance of a 20-mil-diameter gold contact would be $18.7 \text{ M}\Omega$ and about 5.8 pF , respectively. For reference, the current-voltage characteristics of devices

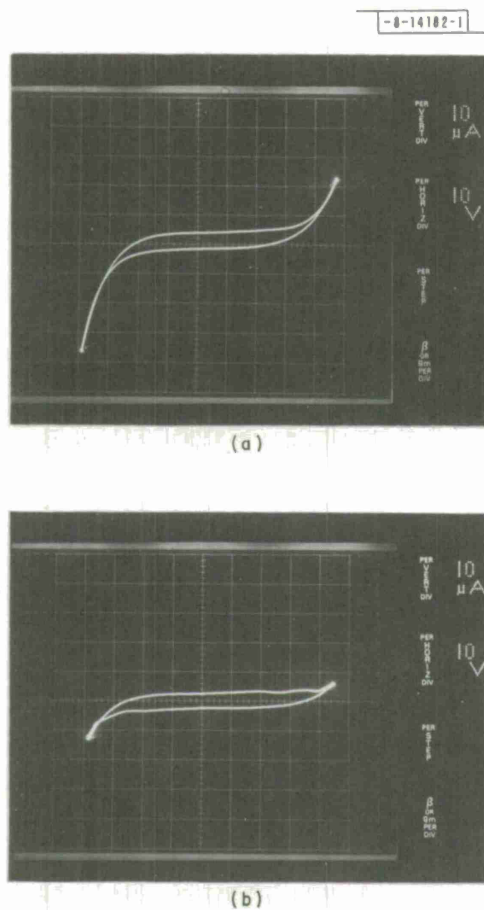


Fig.I-5. Current-voltage characteristics of 20-mil-diameter gold contacts on multi-energy proton-bombarded p^+ -InP ($p \approx 5 \times 10^{18} \text{ cm}^{-3}$) with (a) no annealing and (b) a 200°C, 15-min. anneal. InP was bombarded with proton doses of $1 \times 10^{14} \text{ cm}^{-2}$ at 400 keV, $6 \times 10^{13} \text{ cm}^{-2}$ at 300 keV, $3 \times 10^{13} \text{ cm}^{-2}$ at 200 keV, and $2 \times 10^{13} \text{ cm}^{-2}$ at 100 keV.

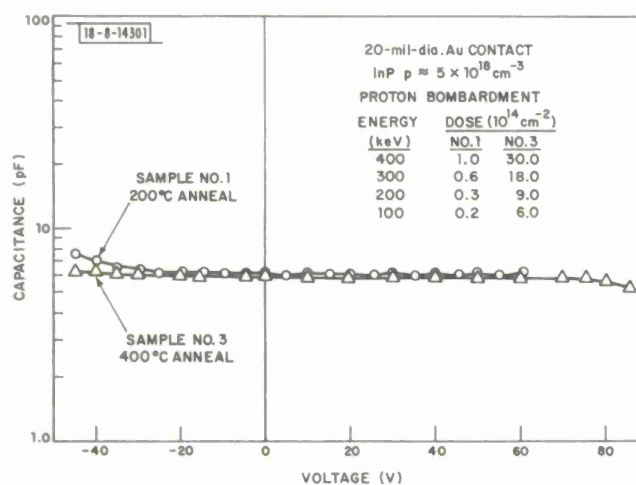


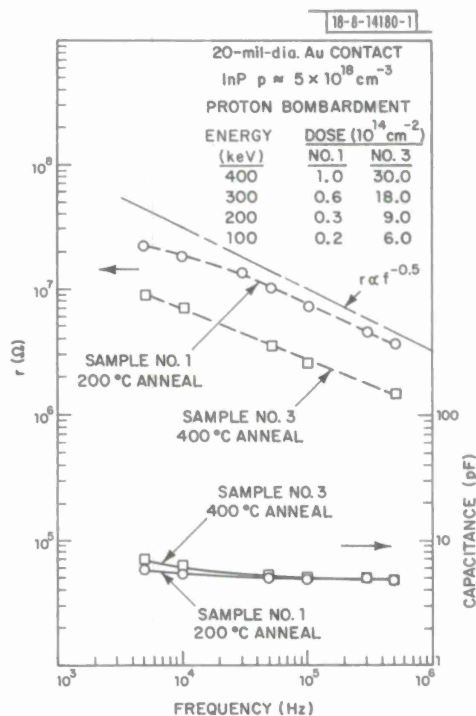
Fig.I-6. Capacitance vs voltage of 20-mil-diameter gold contacts on two multiple-energy proton-bombarded $p \approx 5 \times 10^{18} \text{ cm}^{-3}$ InP samples from Table I-1, with sample 1 annealed at 200°C and sample 3 annealed at 400°C. Capacitance was measured at 500 kHz.

on sample 1 with no anneal and with a 200°C anneal are shown in Fig. I-5(a-b). The resistance of the piece annealed at 200°C corresponds to a resistivity of $5 \times 10^8 \Omega\text{-cm}$. Very little leakage current flows out to ± 40 V, where the average electric field is $\approx 10^5$ V/cm.

Several points can be noted relative to the data of Table I-1. For sample 1, the resistance after a 200°C anneal was somewhat higher than that before annealing, while after a 300°C anneal the electrical characteristics appear to be that of a Schottky barrier on p⁻ material. For sample 2 with its higher proton dose, the resistivity probably reaches a maximum for an anneal between 200° and 300°C, and again Schottky-barrier characteristics are observed for a 400°C anneal. In sample 3 with the highest proton dose, the resistivity increases with anneal temperature, reaching a value in excess of $10^8 \Omega\text{-cm}$ at 400°C. In both samples 2 and 3, anneals at temperatures well below the optimum resulted in n⁻-p junctions with high forward resistances. This pattern of annealing characteristics can be qualitatively explained by postulating that more than one type of compensating defect or complex is being created by the proton bombardment, and that each type anneals out at a somewhat different temperature.

The capacitance (measured at 500 kHz) vs voltage of devices from sample 1 annealed at 200°C and from sample 3 annealed at 400°C are shown in Fig. I-6. There is little variation in capacitance out to high voltages (≥ 45 V) in either bias direction. The zero-bias capacitance and AC resistance as measured on a bridge, however, were found to vary with frequency. This is shown in Fig. I-7 for devices on the same two samples. The AC resistance r appears to be inversely proportional to $f^{-1/2}$ at higher frequencies, while the capacitance C decreases with frequency, asymptotically approaching a constant value at the higher frequencies. This type of behavior is similar to that observed in proton-bombarded n⁺-GaAs (Ref. 35) and is believed to be due to a hopping conductivity.^{37,38}

Fig. I-7. AC resistance and capacitance of 20-mil-diameter gold contacts on two multi-energy proton-bombarded $p = 5 \times 10^{18} \text{ cm}^{-3}$ InP samples from Table I-1, with sample 1 annealed at 200°C and sample 3 annealed at 400°C.



These results indicate that proton bombardment can increase the resistivity of n-type InP only to a level of about $10^3 \Omega\text{-cm}$, while the resistivity of p-type InP can be increased to $>10^8 \Omega\text{-cm}$ for an optimum multiple-energy dose or an optimum combination of dose and post-bombardment anneal. For properly chosen proton doses, high-resistivity layers can be achieved even with post-bombardment temperatures reaching at least as high as 400°C .

J. P. Donnelly
C. E. Hurwitz

D. ION IMPLANTATION IN InP

Ion implantation in InP has the potential of being of significant practical importance in the fabrication of optoelectronic and microwave devices. In this section, some initial results on the use of implantation to create n-type, p-type, and high-resistivity layers in InP will be summarized. Details of the encapsulation system and implantation results will be given in subsequent reports.

In general, post-implantation anneal temperatures of 725° to 750°C were required to achieve high electrical activity of the implanted ion species. To protect the InP from decomposition and anomalous carrier-concentration changes at these temperatures, a pyrolytic phosphosilicate glass (PSG) encapsulation, which permitted reproducible annealing at temperatures in excess of 750°C , was developed.

For n-type layers, 400-keV Se^+ or Si^+ ions were implanted into high-resistivity ($\rho \geq 10^7 \Omega\text{-cm}$) Fe-doped InP substrates held at both room temperature and 200°C . For doses of $10^{13} \text{ Se}^+/\text{cm}^2$, the sheet carrier concentration of the implanted layers did not depend on the substrate temperature, whereas the sheet mobility was consistently ≈ 20 percent higher on the samples implanted at 200°C . For doses $\geq 10^{14} \text{ Se}^+/\text{cm}^2$, higher values of both sheet carrier concentration N_s and mobility μ_s were obtained for implants made into the heated substrates. Following a 750°C , 15-min. anneal, samples implanted at 200°C with $1 \times 10^{14} \text{ Se}^+/\text{cm}^2$ exhibited an N_s of $7.8 \times 10^{13} \text{ cm}^{-2}$ and a μ_s of $1810 \text{ cm}^2/\text{V-sec}$. At a dose of $1 \times 10^{15} \text{ Se}^+/\text{cm}^2$, N_s and μ_s were $3 \times 10^{14} \text{ cm}^{-2}$ and $1300 \text{ cm}^2/\text{V-sec}$, respectively, which corresponds to a sheet resistivity of $16 \Omega/\square$. The results obtained with Si^+ were similar to those using Se^+ ions.

To make p-type layers in Fe-doped InP, Be^+ , Mg^+ , and Cd^+ were implanted at 50, 150, and 400 keV, respectively. Mg^+ was also implanted into n-type InP ($n \approx 4 \times 10^{16} \text{ cm}^{-3}$) with results similar to those obtained in the high-resistivity substrates. Implantation of Mg^+ into substrates at room temperature resulted in higher sheet carrier concentrations than implantation into heated substrates. Samples implanted at room temperature with $1 \times 10^{14} \text{ Mg}^+/\text{cm}^2$ and annealed at 750°C for 15 min. yielded values of N_s and μ_s of $5.2 \times 10^{13} \text{ cm}^{-2}$ and $83 \text{ cm}^2/\text{V-sec}$, respectively. For the heavier ion (Cd^+), however, the opposite result was found, and higher sheet carrier concentrations were obtained on samples implanted at 200°C . For a sample implanted at 200°C with $1 \times 10^{14} \text{ Cd}^+/\text{cm}^2$ and annealed at 750°C , N_s and μ_s were $3.6 \times 10^{13} \text{ cm}^{-2}$ and $90 \text{ cm}^2/\text{V-sec}$, respectively.

Although it was found that proton bombardment could convert p-type InP to high-resistivity material ($\rho \geq 10^8 \Omega\text{-cm}$), this technique was not similarly useful for substantially increasing the resistivity of n-type material (see Sec. C above). Implantation of Fe, however, was found to be quite effective in creating high-resistivity layers in n-type InP. A multi-energy (flat profile) Fe implant in n-type InP ($n \approx 4 \times 10^{16} \text{ cm}^{-3}$) followed by a 725°C 15-min. anneal resulted in layers with a resistivity $\approx 10^7 \Omega\text{-cm}$.

J. P. Donnelly
C. E. Hurwitz

E. Si CONTAMINATION OF LPE InP

Our early attempts to grow high-purity InP by liquid-phase epitaxy (LPE) from an In-rich solution have shown that silicon contamination is a key problem. Not only is the Si concentration in as-received In too high for our requirements, but the growth solution can be further contaminated through direct or indirect contact with quartz if a strongly reducing gas such as dry H_2 is present in the growth tube. Reports in the literature on LPE growth of high-purity InP have been incomplete in that the partial pressure of H_2O in the atmosphere of H_2 over the growth has either not been measured or has not been reported, and it is this parameter that determines the equilibrium concentration of Si in the growth solution at a given temperature. A similar situation exists for the Si contamination of Ga-rich growth solutions for GaAs growth.^{39,40} However, the distribution coefficient k_{Si} , which is the ratio of the Si concentration in the growth to that in the solution, is much less than 1 for GaAs but is ≈ 30 for InP (Ref. 41). With this large k_{Si} , the minimum donor concentration that can be expected, using our best as-received In with a few ppm Si, is $\sim 1 \times 10^{18} \text{ cm}^{-3}$.

The mechanism for Si contamination from the vapor is a two-step process. First, during baking or growth, gaseous SiO is formed by the reaction



where s , l , and g specify the solid, liquid, or gaseous phase of the substrate. In the second step, the SiO is reduced by contact with the molten In, and the Si dissolves in the solution



Weiner has worked out the kinetics of the Si contamination of a Ga solution as a function of temperature and partial pressure of H_2O (Ref. 40). By using thermodynamic values in the literature for the free energy of In_2O and the solubility of Si in In, it is possible to make similar calculations for the Si contamination of In solutions. An interesting second case considered by Weiner is that of direct Ga contact with a silica boat, whereby contamination can occur by the reaction (written here in terms of In instead of Ga)



This reaction is of interest even without the silica boat because, if driven to the left by a sufficiently high In_2O pressure (controlled by the H_2O pressure), purification of the In is achieved. The SiO_2 formed presumably floats to the surface where it either does not interfere with the growth or can be etched away. Again, it is possible to calculate the kinetics and the equilibrium values for the purification process, except that the limiting rate is expected to be set by the diffusion of Si to the In surface, rather than by the flow of gaseous reactants to the In surface, as treated by Weiner. In Fig. I-8, we show results of the equilibrium concentration calculations. By assuming $k_{Si} = 30$, we have expressed the Si concentration as a minimum donor concentration in the epitaxial InP, rather than as a fraction of the growth solution. The calculations have been made using free energy values from the JANAF Tables,⁴² as well as the thermodynamic data from Refs. 43 and 44.

In our experimental work, we have assembled an LPE growth system with high vacuum integrity and have reduced H_2O vapor levels in it by vacuum-baking. A procedure followed in several early runs was to give the In an extended (> 12 hr) bake at $\sim 930^\circ C$ under Pd-diffused H_2 . Epitaxial layers grown after this treatment have very high donor concentrations up to the

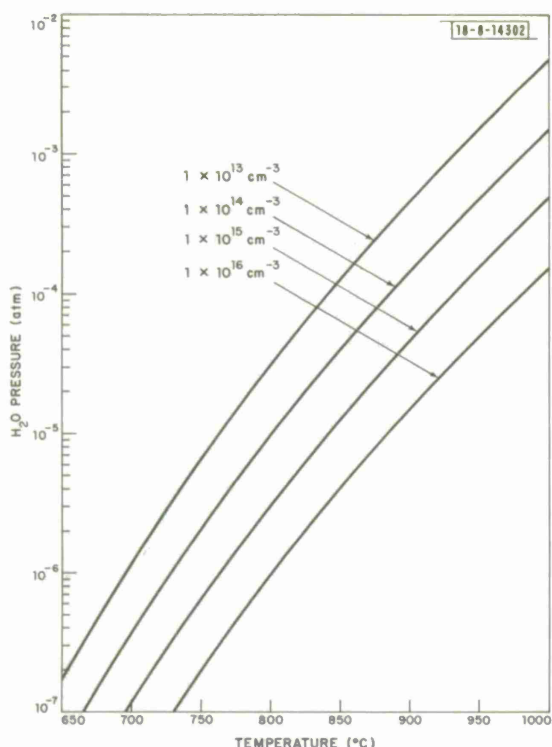


Fig. I-8. Results of calculation of Si concentration in In solution, in equilibrium with SiO_2 , as a function of temperature and H_2O vapor pressure. Lines of constant Si concentration are labeled by donor carrier concentration in InP grown from In-rich solution, assuming $k_{\text{Si}} = 30$.

mid- 10^{19} cm^{-3} range. Mass spectrographic analyses of the In showed that this baking treatment increased the Si content of the In from ~ 10 to above 100 ppm. The rate of Si contamination observed is predicted by the thermodynamic calculations if the partial pressure of H_2O in our system is 10^{-8} atm , a number that is corroborated by the temperature at which the In_2O_3 on the In charge is reduced, as observed with a "transparent" furnace.

Our next efforts at In baking went to the opposite extreme by utilizing a source of H_2O -saturated H_2 mixed with the Pd-diffused H_2 , giving a H_2O partial pressure of 10^{-2} atm . The Si level in the In baked in this atmosphere was not accurately determined, but it stayed under the 10-ppm level, and there were indications in the mass spectrographic analysis that the Si was concentrated at the surface, as expected if converted to SiO_2 . Net carrier-concentration levels in epitaxial layers grown from this In were reduced, but only to the $1 \times 10^{17} \text{ cm}^{-3}$ level. A bake under dry H_2 for 6 hr at 600°C reduced the net carrier concentration to the mid- 10^{16} level. Our interpretation of the results with the wet H_2 baking is that the Si contamination problem has been replaced by an O_2 contamination problem. Solomon observed that, for growth of GaAs from Ga-rich solution, H_2O or Ga_2O_3 added to the growth atmosphere or solution introduced donor impurities.⁴⁵ Our results are understandable if O_2 behaves in a similar way for InP grown from In-rich solution.

An apparatus for In baking is presently being assembled that will allow the ratio of H_2O to H_2 pressures to be set at any level between the very wet and very dry extremes used heretofore. With this, we will be able to compare measured donor concentrations with those predicted in Fig. I-8, and we expect that this apparatus will lead to considerably higher levels of purity than we have been able to obtain to date.

S. H. Groves
M. C. Plonko

REFERENCES

1. H. Kogelnik and R. V. Schmidt, IEEE J. Quantum Electron. QE-12, 396 (1976).
2. R. V. Schmidt and H. Kogelnik, Appl. Phys. Lett. 28, 503 (1976).
3. See, for example, H. F. Taylor, J. Appl. Phys. 44, 3257 (1973).
4. F. J. Leonberger, J. P. Donnelly, and C. O. Bozler, Appl. Phys. Lett. 29, 652 (1976), DDC AD-A037627.
5. Solid State Research Report, Lincoln Laboratory, M.I.T. (1976:3), p. 1, DDC AD-A034647/8.
6. J. Hamasaki and K. Nosu, IEEE J. Quantum Electron. QE-10, 822 (1974).
7. Y. Yamamoto, T. Kamiya, and H. Yanai, Appl. Opt. 14, 322 (1975).
8. J. C. Campbell, F. A. Blum, D. W. Shaw, and K. C. Lawley, Appl. Phys. Lett. 27, 202 (1975).
9. H. F. Taylor, Technical Report NELC TR 1913 (April 1974).
10. F. J. Leonberger, J. P. Donnelly, and C. O. Bozler, Appl. Phys. Lett. 28, 616 (1976), DDC AD-A027103/1.
11. Solid State Research Report, Lincoln Laboratory, M.I.T. (1976:1), p. 5, DDC AD-A027261/7.
12. J. J. Hsieh, J. A. Rossi, and J. P. Donnelly, Appl. Phys. Lett. 28, 709 (1976), DDC AD-A028550/2.
13. B. Tuck and A. Hooper, J. Phys. D: Appl. Phys. 8, 1806 (1975).
14. K. Wollleben and W. Beck, Z. Naturf. 21A, 1057 (1966).
15. A. G. Foyt, W. T. Lindley, C. M. Wolfe, and J. P. Donnelly, Solid-State Electron. 12, 209 (1969), DDC AD-694145.
16. J. C. Dymont, J. C. North, and L. A. D'Asaro, J. Appl. Phys. 44, 207 (1973).
17. B. R. Pruniaux, J. C. North, and G. L. Miller, in Proceedings of the 2nd International Conference on Ion Implantation in Semiconductors, 1971 (Springer-Verlag, Berlin, 1971), p. 212.
18. H. Haradu and M. Fujimoto, in Proceedings of the 4th International Conference on Ion Implantation in Semiconductors, 1974 (Plenum Press, New York, 1975), p. 73.
19. J. C. Dymont, L. A. D'Asaro, J. C. North, B. I. Miller, and J. E. Ripper, Proc. IEEE 60, 726 (1972).
20. P. N. Favenec and D. Diquet, Appl. Phys. Lett. 23, 546 (1973).
21. S. M. Spitzer and J. C. North, J. Appl. Phys. 44, 214 (1973).
22. W. T. Lindley, R. J. Phelan, Jr., C. M. Wolfe, and A. G. Foyt, Appl. Phys. Lett. 14, 197 (1969), DDC AD-694323.
23. G. E. Stillman, C. M. Wolfe, J. A. Rossi, and J. P. Donnelly, Appl. Phys. Lett. 25, 671 (1974), DDC AD-A006705/8.
24. R. A. Murphy, W. T. Lindley, D. F. Peterson, A. G. Foyt, C. M. Wolfe, C. E. Hurwitz, and J. P. Donnelly, in Proceedings of the 1972 Symposium on GaAs (Institute of Physics, London, 1973), p. 224, DDC AD-771891/9.
25. R. A. Murphy, W. T. Lindley, D. F. Peterson, and P. W. Staecker, in 1974-IEEE S-MTT International Microwave Symposium Digest of Technical Papers (IEEE, New York, 1974), p. 345.
26. I. S. Groves, J. D. Speight, P. Leight, N. McIntyre, S. O'Hara, and P. Hemment, in Proceedings of the 4th European Microwave Conference (Microwave Exhibitions and Publishers, Ltd., Kent, England, 1974), p. 163.

27. J. D. Speight, P. Leight, N. McIntyre, I. S. Groves, S. O. O'Hara, and P. Hemment, *Electron. Lett.* 10, 98 (1974).
28. L. C. Upadhyayula, S. Y. Narayan, and E. C. Douglas, *Electron. Lett.* 11, 201 (1975).
29. R. A. Murphy, C. O. Bozler, C. D. Parker, H. R. Fetterman, P. E. Tannenwald, B. J. Clifton, J. P. Donnelly, and W. T. Lindley, *IEEE Trans. Microwave Tech.* MTT-25, 494 (1977) [also in Solid State Research Report, Lincoln Laboratory, M.I.T. (1977:1), pp. 32-35].
30. B. R. Pruniaux, J. C. North, and A. V. Payer, *IEEE Trans. Electron Devices* ED-19, 672 (1972).
31. E. Garmire, H. Stoll, A. Yariv, and R. G. Hunsperger, *Appl. Phys. Lett.* 21, 87 (1972).
32. S. Somekh, E. Garmire, A. Yariv, H. L. Garvin, and R. G. Hunsperger, *Appl. Phys. Lett.* 22, 46 (1973).
33. P. N. Favenec and E. V. K. Rao, in Proceedings of the 4th International Conference on Ion Implantation in Semiconductors, 1974 (Plenum Press, New York, 1975), p. 65.
34. R. Becker, *Solid-State Electron.* 16, 1241 (1973).
35. J. P. Donnelly and F. J. Leonberger, *Solid-State Electron.* 20, 183 (1977).
36. L. J. van der Pauw, *Philips Res. Rep.* 13, 1 (1958).
37. M. Pollak and T. H. Geballe, *Phys. Rev.* 122, 1742 (1961).
38. A. K. Jonscher, *Non-Crystalline Solids* 8-10, 293 (1972).
39. H. G. B. Hicks and P. D. Greene, in Proceedings of the 3rd International Symposium on Gallium Arsenide (Inst. Phys. Phys. Soc., London, Conf. Ser. No. 9, 1971), p. 92.
40. M. E. Weiner, *J. Electrochem. Soc.* 119, 496 (1972).
41. G. G. Baumann, K. W. Benz, and M. H. Pilkuhn, *J. Electrochem. Soc.* 123, 1232 (1976).
42. JANAF Thermochemical Tables (U.S. Department of Commerce, Washington, D.C., 1965).
43. P. H. Keck and J. Broder, *Phys. Rev.* 90, 521 (1953).
44. A. Klinedinst and D. A. Stevenson, *J. Chem. Thermodyn.* 5, 21 (1973).
45. R. Solomon, in Proceedings of the 2nd International Symposium on Gallium Arsenide (Inst. Phys. Phys. Soc., London, Conf. Ser. No. 7, 1969), p. 11.

II. QUANTUM ELECTRONICS

A. FLASHLAMP-EXCITED $\text{NdP}_5\text{O}_{14}$ LASER

Laser materials such as $\text{NdP}_5\text{O}_{14}$ (NPP) have relatively little nonradiative quenching of the fluorescence at high Nd concentrations, and allow the possibility of very efficient pump absorption in small volumes. We have succeeded in obtaining operation of a high-Nd-concentration NPP laser excited by a conventional broad-band incoherent source, a miniature Xe flashlamp. Previous laser experiments with similar materials have used either Ar (Ref. 1), Kr (Ref. 2), or dye lasers,³ or semiconductor injection devices (laser diodes⁴ or light-emitting diodes⁵) as excitation sources. Particularly in the latter case, the small amount of power available from the pump has meant that small laser mode volumes were required to achieve threshold, and cooling was sometimes required to obtain lasing. With the relatively large crystals of $\text{Nd}_x\text{La}_{1-x}\text{P}_5\text{O}_{14}$ which have been grown, a laser has been constructed with greatly increased mode size approaching that of the lamp discharge. Because of the large pump absorption across the small transverse laser rod dimension, such lasers can be made smaller, and potentially more efficient, than similarly excited miniature Nd:YAG lasers.⁶

Single crystals of $\text{Nd}_x\text{La}_{1-x}\text{P}_5\text{O}_{14}$ were grown by a previously described technique⁷⁻¹² from hot phosphoric acids in which the rare-earth oxides had been dissolved. Growth was performed under isothermal conditions in a vitreous carbon crucible inside a semi-sealed furnace chamber at temperatures between 500° and 675°C. We were able to grow optically clear crystals up to 30 mm in cross section with fluorescent lifetimes equal or better than those reported in the literature,⁹ after optimizing the heatup procedure, growth temperature, and growth rate. Details on the crystal-growth technique will be reported elsewhere.¹³

Laser rods fabricated from these crystals were 7 mm in length with polished end "c" faces which were 1.2 mm² in cross section. Because of crystal cleavage problems, only the "a" and "b" side faces of the laser rods were ground. Flatness of the end faces is $\lambda/10$ at 5876 Å with a parallelism of better than 20 arcsec. The first available rods to be processed in this manner which were used in the present experiments were undiluted $\text{NdP}_5\text{O}_{14}$. Several ferroelastic domains,¹⁴ with walls normal to the c-axis, could be observed through crossed polarizers. The fluorescent lifetime of the $\text{Nd}^{3+4}\text{F}_{3/2}$ manifold was 135 μsec, measured using 0.2-μsec-long pulsed excitation at a wavelength of 0.8 μm.

The uncoated laser rod was mounted in the center of a 10.8-cm-long, nearly confocal optical cavity with 10-cm-radius mirrors, giving a calculated mode radius of 129 μm in the crystal and 188 μm at the mirrors. One mirror had high reflectivity at the laser wavelength of 1.05 μm, and three different output mirrors were used having transmissions of 0.15, 0.8, and 2.5 percent.

The laser rod was cemented to an aluminum tab with acetate cement (for ease in later demounting), and the tab and rod were inserted in a side slot of a 13-mm-long cylindrical reflector. This reflector was simply a small aluminum block with a slotted hole drilled through it, into which was inserted a 6.5-mm-inner-diameter slotted thin-wall quartz tube, which had a reflective layer of aluminum evaporated on its inner surface. A linear Xe-filled flashlamp was inserted in the reflector assembly parallel to the laser rod and about 1 mm from it. This lamp had a quartz envelope with 1-mm-dia. bore and 10-mm-long discharge length. The separated components of the laser head are shown in Fig. II-1. The lamp was driven in a simple, single-mesh discharge circuit¹⁵ with a total of 10-μF capacitance and about 75-μH series inductance

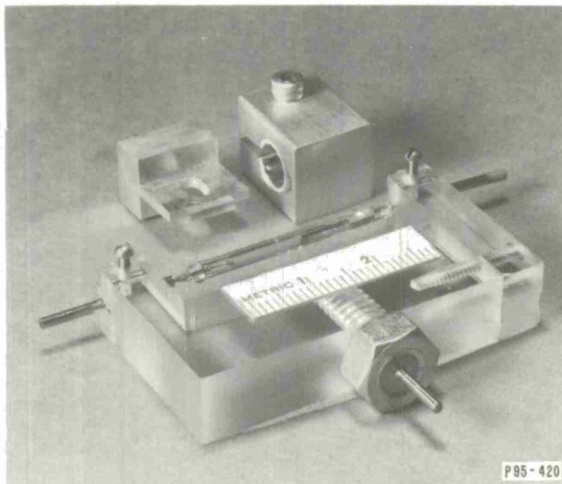


Fig. II-1. Disassembled components of $\text{NdP}_5\text{O}_{14}$ laser head showing cylindrical pump collector assembly (top right), mounted laser rod (left), and flashlamp and holder (bottom).

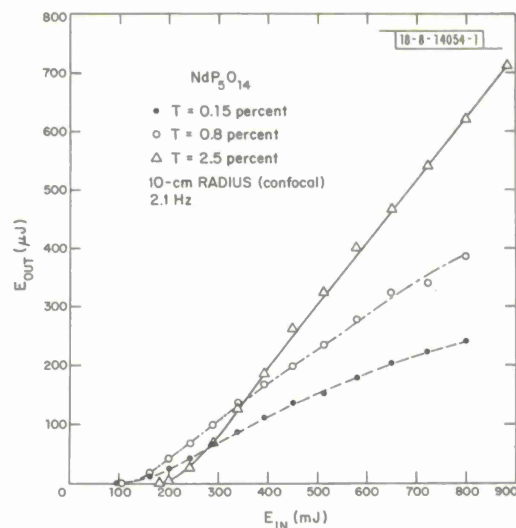


Fig. II-2. Laser output energy of $\text{NdP}_5\text{O}_{14}$ laser as a function of stored electrical energy input to flashlamp, with output mirror transmissions of 0.15, 0.8, and 2.5 percent. Repetition rate is 2.1 Hz, and output is predominantly TEM_{00} .

TABLE II-1 NPP LASER THRESHOLDS FOR DYE LASER AND LAMP EXCITATION				
Output Mirror Transmission (percent)	Quasi-CW Threshold Power		Pulsed Threshold Energy	
	(mW)	(normalized)	(mJ)	(normalized)
0.15	112	0.8	95	0.9
0.8	140	1.0	105	1.0
2.5	241	1.7	181	1.7

(including that of the series trigger transformer). This lamp should have a lifetime exceeding 10^6 shots at 1-J energy input with our present pulse duration, 100 μ sec. With this laser configuration it was also possible to use collinear excitation by a chopped CW dye-laser beam tuned to the 0.58- μ m Nd^{3+} absorption band. This system is described more fully in Ref. 3 (Chinn *et al.*), and was used in the NPP laser alignment and to measure CW thresholds.

The output from the NPP laser was measured by a calibrated Si photodiode, whose current was integrated by a capacitor in measuring output energies. At higher output levels, this detection system was compared with a presumably better calibrated thermopile detector, and all photodiode data were corrected to correspond to the thermopile output.

Two rods of the type described above were tested and lased with very similar performance. The data reported here are for the better of the two. The results with a 2.1-Hz repetition rate for output pulse energy vs electrical energy stored in the capacitors are shown in Fig. II-2 for the three output mirror transmissions indicated. The output calibration is accurate to about ± 5 percent, and for each data point individual output pulses fluctuated approximately ± 10 percent about the average. The quasi-CW thresholds for dye-laser excitation and pulsed energy thresholds for flashlamp excitation are summarized in Table II-1. The thresholds normalized by the 0.8-percent values are in fairly good agreement for the pulsed and CW excitations. Using the ratios of the slope efficiencies from the 2.5- and 0.8-percent mirror data, we estimate an upper bound on the loss to be $L = 1.5$ percent. This value is only in qualitative agreement with that estimated using the 0.15-percent mirror slope efficiency or from comparing the measured and calculated CW thresholds using the cross-section data of Ref. 16. However, the theoretical threshold calculation is not extremely precise, and there may also have been experimental uncertainty in obtaining the same degree of laser alignment and internal loss with the interchange of output mirrors. Because of the poor thermal mounting, rod heating was significantly reduced with a 1.0-Hz pulse rate, and using the 2.5-percent mirror, 1.5-mJ output was obtained at 0.97-J input. Observation of the far-field transverse mode distribution of the laser output with an infrared-sensitive television system showed that even without any mode-controlling apertures the mode was rather symmetric and predominantly TEM_{00} .

When a more closely coupled pump collector was used, with a 5-mm inner diameter, and the output energy was optimized with a multimode transverse distribution, significantly more energy was obtained, as shown in Fig. II-3. The output time behavior is shown in Fig. II-4, with the spiking and fluctuation commonly found in solid-state lasers with long fluorescence lifetimes. A spectrum of the laser output showed emission over a 7- \AA bandwidth, with partially separated modes 0.49 \AA apart, characteristic of the rod etalon longitudinal mode separation.

In the present rod geometry, the ferroelastic c-plane domain walls, associated with the two monoclinic orientations of the a-axis differing by $\pm 0.5^\circ$, do not affect the laser performance. The laser radiation is polarized along the b-axis by the intrinsic gain anisotropy,¹⁷ and neither the polarization nor propagation direction in the b-plane is changed by the a-axis shifts. Using a polarizing prism, we verified that the output was completely polarized along the b-axis ($> 1500:1$). In other experiments, we have not observed any visible scattering of dye-laser pump radiation by domain walls, implying that the NPP laser radiation is also unaffected.

It is clear that major improvements on performance can be obtained by straightforward means. First, the coupling of the excitation into the laser mode could probably be improved by using a more efficient pump collector and improving the laser side surfaces and mounting.

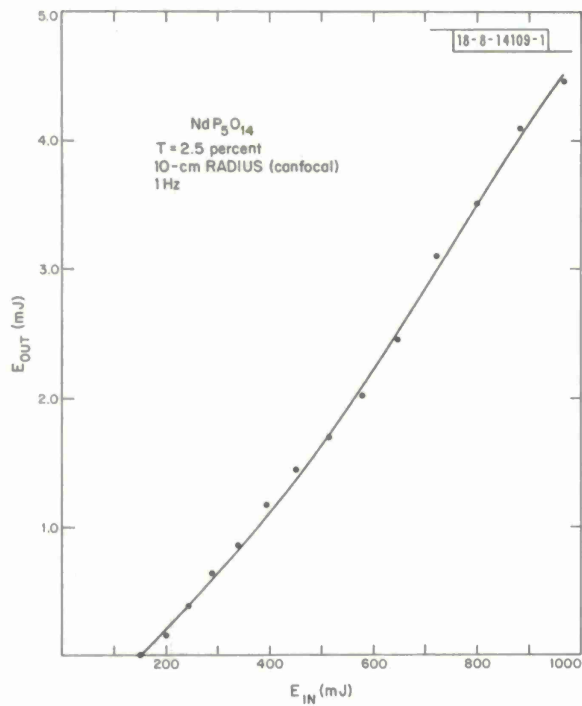
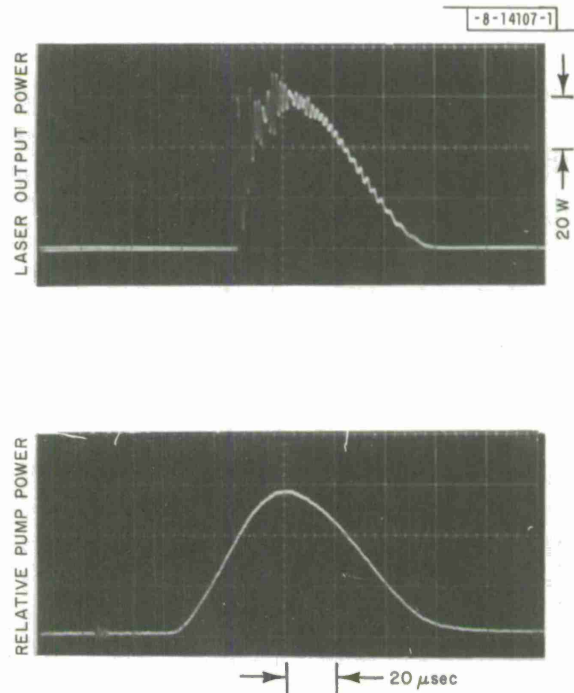


Fig. II-3. Laser output energy of $\text{NdP}_5\text{O}_{14}$ laser as a function of stored energy input to flashlamp, with 2.5-percent mirror transmission and multi-transverse-mode output. A more closely coupled pump collector is used, and repetition rate is 1 Hz.

Fig. II-4. Time dependence of $\text{NdP}_5\text{O}_{14}$ laser output and flashlamp radiation at energy output of 4.45 mJ and energy input of 0.97 J.



Second, rough calculations show that with impulse excitation an optimum compound of composition $\text{Nd}_{0.3}\text{La}_{0.7}\text{P}_5\text{O}_{14}$ should have 30-percent lower threshold than $\text{NdP}_5\text{O}_{14}$. Since our pump pulse is relatively long, this factor should increase somewhat more because the lower concentration material will have a longer fluorescent lifetime with less inversion loss before lasing begins. Finally, larger output-mirror transmission should give greater output energies, although with the present uncertainty in the internal loss, the optimum coupling and output energy cannot be accurately estimated now.

S. R. Chinn
W. K. Zwickert†

B. EFFICIENT SECOND-HARMONIC GENERATION IN AgGaSe_2

The chalcopyrites CdGeAs_2 and AgGaSe_2 are efficient nonlinear materials for frequency-doubling of CO_2 laser radiation. The maximum external energy conversion efficiencies we have obtained using a conventional CO_2 TEA laser with a 70-nsec pulse length are 27 percent for an antireflection-coated CdGeAs_2 crystal 12 mm long, and 7 percent for an uncoated AgGaSe_2 crystal 16 mm long.¹⁸ In the latter experiment, the internal conversion efficiency corresponded to 11 percent. CdGeAs_2 has a nonlinear figure of merit 30 times that of AgGaSe_2 . At high conversion efficiencies, however, the difference in energy conversion is smaller because nonlinear saturation effects limit the conversion in CdGeAs_2 . In contrast, no such effects have been observed in AgGaSe_2 , and here the laser-induced breakdown threshold limits the conversion efficiency. For pulse lengths around 70 nsec, the breakdown threshold is determined by the energy density. Therefore, the second-harmonic conversion efficiency in AgGaSe_2 should improve for shorter laser pulses, which allows higher power densities before breakdown.

In an experiment with the 16-mm AgGaSe_2 crystal and a CO_2 laser source consisting of an oscillator-amplifier system¹⁹ that uses optical free induction decay²⁰ to generate 0.5-nsec TEM_{00} mode laser pulses, we have obtained an external energy conversion efficiency of 21 percent, corresponding to an internal conversion efficiency of 33 percent. This is presently the highest conversion efficiency that has been observed for frequency-doubling of CO_2 laser radiation.

H. Kildal
E. Yablonovitch‡
G. W. Iseler

C. DETECTION OF DOUBLED CO_2 RADIATION SCATTERED FROM A REMOTE TARGET

Doubled CO_2 laser lines have coincidences with absorption lines of CO and NO, and they also lie within the absorption region of other molecular species of interest. Therefore, the ability to achieve significant power and energy levels at doubled CO_2 frequencies makes the use of such frequencies attractive as a line-tunable laser source in a monostatic differential absorption system for remote monitoring of molecular constituents in the atmosphere. We have established that CdGeAs_2 crystals grown at Lincoln Laboratory are capable of frequency-doubling the output of a CO_2 laser with power-conversion efficiencies in excess of 20 percent at high-power levels without damaging the crystal.²¹⁻²³ Average-power levels of 2 W and energy pulses of 200 mJ at the doubled frequency have been obtained in separate experiments.

† Philips Laboratories, Briarcliff Manor, NY.

‡ Harvard University, Cambridge, MA.

Furthermore, the CdGeAs_2 crystals will be equally effective in a sum- or difference-frequency mixing mode, which increases the available frequency coverage and the number of constituents which can be detected.

An initial experiment was carried out in which the frequency-doubled output of a CO_2 laser emanating from a CdGeAs_2 crystal was collimated using a telescope and aimed at the side of a building located approximately 23 m from the telescope. The building served as a topographic reflector, the return from which was focused on an InSb detector. The topographically reflected signal, along with the original doubled output, is shown in Fig. II-5. The original beam trace, which served to trigger the oscilloscope, was obtained by using a beam splitter to send a fraction of the doubled output to an Au:Ge detector.

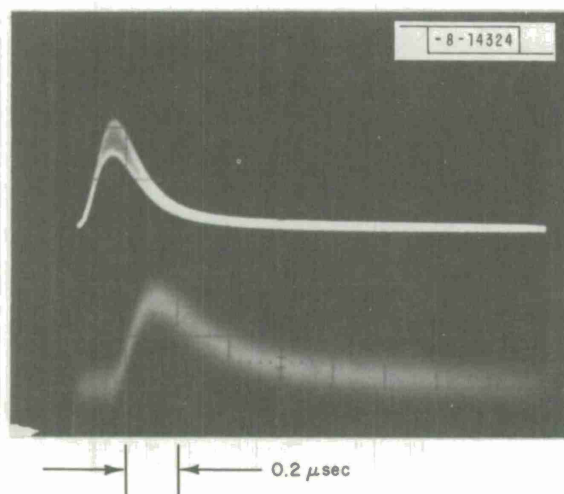


Fig. II-5. Upper trace: second-harmonic signal (Au:Ge detector). Lower trace: second-harmonic signal after reflection from topographic target 23 m distant (InSb detector).

The pulsed outputs shown in Fig. II-5 were obtained using the passively Q-switched folded CO_2 laser previously described²⁴ to pump the CdGeAs_2 crystal. The pulse repetition rate was 10 kHz, with an average power output at the doubled frequency of 0.5 W; after passage through the beam splitter this corresponds to 50 $\mu\text{J}/\text{pulse}$. The noise level of the reflected signal is determined by the dark current of the InSb detector.

The passively Q-switched CO_2 laser used in the above experiment will be inappropriate as a primary source in a portable LIDAR system for several reasons which include: (1) passive Q-switching is restricted to frequencies characteristic of the absorber gas; (2) the high repetition rates generally characteristic of passively Q-switched lasers, with the concomitant reduction in energy per pulse, are distinctly disadvantageous in a direct-detection system which is dark-current-limited since, for such systems in pulsed operation with constant average power, a higher signal-to-noise ratio is obtained with increasing peak power;²⁵ and (3) the laser is water-cooled and extremely bulky. In view of these limitations, we are now engaged in designing a grating-controlled version of a mini-TEA laser.

N. Menyuk
P. F. Moulton
G. W. Iseler

D. GRATING-TUNING OF THE O^{13}CS AND C_2H_2 LASERS

We have previously demonstrated laser action in a number of molecules using an optical pumping technique where vibrational modes of molecules are selectively excited by resonant vibrational energy transfer from CO gas excited by frequency doubled CO_2 laser radiation.^{26,22}

By inserting a grating into the laser cavity, these optically pumped lasers can be operated on specific vibration-rotation transitions. Here we report grating-tuning of the $O^{13}CS$ and C_2H_2 lasers which operate in a wavelength region that is important for some of the proposed laser schemes for isotopic enrichment of uranium.²⁷

We have measured the frequencies of a total of 53 $O^{13}CS$ laser lines between 8.56 and 8.78 μm using a 1-m Jarrell-Ash spectrometer. The accuracy of the frequency measurements is approximately $\pm 0.05 \text{ cm}^{-1}$. In order to identify the observed laser lines, it was necessary to determine the band center of the $O^{13}CS$ $00^0 1 \rightarrow 10^0 0$ transition. We measured the band center of the $10^0 0 \rightarrow 00^0 0$ transition using a 1-m spectrometer equipped with a Nernst glower and a 10-cm absorption cell filled with 50 Torr of $O^{13}CS$. The measured band center at 854.49 cm^{-1} agrees well with the reported value of 854.45 cm^{-1} by Fayt and Vandenhoute,²⁸ but it disagrees with the values of 852.6 and 853.9 cm^{-1} given by Callomon and Thompson²⁹ and by Dorman and Lin,³⁰ respectively. The band center of the $00^0 1 \rightarrow 00^0 0$ transition at 2009.249 cm^{-1} has been measured by Maki *et al.*³¹ Combining this result with our measurement for the $10^0 0$ mode gives a band center for the $00^0 1 \rightarrow 10^0 0$ laser transition of 1154.76 cm^{-1} . With this value, the J assignments for the measured laser lines can be made unambiguously.

The $O^{13}CS$ laser frequencies can be calculated using the expression

$$\begin{aligned} \nu(J) = & \nu_0 + (B_{001} + B_{100})m + [(B_{001} - B_{100}) - (D_{001} - D_{100})]m^2 \\ & - 2(D_{001} + D_{100})m^3 - (D_{001} - D_{100})m^4 \end{aligned} \quad (\text{II-1})$$

where $m = J + 1$ ($J \geq 0$) for an R-branch transition, and $m = -J$ ($J \geq 1$) for a P-branch transition. The rotational constants are $B_{001} = 0.2010604 \text{ cm}^{-1}$ and $B_{100} = 0.2016040 \text{ cm}^{-1}$ (Ref. 28), and $D_{001} = 4.33 \times 10^{-8} \text{ cm}^{-1}$ and $D_{100} = 4.68 \times 10^{-8} \text{ cm}^{-1}$ (Ref. 32). We determine the band center ν_0 in Eq. (II-1) by fitting the expression to the measured laser frequencies. This gives $\nu_0 = 1154.71 \text{ cm}^{-1}$, which agrees well with our preliminary measurement of 1154.76 cm^{-1} . Varying $B_{100} + B_{001}$ in addition to ν_0 does not improve significantly the fit between the measured and calculated frequencies which are listed in Table II-2.

When the C_2H_2 laser was operated without a grating, four lines belonging to the Q-branch of the $01000 \rightarrow 00001^1$ transition were observed near $8.04 \mu m$ (Ref. 22). With grating operation we observed six Q-branch transitions [Q(7), Q(9), Q(11), Q(13), Q(15), and Q(17)] between 8.03 and $8.05 \mu m$, and four P-branch transitions [P(8), P(10), P(12), and P(14)] between 8.16 and $8.26 \mu m$. No laser action was observed on the R-branch, probably because of absorption in C_2H_2 between 7 and $8 \mu m$ associated with the $\nu_4 + \nu_5$ combination band. The measured laser frequencies agree well with the reported hot-band absorption measurements for the C_2H_2 $01000 \rightarrow 00001^1$ transition.³³

H. Kildal

E. SECOND VIBRATIONAL OVERTONE ABSORPTION SPECTRUM OF THE ν_3 MODE OF SF_6

The recent success in isotope-selective photodissociation of the SF_6 molecule when it is subjected to intense CO_2 laser radiation^{34,35} has generated considerable interest in the spectroscopic properties of the SF_6 molecule.³⁶⁻⁴⁰ Several theoretical models have been suggested to describe the photodissociation process;³⁹⁻⁴⁶ in order to test these models accurate spectroscopic constants are necessary. They are also useful for understanding the recently measured spectral dependence of the third-order susceptibility tensor for SF_6 (Refs. 47 and 48).

TABLE II-2
 $O^{13}CS\ 00^0_1 \rightarrow 10^0_0$ LASER LINES
(in vacuum wavenumber)

J	R(J)			P(J)		
	Measured	Calculated	Difference	Measured	Calculated	Difference
11	1159.48	1159.46	0.02	1150.28	1150.22	0.06
12	1159.85	1159.85	0.00	1149.83	1149.80	0.03
13	1160.23	1160.24	-0.01	1149.31	1149.38	-0.07
14	1160.64	1160.63	0.01	1148.96	1148.97	-0.01
15	1161.03	1161.01	0.02	1148.55	1148.55	0.00
16	1161.43	1161.40	0.03	1148.20	1148.13	0.07
17	1161.78	1161.78	0.00	1147.72	1147.71	0.01
18	1162.10	1162.16	-0.06	1147.29	1147.29	0.00
19	1162.56	1162.55	0.01	1146.86	1146.87	-0.01
20	1162.94	1162.93	0.01	1146.45	1146.44	0.01
21	1163.25	1163.30	-0.05	1146.04	1146.02	0.02
22	1163.67	1163.68	-0.01	1145.53	1145.59	-0.06
23	1164.03	1164.06	-0.03	1145.17	1145.16	0.01
24	1164.49	1164.44	0.05	1144.75	1144.74	0.01
25	1164.89	1164.81	0.08	1144.31	1144.31	0.00
26	1165.18	1165.18	0.00	1143.87	1143.88	-0.01
27	1165.60	1165.56	0.04	1143.50	1143.45	0.05
28	1165.93	1165.93	0.00	1142.91	1143.02	-0.11
29	1166.30	1166.30	0.00	1142.53	1142.58	-0.05
30	1166.69	1166.67	0.02	1142.23	1142.15	0.08
31	1167.01	1167.04	-0.03	1141.76	1141.71	0.05
32	1167.38	1167.40	-0.02	1141.31	1141.28	0.03
33	1167.75	1167.77	-0.02	1140.86	1140.84	0.02
34	1168.09	1168.14	-0.05	1140.42	1140.40	0.02
35	1168.46	1168.50	-0.04	1139.94	1139.96	-0.02
36				1139.52	1139.52	0.00
37				1139.04	1139.08	-0.04
38				1138.58	1138.64	-0.06

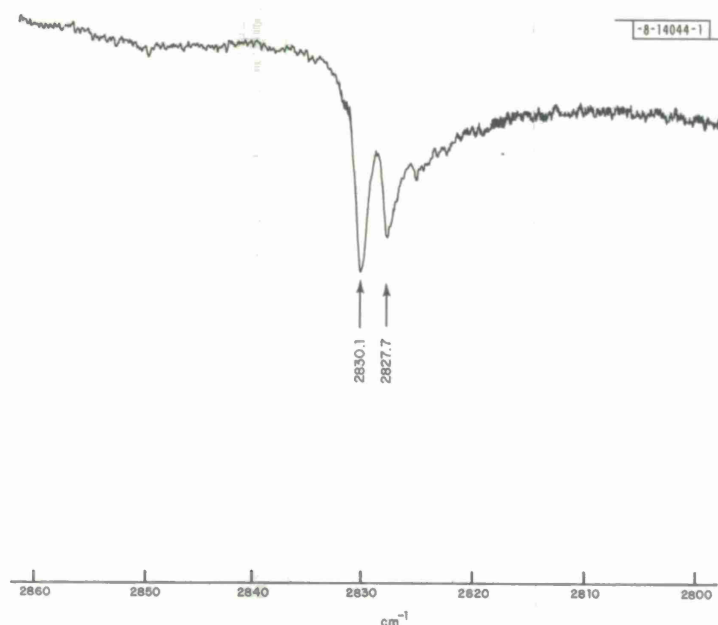


Fig. II-6. Absorption spectrum near $3.5\ \mu\text{m}$ of 200-Torr SF_6 in a 110-cm cell at 200 K.

Here we report measurements of the second vibrational overtone absorption spectrum of the ν_3 mode of SF_6 using a 1-m grating spectrometer. The spectrum is shown in Fig. II-6. It was recorded with the grating in the third order using a gas cell cooled by a circulating dry-ice and methanol mixture. For the purpose of calibration, the fundamental ν_3 spectrum was also recorded. The measured peak position of the Q-branch at $947.92\ \text{cm}^{-1}$ was in good agreement with previously published results.^{36,49} The second overtone transition has a Q-branch at $2830.1\ \text{cm}^{-1}$. Varying the temperature of the absorption cell showed that the additional structure on the low-frequency side of the Q-branch is due to hot-band transitions. The peak at $2827.7\ \text{cm}^{-1}$ is probably the Q-branch associated with the $(3\nu_3 + \nu_6) \rightarrow \nu_6$ transition.⁵⁰ The frequency difference between the $3\nu_3$ and the $(3\nu_3 + \nu_6) \rightarrow \nu_6$ transitions is equal to $3X_{36}$ (Ref. 51) which gives $X_{36} = 0.8\ \text{cm}^{-1}$. This is in reasonable agreement with $X_{36} = 1.0\ \text{cm}^{-1}$ determined from the absorption spectrum near the fundamental ν_3 transition.^{38,50}

The anharmonic potential with octahedral symmetry in SF_6 splits the degenerate $3\nu_3$ vibration into four levels with symmetries of A_{2u} , F_{2u} , F_{1u} , and F_{1u} , respectively (Refs. 39 and 40, see also Ref. 52). The positions of the $3\nu_3$ levels depend on both the anharmonicity X_{33} and the Hecht vibrational splitting parameters G_{33} and T_{33} (Ref. 52). From group theory, it follows that transitions from the ground state are allowed only to levels with F_{1u} symmetry, so there can be at most two second vibrational overtone transitions to the $3\nu_3$ level. Experimentally, only one transition is observed. This implies that either the splitting of the two F_{1u} levels is smaller than the width of the Q-branch, or that the dipole moments for transitions to the two F_{1u} levels are very different. The first case is considered unlikely since this would require both G_{33} and T_{33} less than a few tenths of cm^{-1} .

In the limit when $G_{33} \gg T_{33}$, the two F_{4u} levels have vibrational angular momenta of $l = 1$ and $l = 3$, respectively. In this case, only a single second vibrational overtone transition is allowed because of the selection rule $\Delta l = 1$ (Ref. 39). In the more general case where T_{33} is not negligible compared with G_{33} , the two states have mixed wavefunctions with both $l = 1$ and $l = 3$ characters. A more-detailed calculation is necessary to see if one of the dipole moments remains small compared with the other. If we assume that $G_{33} \gg T_{33}$, then the frequency of the second overtone transition is given by $3\nu_3 + 6X_{33} - 4G_{33}$, where ν_3 is the frequency of the fundamental vibrational transition.⁵² Our measurement then gives $X'_{33} = X_{33} - 2/3 G_{33} = -2.3 \text{ cm}^{-1}$.

When SF_6 is dissolved in liquid oxygen⁵³ or argon,⁵⁴ only one $3\nu_3$ transition is observed. The anharmonicity, however, differs significantly from the gas-phase measurements. Again assuming $G_{33} \gg T_{33}$, the liquid spectra give $X'_{33} = -3.1 \text{ cm}^{-1}$ (Ref. 54) in contrast to our gas data. The latter value has been used in Ref. 38 in discussing gas-phase spectra. Recently, Nowak and Lyman,⁵⁵ neglecting the octahedral splittings, have estimated that $X'_{33} = -1.2 \text{ cm}^{-1}$ by analyzing the band contours of the ν_3 absorption in shock-heated SF_6 . This disagrees with our direct measurements.

The $3\nu_3$ energy levels with F_{4u} symmetry are calculated by Cantrell and Galbraith³⁹ to lie at 2820 and 2836 cm^{-1} , respectively, while Jensen *et al.*⁴⁰ obtain 2820.3 and 2837.5 cm^{-1} for the same two levels. In contrast, the measured position of one of the levels is at 2830.1 cm^{-1} . This disagreement indicates that the basic spectroscopic parameters for SF_6 , which are important for any quantitative calculation of the photodissociation, are not yet firmly established.

H. Kildal

F. VIBRATIONAL ENERGY RELAXATION OF CH_3F DISSOLVED IN LIQUID O_2 AND Ar

In an earlier report⁵⁶ we discussed some preliminary measurements of the vibrational relaxation times of the polyatomic molecules CH_3F and SF_6 in liquid Ar and O_2 hosts. Here we report more-accurate measurements of CH_3F relaxation times measured by both saturation and double-resonance techniques. Using the double-resonance technique, an induced $\nu_3 \rightarrow 2\nu_3$ absorption is observed; the measured anharmonicity is in good agreement with the gas-phase literature value.

These measurements are of interest because they will materially increase our knowledge and understanding of collisional vibration transfer processes in the liquid phase. These measurements may also aid in the interpretation of gas-phase results. Due to the low translational temperature in cryogenic liquids, the thermal equilibrium populations of excited vibrational levels are reduced to negligible values for all but the lowest frequency modes, and, further, some of the multiple pathways for vibrational relaxation that complicate the interpretation of the gas-phase results are eliminated.

Significant practical implications may also follow. As has recently been pointed out,⁵⁷⁻⁵⁹ the infrared spectroscopy of complex polyatomics can be considerably simplified in these cryogenic liquid media. These simplifications arise from the elimination of "hot bands" at cryogenic temperatures, and also from the hindering of free rotational motion in the liquid collisional environment. The resulting infrared spectra often exhibit far narrower features than are observed in the gas phase. These narrow, homogeneously broadened, infrared spectral features suggest applications⁶⁰ for optically pumped infrared lasers and for infrared laser

photochemistry and isotope separation. Such applications crucially depend upon energy-transfer rates in these media, which are to a large extent unmeasured and not readily predictable from existing theories.

We have begun a series of measurements on these relaxation processes with the relatively simple polyatomic methyl fluoride (CH_3F), whose spectroscopy and gas-phase energy-transfer processes are well understood, and have examined these energy-transfer processes in the liquid phase for dilute solutions in the cryogenic hosts liquid argon and liquid oxygen. We have used measurements of the saturation of the infrared absorption to obtain vibration-translation (V-T) relaxation times, and have performed infrared double-resonance experiments which give a direct measurement of the V-T time and of the molecular anharmonicity. These experiments are well-suited to the liquid phase since the high-heat capacity and thermal conductivity of the liquid medium effectively eliminate the heating effects which complicate the interpretation of these measurement techniques in the gas phase. Both of these techniques measure the relaxation time of the excited vibrational mode. The double-resonance technique is more accurate since it is a direct time-domain measurement which does not suffer from the uncertainties due to the spatial and temporal variations of the pump pulse that affect the saturation measurements. However, the saturation measurements are much simpler and are applicable over a much wider range of decay times. One of the purposes of this study was to investigate the accuracy of the saturation measurements in a system where double-resonance measurements were also feasible. The results indicate that the saturation technique can be used with reasonable confidence.

Methyl fluoride is a symmetric top molecule whose lowest energy mode, ν_3 at 1040 cm^{-1} , is accessible with CO_2 laser radiation. This nondegenerate mode has a linewidth of approximately 3.7 cm^{-1} in liquid O_2 and 4.4 cm^{-1} in liquid Ar. This linewidth is due predominately to the hindered rotational motion of the relatively light and compact CH_3F molecule about axes perpendicular to the C-F molecular axis. This linewidth in liquid solution should be compared with an overall P-Q-R branch envelope of approximately 100 cm^{-1} in the gas phase at room temperature. Linewidths of heavier molecules, where rotation is more effectively impeded by the liquid environment, are often considerably narrower. For example, the linewidth of the ν_3 mode of SF_6 in liquid O_2 is 0.3 cm^{-1} (Ref. 59).

Solutions of CH_3F in either liquid oxygen or liquid argon were made in a stainless-steel double Dewar with BaF_2 windows and a path length of 4.2 cm. Liquid nitrogen and liquid argon were used as refrigerants. A CO_2 TEA laser served as the pump for both the double-resonance and the saturation measurements. For double-resonance experiments, the TEA laser was operated with a nitrogen lean mix to give partially mode-locked pulses having a FWHM of 100 nsec as measured by a photon drag detector. For measurements of transmission vs incident flux, the TEA laser was operated with a nitrogen rich mix and with a CW gain cell to give a stretched pulse of roughly triangular temporal shape having a FWHM of $2.9\text{ }\mu\text{sec}$ and no rapid temporal structure. Output energies in either mode of operation were typically 40 mJ. The beam was collimated to a diameter of 0.4 cm at the half-power points.

Double-resonance measurements were performed using a grating-tuned, CW CO_2 probe laser with a typical power of 50 mW on a single line. The probe laser beam was propagated through the sample Dewar collinearly with the TEA pump laser. This beam was collimated to a slightly smaller beam diameter of 0.3 cm to insure that the pumping beam could be considered as a plane wave in the data analysis. The probe laser polarization was perpendicular to that of the pump laser; two germanium polarizers were used to attenuate by about 40 dB the

transmitted pump laser beam. The probe laser beam was then passed through a 3/4-m Spex double-grating monochromator, which eliminated any remaining pump signal, and then focused on a Cu:Ge liquid-helium-cooled detector. For measurements of the decay of the transient double-resonance signal, the detector was operated with a 50-ohm load, which allowed the mode-locked spikes of the pump laser (risetime less than 10 nsec) to be resolved; this response was more than adequate to resolve the decay of the double-resonance signal, which occurred with a lifetime of about 500 nsec. For decay-time measurements, the signal from the detector was amplified and fed into a Nicolet Lab 80 signal averager-minicomputer system. Typically, the signals from 100 shots were collected, averaged, and fit to an exponential decay.

Measurements of the spectral dependence of the double-resonance signal were performed with another Cu:Ge detector system having a 500-nsec response time but a higher responsivity, which allowed the double-resonance signal to be read directly from oscilloscope displays. The relative change in transmission was obtained by normalizing the transient signal to the chopped CW signal from the probe laser. The transmission of each sample fill was measured on a Beckman 4250 IR spectrophotometer and used to correct the measured chopped probe laser signal for sample absorption.

Measurements of transmission vs incident energy fluence were made using two cross-calibrated Gen-Tec ED-200 energy meters. In order to minimize pulse-shape variations, the laser energy was varied using CaF_2 attenuators, with the TEA laser voltage remaining fixed.

Figure II-7(a) shows the linear absorption spectrum of the ν_3 mode of CH_3F in liquid oxygen. The line center at $1037.5 \pm 0.2 \text{ cm}^{-1}$ is red-shifted from the gas-phase value of $\nu_0 = 1048.60 \pm 2 \text{ cm}^{-1}$ due to interactions within the liquid environment. Figure II-7(b) shows the

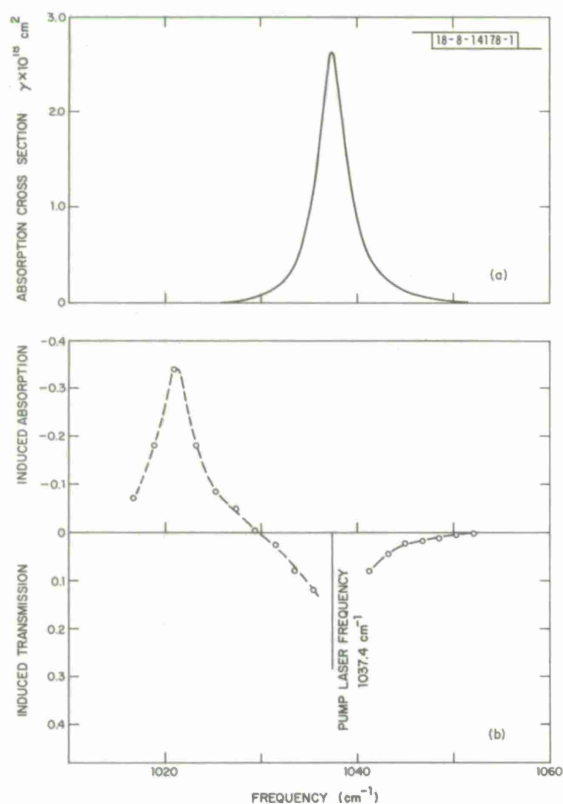


Fig. II-7. (a) Linear and (b) double-resonance absorption spectra of CH_3F in liquid O_2 . For double-resonance spectrum, pump laser energy was 5 mJ and CH_3F concentration was $3 \times 10^{17} \text{ cm}^{-3}$.

double-resonance spectrum for a CH_3F density of $3.5 \times 10^{17} \text{ cm}^{-3}$ in liquid oxygen pumped with the P(30) CO_2 laser line at 1037.4 cm^{-1} . The induced absorption peak at 1021.2 cm^{-1} is due to $\nu_3 \rightarrow 2\nu_3$ transitions; the red shift from the fundamental absorption, $16.3 \pm 1 \text{ cm}^{-1}$, is in good agreement with the gas-phase red shift⁶¹ of 15.84 cm^{-1} . The double-resonance technique thus provides a direct measure of molecular anharmonicity. In the region near the absorption peak, an induced transmission signal is observed because of depletion of the ground-state population.

In order to interpret the observed double-resonance and saturation measurements, a dynamic model of the CH_3F vibrational-level population evolution is necessary. For simplicity, we restrict ourselves to a two-level model for evaluating the dynamics of the ν_3 mode of CH_3F . That is, we assume that the pump laser affects only the $v = 0$ and $v = 1$ levels of the ν_3 mode, and that multiphoton absorption and V-V equilibration processes in $\text{CH}_3\text{F}-\text{CH}_3\text{F}$ collisions may be neglected. This last process is known to be quite rapid in the gas phase⁶² (~ 7 gas kinetic collisions) and is probably responsible for some deviations from simple exponential behavior that are observed in the induced absorption signals at the highest concentration levels that have been investigated. This is particularly true in the liquid Ar solutions where the relaxation times are longer than in liquid O_2 . However, at sufficiently low concentrations, the observed signals were single exponentials over at least one-and-a-half decades; the rate equations which describe the $v = 0$ and $v = 1$ populations (n_0, n_1) are then simply,

$$\frac{dn_0}{dt} - \frac{dn_1}{dt} = \frac{n_1}{\tau} - \frac{I\gamma}{\hbar\omega} (n_0 - n_1) \quad (\text{II-2})$$

and for the pump intensity,

$$\frac{dI}{dz} = -\gamma(n_0 - n_1) I(z) \quad (\text{II-3})$$

where $n_0 + n_1 = N$ (the total CH_3F density), γ is the absorption cross section at the laser frequency $\omega/2\pi$, I is the laser intensity, and $1/\tau$ is the vibrational decay rate. In these equations, n_0 , n_1 , and I are all dependent on the propagation distance in the medium z , as well as time, since the medium is optically thick at the higher densities used for the saturation measurements.

The double-resonance experiments measure the relaxation of the CH_3F molecules back to the ground state after the laser pulse has been switched off ($I = 0$), and the solutions to Eq.(II-2) are just simple exponential decays. The observed double-resonance signals in both the induced absorption and induced transmission regions at low CH_3F concentrations are well-fitted by single exponential decays. The induced absorption signal at 1021.1 cm^{-1} showed a decay time τ of $440 \pm 70 \text{ nsec}$, while the induced transmission signal at 1035.5 cm^{-1} gave $\tau = 375 \pm 35 \text{ nsec}$. Each time represents the average of several runs taken at different pump levels. Detailed, line-by-line measurements of decay time vs frequency indicate that there may be some systematic decrease in τ as the probe frequency is increased. Within the relatively large error bars, we were not able to find any systematic dependence of τ on either CH_3F concentrations or pump intensity. Measurements using a liquid argon host yielded $\tau = 1.30 \pm 0.15 \text{ } \mu\text{sec}$ for the induced transmission signal at 1033.5 cm^{-1} . The relaxation time in liquid argon is more than three times as long as in liquid oxygen.

Figure II-8 shows the results of saturation measurement on CH_3F in a liquid oxygen host, with similar data for an argon host. The observed dependences are both straight lines when plotted in the form $(\ln T/T_s)/(1 - T)$ vs input energy, where $T_s \{= \exp[-\gamma N l]\}$ is the small

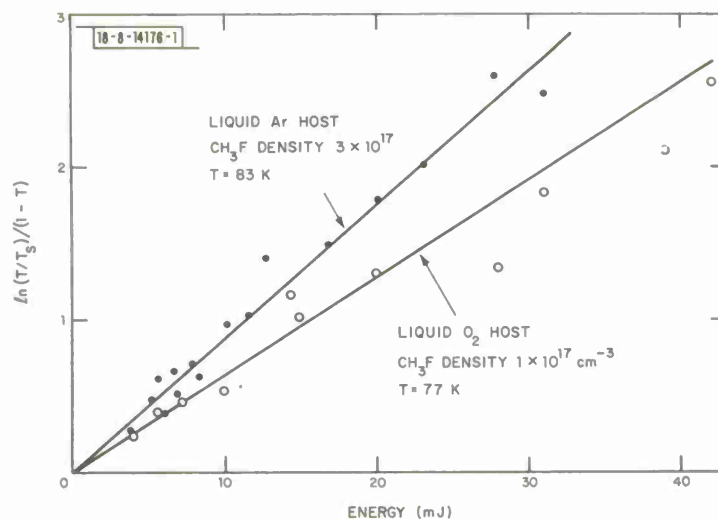


Fig. II-8. Saturation of infrared absorption for dilute solutions of CH_3F in liquid O_2 and liquid Ar. Slopes of these curves are proportional to ν_3 mode lifetimes giving $\tau = 230 \pm 100$ nsec in liquid O_2 and $\tau = 450 \pm 200$ nsec in liquid Ar.

signal transmission of the liquid. This form for displaying the data was chosen since the solution to Eqs. (II-2) and (II-3) for a flat-topped pulse of duration T_p is

$$\frac{\ln T/T_s}{1 - T} = \frac{\mathcal{E} 2\gamma \tau}{\hbar \omega (T_p + \tau) A} \quad (\text{II-4})$$

Here \mathcal{E} is the pulse energy, A is the pulse area, and only the lowest-order correction to the steady-state response due to a finite pulse width has been retained. Since our pulse widths are $5.8 \mu\text{sec}$ (total pulse duration) compared with relaxation times of ~ 400 nsec for CH_3F in liquid O_2 , this is a reasonable assumption. The situation is less clear in liquid Ar where the double-resonance results give a relaxation time of $1.3 \mu\text{sec}$. From the slopes of the curves in Fig. II-8, we deduce CH_3F relaxation times of 230 ± 100 nsec in liquid O_2 and 450 ± 200 nsec in liquid Ar, where the large error bars and the systematic deviation from the double-resonance results stem from uncertainties in defining the pulse length and the spatial extent of the input pulse. It should be noted that, while this saturation measurement is subject to these uncertainties which are not present in the double-resonance experiment, it is a far-simpler and less-involved measurement that is readily carried out with only a laser and an energy meter. This ease of measurement makes it suitable for survey-type measurements where order-of-magnitude relaxation times are desired. Further, since it does not involve time-domain measurements, it can be used over a wide range of decay times. For example, we have used saturation measurements to obtain a relaxation time for SF_6 in liquid oxygen of the order of 50 psec. Note that for this very rapid τ , the steady-state approximation is quite good and, in this sense, the two measurement techniques are complementary.

In summary, we have applied two techniques — double-resonance and saturation measurements — to measure the relaxation times of methyl fluoride in very dilute solution (1 to 10 ppm) in liquids O_2 and Ar. Because of the very high heat capacity of the liquid medium, these

techniques are very well-suited to this environment. This represents the first application of these techniques to the measurement of V-T decay rates in simple liquid media. Due to the relative simplicity of these techniques, especially as compared with the picosecond laser pulse technique which has been the dominant one used previously, these measurements should add rapidly to our knowledge of the liquid collisional environment.

S. R. J. Brueck
T. F. Deutsch
R. M. Osgood, Jr.

G. VIBRATIONAL TWO-PHOTON RESONANCE LINEWIDTHS IN LIQUID MEDIA

In a recent report,⁶³ we derived an expression for the motionally narrowed contribution of the vibration-rotation interaction to the two-photon resonance linewidth in simple diatomic liquids. This resonance describes two-photon processes such as Raman scattering, two-photon absorption, and two-photon-resonant four-wave mixing. The essential physics described by the model was that of an ensemble of vibrational oscillators with an inhomogeneously broadened density of states due to the weak rotational angular momentum dependence of the vibrational frequency. Frequent rotational angular momentum changing collisions, described by the collision parameter τ_J , cause the molecules to sample all the available angular momentum states and thus lead to a motional narrowing of the inhomogeneously broadened lineshape. The calculated lineshape was Lorentzian of width (FWHM)

$$\Gamma = 2\tau_J \left(\frac{\alpha_e}{B_e} \frac{kT}{\hbar} \right)^2$$

where B_e is the rotational term value, α_e is the rotation-vibration coupling constant, T is the temperature, k is Boltzmann's constant, and \hbar is Planck's constant.

Recently, Clouter and Kieft⁶⁴ measured the temperature dependence of the Raman Q-branch linewidth of saturated liquid nitrogen and oxygen over the entire range from the triple point to the critical point. In order to compare this simple theory with their measurements, we require a model for the temperature and density dependence of the rotational correlation time τ_J . One model for collision times that has often been used in liquids is the cell model⁶⁵ which gives

$$\frac{1}{\tau_J} = \frac{(8KT/\pi m)^{1/2}}{2^{1/6} \rho^{-1/3} - \sigma_c} \quad (\text{II-5})$$

where m is the molecular mass, ρ is the molecular density, and σ_c is a collisional diameter. If we adjust σ_c to give a correlation time of 0.35×10^{-12} sec at 77 K, within the range of 0.23 to 0.35×10^{-12} sec found by Van Konynenburg and Steele⁶⁶ in their analysis of the rotational Raman spectrum of liquid nitrogen, the value obtained for σ_c is 3.5×10^{-8} cm and for the Raman linewidth we have $\Gamma = 0.99$ GHz, a significant contribution to the experimental value of 2 GHz (Refs. 65 and 67). Figure II-9 shows the temperature dependence of the Raman linewidth calculated from this cell model, along with the experimental results of Clouter *et al.*⁶⁴

Chandler⁶⁸ recently presented an alternate expression for evaluating the correlation time based on a more-detailed microscopic description of the liquid as an ensemble of "rough" hard spheres. His result is

$$\frac{1}{\tau_J} = \frac{2\sqrt{8}}{2.3} \left(\frac{8KT}{\pi m} \right)^{1/2} \eta \frac{2 - \eta}{2(1 - \eta)^3} \quad (\text{II-6})$$

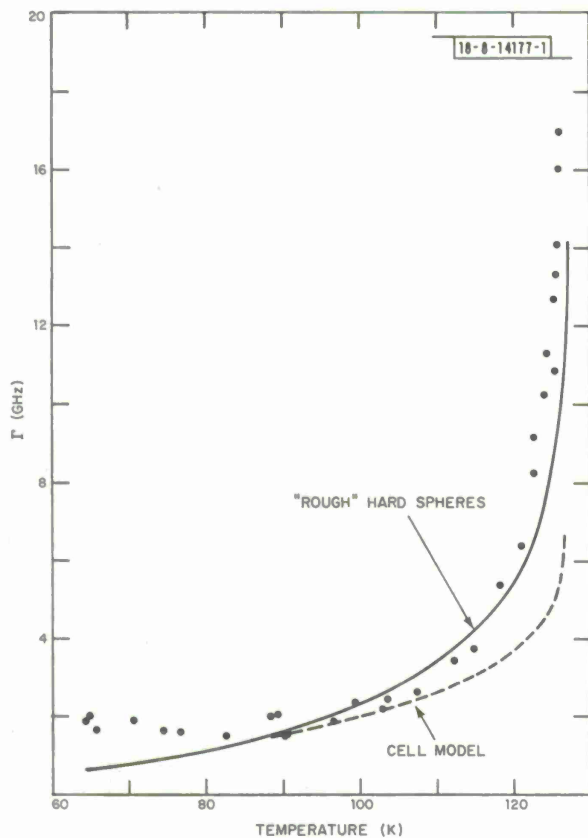


Fig. II-9. Comparison of calculated temperature variation of rotational contribution to Raman linewidth for liquid N_2 with experimental results of Clouter and Kieft.⁶⁴ See text for a description of collisional models used.

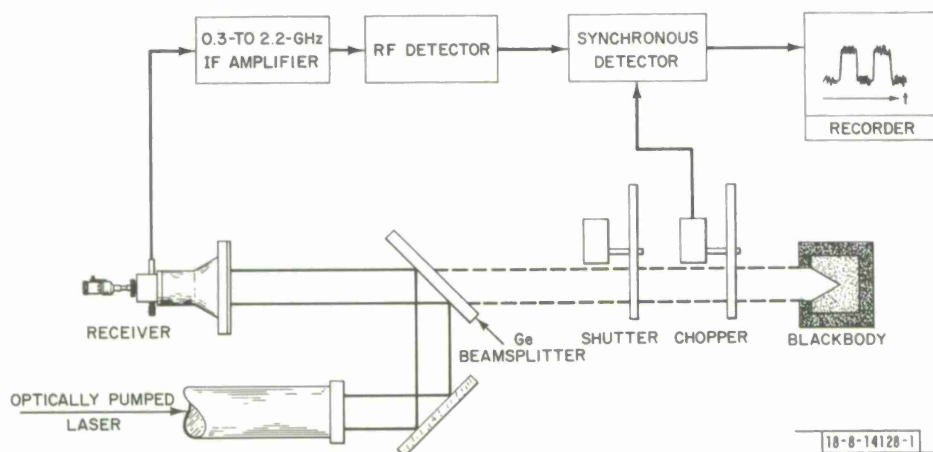


Fig. II-10. Blackbody heterodyne radiometry system for testing diode receivers at $500\ \mu m$.

where $\eta = (\pi/6) \rho \sigma^3$. Again, σ was chosen to force the calculated rate at 77 K to be 0.35 psec. The temperature dependence calculated using this expression for τ_J is also shown in Fig. II-9. It should be noted that, in doing this, we have extended Chandler's model for τ_J beyond its claimed region of validity. Even so, the agreement between theory and experiment is quite good in the region near the critical point. At lower temperatures, the calculated curves for both collision models fall below the experimental results. At this stage of theoretical understanding, it is not possible to say if this is due to an inadequacy of these rotational diffusion models or to the contributions of vibrational dephasing which have not been included here. The results for liquid oxygen are quite similar; the calculated curves are in good agreement with the experiment in the region of the critical point, but fail to reproduce the experimental results at lower temperatures.

Recent measurements⁶⁹ of the Raman linewidth of CO in the neat liquid and diluted in various solvents, N₂, O₂, and Ar at 77 K (83 K for the Ar solvent) further demonstrate the relative importance of the motionally narrowed rotation-vibration interaction and the vibrational dephasing contributions to the Raman linewidth. In dilute solutions in all three solvents the CO Raman linewidth is approximately 0.15 cm⁻¹ wide, increasing to 0.54 cm⁻¹ in the neat liquid. This variation is due to the effects of vibrationally dephasing exchange collisions in highly concentrated solutions which are not possible in the dilute solutions.

In summary, we have developed a simple expression for evaluating the contribution to the linewidth of the isotropic two-photon resonance in diatomic molecules due to the motionally narrowed vibration-rotation interaction, and have demonstrated that this mechanism contributes significantly to the total linewidth. This model can readily be extended to more-complex molecular symmetries. Vibrational dephasing contributions, which we have not included, are also significant, and a full theory of the linewidth must incorporate both effects.

S. R. J. Brueck

H. BLACKBODY HETERODYNE NEP MEASUREMENTS OF SCHOTTKY-DIODE RECEIVERS

Heterodyne radiometric measurements at 500 μ m have been made to determine the sensitivities of recently developed GaAs Schottky-diode receivers.⁷⁰ The Dicke-type radiometer we used is shown in Fig. II-10. This technique is particularly well-suited to this wavelength regime since it reduces the sensitivity measurement to a determination of a minimum detectable temperature difference (ΔT). The NEP is then related to this ΔT by the relationship⁷¹

$$\Delta T = \frac{2 \text{ NEP}}{k \sqrt{B \tau}}$$

where B is the IF bandwidth, and τ is the post-detection integration time. The measurement does not require critical alignment and is independent of polarization. Of greatest importance, however, is the fact that it effectively eliminates the need for difficult absolute submillimeter-power measurements.

Three different receiver configurations were tested in these experiments. The first had a horn-lens (TPX) system to couple submillimeter radiation into the diodes. A germanium beam splitter was then used to introduce the local oscillator from an optically pumped CH₃F laser of about 12 mW output power. Our second system replaced the horn-lens with a quasi-optical mount using a focusing mirror. The third system depended on a second, orthogonal

mirror to couple the local-oscillator radiation into the diode and did not require a beam splitter. Heated cavities and absorbers cooled to liquid nitrogen temperature were utilized as blackbody sources.

From the initial experiments, we have estimated a minimum detectable temperature difference and resulting NEP. Depending on the mount, the particular diode, and the alignment of the system, we obtain system NEPs in the 2 to 6×10^{-18} W/Hz range (double sideband). Our measurements indicate that increasing the local-oscillator power will significantly improve these results. Efforts to further optimize the detectivity and to determine precise values for diode conversion efficiencies are now in progress.

H. R. Fetterman
P. E. Tannenwald
B. J. Clifton

REFERENCES

1. H. G. Danielmeyer, G. Huber, W. W. Krühler, and J. P. Jeser, Appl. Phys. 2, 335 (1973).
2. H. P. Weber and B. C. Tofield, IEEE J. Quantum Electron. QE-11, 368 (1975).
3. H. P. Weber, T. C. Damen, H. G. Danielmeyer, and B. C. Tofield, Appl. Phys. Lett. 22, 534 (1973); S. R. Chinn, J. W. Pierce, and H. Heckscher, IEEE J. Quantum Electron. QE-11, 747 (1975), DDC AD-A017355/9. Other references may be found in the review articles: H. G. Danielmeyer, Festkörperprobleme (Adv. in Solid State Phys.) XV, 253 (1975) and H. P. Weber, Opt. Quant. Electron. 7, 431 (1975).
4. S. R. Chinn, J. W. Pierce, and H. Heckscher, Appl. Opt. 15, 1444 (1976); S. R. Chinn, H. Y-P. Hong, and J. W. Pierce, IEEE J. Quantum Electron. QE-12, 189 (1976), DDC AD-A025591/9; M. Saruwatari, T. Kimura, and K. Otsuka, Appl. Phys. Lett. 29, 291 (1976).
5. M. Saruwatari, T. Kimura, T. Yamada, and J. Nakano, Appl. Phys. Lett. 27, 682 (1975).
6. P. A. Forrester, V. J. Alexander, and H. W. Evans, Opt. Laser Tech. 6, 174 (1974); F. Kobylarz, R. H. Wright, H. Saphow, and N. Yeaman, Proc. 6th Department of Defense Conference on Laser Technology, U.S. Air Force Academy, Colorado Springs, Colorado, March 1976.
7. M. Beucher, Proc. 6th Rare Earth Research Conference, Paris, 1969.
8. S. Jaulmes, C. R. Acad. Sci. C (Paris) 268, 935 (1969).
9. B. C. Tofield, H. P. Weber, and T. C. Damen, Mat. Res. Bull. 9, 435 (1974).
10. H. G. Danielmeyer, H. Jeser, E. Schönherr, and W. Stetter, J. Cryst. Growth 22, 298 (1974).
11. D. C. Miller, L. K. Shick, and C. D. Brandle, J. Cryst. Growth 23, 313 (1974).
12. M. Marais, N. D. Chinh, H. Savary, and J. P. Budin, J. Cryst. Growth 35, 329 (1976).
13. W. K. Zwicker, T. Kovats, and S. R. Chinn, to be presented at the 5th International Conference on Crystal Growth, Boston, Massachusetts, July 1977.
14. H. P. Weber, B. C. Tofield, and P. F. Liao, Phys. Rev. B 11, 1152 (1975); J. P. Budin, A. Milatos-Roufos, N. D. Chinh, and G. LeRoux, J. Appl. Phys. 46, 2867 (1975).

15. J. P. Markiewicz and J. L. Emmett, IEEE J. Quantum Electron. QE-2, 707 (1966).
16. S. Singh, D. C. Miller, J. R. Potopowicz, and L. K. Shick, J. Appl. Phys. 46, 1191 (1975).
17. G. Huber, W. W. Krühler, W. Bludau, and H. G. Danielmeyer, J. Appl. Phys. 46, 3580 (1975).
18. H. Kildal, G. W. Iseler, N. Menyuk, and J. C. Mikkelsen, Topical Meeting on Optical Phenomena in Infrared Materials, Annapolis, Maryland, 1976.
19. H. S. Kwok and E. Yablonovitch, Rev. Sci. Instrum. 46, 814 (1975).
20. E. Yablonovitch and J. Goldhar, Appl. Phys. Lett. 25, 580 (1974).
21. N. Menyuk, G. W. Iseler, and A. Mooradian, Appl. Phys. Lett. 29, 422 (1976), DDC AD-A037622.
22. H. Kildal and T. F. Deutsch, in Tunable Lasers and Applications, A. Mooradian, T. Jaeger, and P. Stokseth, Eds. (Springer-Verlag, New York, 1976), p. 367.
23. G. W. Iseler, H. Kildal, and N. Menyuk, Proc. Third International Conference on Ternary Compounds, Edinburgh, Scotland, April 1977 (to be published in the Institute of Physics Conference Series).
24. Solid State Research Report, Lincoln Laboratory, M.I.T. (1976:4), p. 21, DDC AD-A039175.
25. R. L. Byer, Opt. Quant. Electron. 7, 147 (1975).
26. H. Kildal and T. F. Deutsch, Appl. Phys. Lett. 27, 500 (1975), DDC AD-A024185/1.
27. R. J. Jensen, J. G. Marinuzzi, C. P. Robinson, and S. D. Rockwood, Laser Focus 12, 51 (1976).
28. A. Fayt and R. Vandenhaute, Ann. Soc. Scient. Bruxelles 85, 105 (1971).
29. H. J. Callomon and H. W. Thompson, Proc. Roy. Soc. A222, 431 (1954).
30. F. Dorman and C. C. Lin, J. Mol. Spectrosc. 12, 119 (1964).
31. A. G. Maki, E. K. Plyler, and E. D. Tidwell, J. Res. Natl. Bur. Stand. (U.S.) A 66, 163 (1962).
32. A. G. Maki, private communication.
33. K. F. Palmer, M. E. Mickelson, and K. N. Rao, J. Mol. Spectrosc. 44, 131 (1972).
34. R. V. Ambartsumyan, Yu. A. Gorokhov, V. S. Letokhov, and G. N. Makarov, JETP Lett. 21, 171 (1975).
35. J. L. Lyman, R. J. Jensen, J. Rink, C. P. Robinson, and S. D. Rockwood, Appl. Phys. Lett. 27, 87 (1975).
36. J. P. Aldridge, H. Filip, H. Flicker, R. F. Holland, R. S. McDowell, and N. G. Nereson, J. Mol. Spectrosc. 58, 165 (1975).
37. R. S. McDowell, H. W. Galbraith, B. J. Krohn, C. D. Cantrell, and E. D. Hinkley, Opt. Commun. 17, 178 (1976).
38. R. S. McDowell, J. P. Aldridge, and R. F. Holland, J. Phys. Chem. 80, 1203 (1976).
39. C. D. Cantrell and H. W. Galbraith, Opt. Commun. 18, 513 (1976).
40. C. C. Jensen, W. B. Person, B. J. Krohn, and J. Overend, Opt. Commun. 20, 275 (1977).
41. R. V. Ambartsumyan, Yu. A. Gorokhov, V. S. Letokhov, G. N. Makarov, and A. A. Puretskii, JETP Lett. 23, 22 (1976).
42. N. Bloembergen, C. D. Cantrell, and D. M. Larsen, in Tunable Lasers and Applications, A. Mooradian, T. Jaeger, and P. Stokseth, Eds. (Springer-Verlag, New York, 1976).

43. D. M. Larsen, Opt. Commun. 19, 404 (1976).
44. J. Stone, M. F. Goodman, and D. A. Dows, Chem. Phys. Lett. 44, 411 (1976).
45. _____, J. Chem. Phys. 65, 5062 (1976).
46. S. Mukamel and J. Jortner, J. Chem. Phys. 65, 5204 (1976).
47. H. Kildal and T. F. Deutsch, IEEE J. Quantum Electron. QE-12, 429 (1976), DDC AD-A030985/6.
48. M. H. Kang, K. M. Chung, and M. F. Becker, J. Appl. Phys. 47, 4944 (1976).
49. H. Brunet and M. Perez, J. Mol. Spectrosc. 29, 472 (1969).
50. H. Brunet, IEEE J. Quantum Electron. QE-6, 678 (1970).
51. R. S. McDowell and L. B. Asprey, J. Mol. Spectrosc. 48, 254 (1973).
52. K. T. Hecht, J. Mol. Spectrosc. 5, 355 (1960).
53. V. V. Bertsev, T. D. Kolomiitseva, and N. M. Tsyganenko, Opt. Spectrosc. 37, 263 (1974).
54. S. R. J. Brueck, private communication.
55. A. V. Nowak and J. L. Lyman, J. Quant. Spectrosc. Radiat. Transfer 15, 945 (1975).
56. Solid State Research Report, Lincoln Laboratory, M.I.T. (1977:1), pp. 10-14.
57. V. V. Bertsev, M. O. Bulanin, and T. D. Kolomiitsova, Opt. Spektrosk. 35, 227 (1973) [Opt. Spectrosc. 35, 162 (1973)].
58. R. Akhmedzhanov, V. V. Bertsev, M. O. Bulanin, and L. A. Zhigula, Opt. Spektrosk. 36, 1219 (1974) [Opt. Spectrosc. 36, 709 (1974)].
59. V. V. Bertsev, T. D. Kolomiitsova, and N. M. Tsyganenko, Opt. Spektrosk. 37, 463 (1974) [Opt. Spectrosc. 37, 263 (1974)].
60. Solid State Research Report, Lincoln Laboratory, M.I.T. (1976:3), p. 30, DDC AD-A034647/8.
61. W. L. Smith and I. M. Mills, J. Mol. Spectrosc. 11, 11 (1963).
62. B. L. Earl, P. C. Isoloni, and A. M. Ronn, Chem. Phys. Lett. 39, 95 (1976).
63. Solid State Research Report, Lincoln Laboratory, M.I.T. (1976:4), p. 27, DDC AD-A039175.
64. M. J. Clouter and H. Kieffe, J. Chem. Phys. 66, 1736 (1977).
65. P. K. Davis, J. Chem. Phys. 57, 517 (1972).
66. P. van Konynenburg and W. A. Steele, J. Chem. Phys. 62, 2301 (1975).
67. W. R. L. Clements and B. P. Stoicheff, Appl. Phys. Lett. 12, 246 (1968).
68. D. Chandler, J. Chem. Phys. 60, 3504 (1974).
69. S. R. J. Brueck (to be published).
70. B. J. Clifton, IEEE Trans. Microwave Theory Tech. MTT-25, 457 (1977).
71. B. J. Peyton, A. J. DiNardo, S. C. Cohen, J. H. McElroy, and R. J. Coates, IEEE J. Quantum Electron. QE-11, 569 (1975).

III. MATERIALS RESEARCH

A. GROWTH OF Ni-DOPED MgF_2 SINGLE CRYSTALS

The observation of laser emission from Ni-doped MgF_2 at wavelengths between 1.62 and 1.84 μm , which was reported over 10 years ago by Johnson, Guggenheim, and Thomas,¹ suggests that this material may be useful as a tunable source of coherent infrared radiation. Although large, optical-quality crystals of undoped MgF_2 are routinely grown from the melt in open crucibles, this method cannot be used for the growth of Ni-doped crystals because NiF_2 is too volatile at temperatures near the melting point of MgF_2 (1390°C). Table III-1 lists the vapor pressures at 1400° and 1500°C of MgF_2 (Ref. 2) and NiF_2 (Ref. 3), together with the total pressure values for two dilute MgF_2 - NiF_2 melts calculated for ideal solution behavior. Even for a melt containing only 1-m/o NiF_2 , the total pressure at 1400°C is 10 Torr, of which the partial pressure of NiF_2 is 8.9 Torr.

TABLE III-1 TOTAL VAPOR PRESSURES OF $\text{Mg}_{1-x}\text{Ni}_x\text{F}_2$		
	Pressure (Torr)	
	1400°C	1500°C
MgF_2 (Ref. 2)	1.1	3.8
NiF_2 (Ref. 3)	890	3300
$\text{Mg}_{0.99}\text{Ni}_{0.01}\text{F}_2$	10	37
$\text{Mg}_{0.97}\text{Ni}_{0.03}\text{F}_2$	28	103

The crystals of Ni-doped MgF_2 used by Johnson *et al.*¹ were grown by Guggenheim⁴ in a closed platinum crucible under an HF-He atmosphere. He employed a modified Stockbarger technique with a moving platinum-wound furnace. We have developed a considerably simpler method for growing such crystals in a self-sealing, dense-graphite crucible in a tungsten-element furnace by means of a vertical gradient freeze technique. This method should be applicable to the melt growth of other materials that are too volatile to permit the use of open systems.

The furnace and crucible used for crystal growth are shown schematically in Fig. III-1. As described previously,⁵ the furnace is resistance-heated by means of a tungsten mesh element that is enclosed in a water-cooled, stainless-steel jacket, permitting either vacuum or inert-gas operation. Multilayer molybdenum heat shields are used for thermally insulating the element and the crucible, which is cooled from the bottom by close contact with the water-cooled base of the furnace. To obtain the temperature gradient required for crystal growth, ten heat shields are placed across the top of the hot zone, and this zone is insulated along its length by means of a spiral which is wound so that the number of molybdenum layers decreases continuously from ten at the top to two at the bottom.

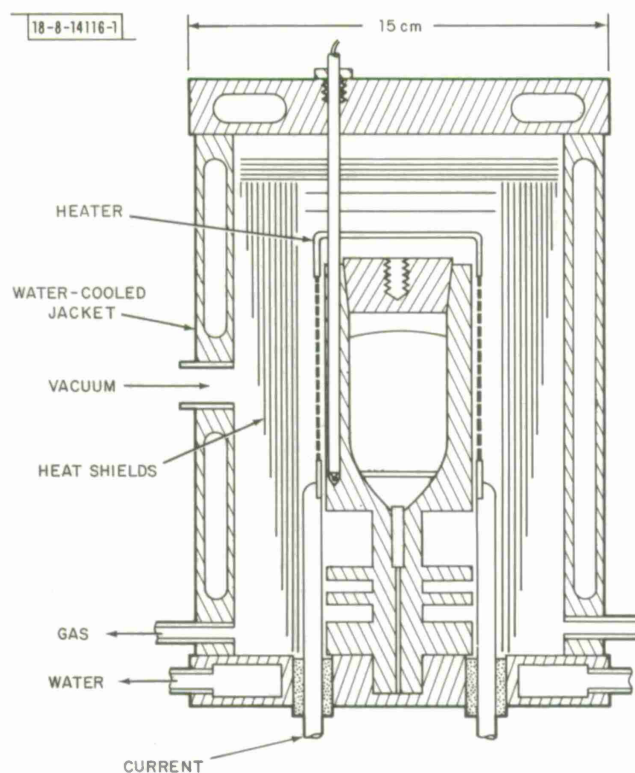


Fig. III-1. Schematic diagram of resistance furnace and graphite crucible used for growth of Ni-doped MgF_2 single crystals.

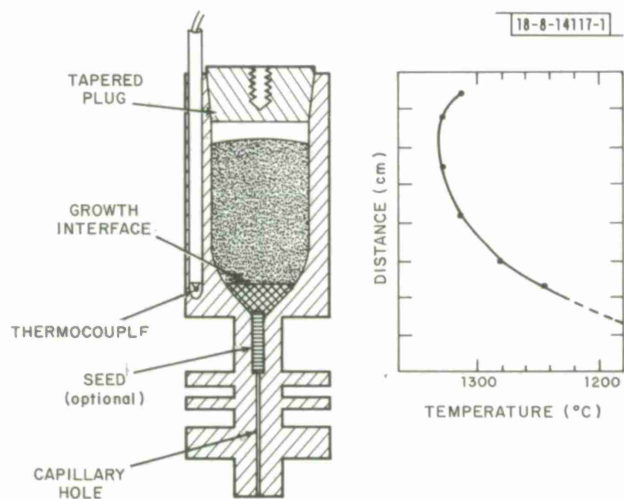


Fig. III-2. Schematic diagram of graphite growth crucible (left side) and temperature profile measured inside crucible wall before reaching growth temperature (right side).

A labeled diagram of the graphite crucible is shown on the left side of Fig. III-2. The internal cavity is tapered at the top to permit sealing with a close-fitting graphite plug. Below the cylindrical center section the cavity is again tapered, ending in an open capillary 1 mm in diameter and about 5 cm long. (In the optional version of the crucible shown in Fig. III-2, the top of the capillary is enlarged to permit insertion of a single-crystal seed.) A well in the crucible wall contains a thermocouple for monitoring the crucible temperature; the thermocouple is not used for temperature control, which is achieved by controlling the input power to the furnace.

The vertical temperature profile during crystal growth has the form shown on the right side of Fig. III-2. The temperature is highest near the top of the crucible and decreases smoothly toward the bottom, while the temperature gradient increases in this direction, reaching a value of about $40^{\circ}\text{C}/\text{cm}$ at the top of the capillary. (The profile plotted in Fig. III-2 was obtained by measurements made with the crucible thermocouple during an actual growth run. However, it was taken before the temperature had reached the melting point of MgF_2 and therefore does not correspond to the position of the growth interface indicated in the diagram of the crucible.)

All but two of the growth runs have been made without seeding. The interior of the crucible and the tapered plug are first polished with carborundum paper to a mirror finish, washed vigorously with soap and water to remove loose graphite particles, rinsed with alcohol, and dried in air at about 200°C . The crucible is loaded with a coarse mixture of optical-grade MgF_2 and NiF_2 (BDH Chemicals, Poole, England), and the plug is sealed in place with epoxy cement. The crucible is then placed in the furnace and evacuated by reducing the furnace pressure to about 0.1 Torr. The temperature at the monitoring thermocouple is raised to about 1200°C , the furnace is back-filled with Ar at atmospheric pressure, and heating is continued. When the charge begins to melt, liquid MgF_2 runs down into the capillary where it freezes to form a plug that seals the crucible. After the temperature reaches 1450°C , it is rapidly decreased to 1100°C in order to refreeze the charge. During cooling, a thermal arrest is generally observed between 1300° and 1100°C , indicating that under these conditions the melt supercools by 100° to 300°C . The furnace is next reheated to 1425°C to produce an interface, located in the capillary, where the molten charge is in equilibrium with solid MgF_2 . The charge is then frozen directionally by lowering the temperature at about $20^{\circ}\text{C}/\text{hr}$ so that the interface moves up through the melt, initially at about 5 mm/hr and then at gradually higher rates as the temperature gradient decreases toward the top of the crucible. Although the material that initially freezes in the capillary is highly polycrystalline, the boule becomes monocrystalline even before the interface enters the tapered section of the crucible. After the charge is completely solidified, the furnace is cooled to room temperature at $20^{\circ}\text{C}/\text{hr}$. (When a seed is used, the procedure is similar except that growth is initiated after the temperature is first raised to 1425°C , without freezing and then remelting the charge.)

A number of single-crystal boules 2.5 cm in diameter and 7.5 cm long have been grown from charges of MgF_2 doped with either 1 or 3 wt% NiF_2 . The growth axis of the unseeded boules was about 30° from the tetragonal c-axis, while the two seeded crystals were grown parallel to the c-axis. The seeded crystals both cracked extensively during cutting, possibly due to strain incorporated during solidification or cooling. The as-grown boules are uniformly pale green in color, indicating that the distribution coefficient for Ni is close to unity, which is consistent with the report of Ferguson *et al.*⁶ that Ni is substituted in MgF_2 without evidence of

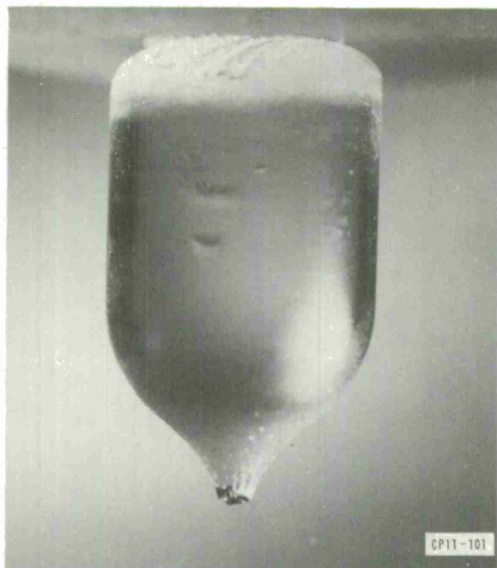
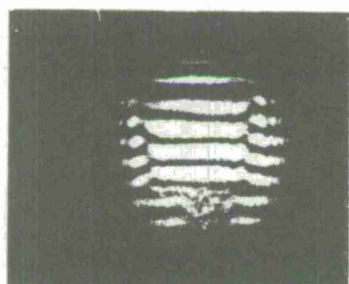
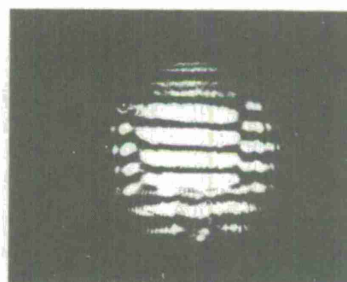


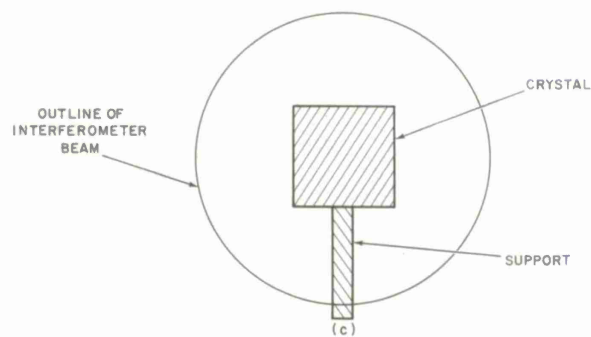
Fig. III-3. Single crystal of Ni-doped MgF_2 2.5 cm in diameter and 7.5 cm long.



(a)



(b)



10-8-14118-1

Fig. III-4. (a, b) Mach-Zender interference patterns for two rods cut from a single crystal of Ni-doped MgF_2 . (c) Location of sample rod in interferometer beam.

segregation. An electron microprobe analysis was performed on a longitudinal slice cut from one of the unseeded boules grown from a charge containing 3 wt% (1.95 m/o) NiF_2 . According to this analysis, the NiF_2 content along the axis of the slice is 2.7 ± 0.08 wt%, a relative variation of 3 percent, while the concentration gradually decreases to 0.9 wt% at the outer edge. We have not determined whether such a radial gradient is typical. Mass spectrographic analysis of this crystal gave the concentrations of the principal impurities as (in ppm atomic): O - 800, Fe - 80, and Mn - 30. No other impurity had a concentration of more than 30 ppma.

The boules obtained by using the growth parameters specified above are of excellent optical quality over almost their entire length, although the last portion to freeze generally contains gaseous inclusions, cracks, or low-angle grain boundaries that are visible between crossed polarizers. These imperfections may result from the increase in growth rate that occurs toward the top of the charge, or from an increase in impurity concentration in the melt due to rejection of impurities from the growing crystal. One of the unseeded boules is shown in Fig. III-3. Imperfections are restricted to a narrow region at the top of the boule, where they result in the dendritic growth that is visible on the top surface in the photograph.

For a more critical check of optical quality, rods cut from one of the boules have been examined by an interferometric method. The rods are $5 \times 5 \text{ mm}^2$ in cross section and 2 cm long, with their length perpendicular to the c-axis and their ends polished flat and parallel. Each rod was placed in one arm of a Mach-Zender interferometer with a He-Ne laser source. Figure III-4(a-c) shows the interference patterns obtained for two of the rods, together with a diagram showing the location of the rod in the interferometer beam. The straightness and parallelism of the fringes produced by the portion of the beam passing through the rods demonstrate the excellent optical quality of the crystal.

T. B. Reed
R. E. Fahey
P. F. Moulton

B. COMPOSITIONS AND LASER WAVELENGTHS OF $\text{Ga}_x\text{In}_{1-x}\text{As}_y\text{P}_{1-y}$ LAYERS LATTICE-MATCHED TO InP SUBSTRATES

The preparation of device-quality semiconductor epitaxial layers requires that the lattice constants of the grown layers and their substrates be closely matched. Lattice matching is especially critical for the effective operation of double-heterostructure (DH) diode lasers because mismatch between the active region and the adjacent barrier layers results in the formation of defects that seriously reduce efficiency and can shorten device lifetime. Since quaternary $\text{Ga}_x\text{In}_{1-x}\text{As}_y\text{P}_{1-y}$ alloys can be exactly lattice-matched to InP over a range of compositions that give energy gaps corresponding to any wavelength between 0.92 and $1.7 \mu\text{m}$, these alloys are of particular interest for optoelectronic devices operating in this spectral region. Both photoemissive devices⁷ and long-lived DH diode lasers operating continuously at room temperature^{8,9} have been fabricated with $\text{Ga}_x\text{In}_{1-x}\text{As}_y\text{P}_{1-y}$ layers grown by liquid-phase epitaxy (LPE) on InP substrates, and avalanche photodiode detectors are under development.

In the $\text{Ga}_x\text{In}_{1-x}\text{As}_y\text{P}_{1-y}$ alloys, both x and y can take any value between 0 and 1, with each varying independently of the other. For those alloys having the same lattice constant as InP, however, x and y are no longer independent. To select the particular alloy composition required for $\text{Ga}_x\text{In}_{1-x}\text{As}_y\text{P}_{1-y}$ /InP devices operating at a specific wavelength, it is necessary to know the functional relationship of x to y and the composition-wavelength relationship for

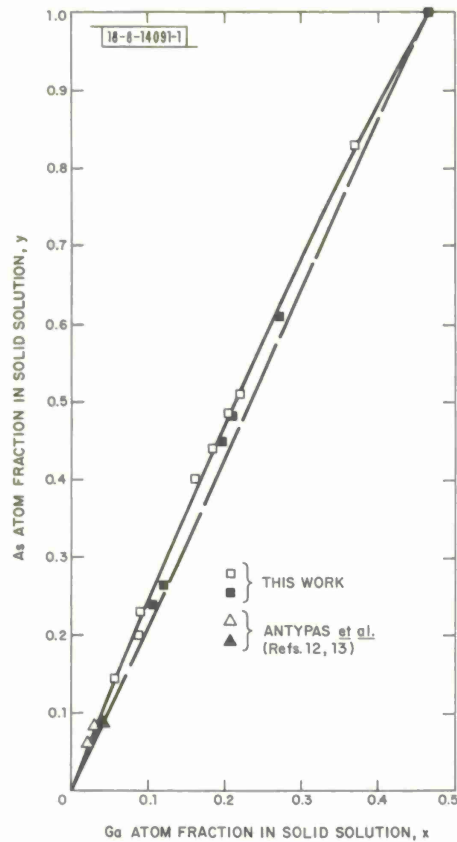


Fig. III-5. Relationship between composition parameters x and y for LPE $\text{Ga}_x\text{In}_{1-x}\text{As}_y\text{P}_{1-y}$ epilayers lattice-matched to InP substrates. Open and closed symbols refer to layers with $0 \leq \Delta a/a \leq +0.06$ percent and $0 \geq \Delta a/a \geq -0.06$ percent, respectively, where $\Delta a/a$ is relative mismatch between layer and substrate.

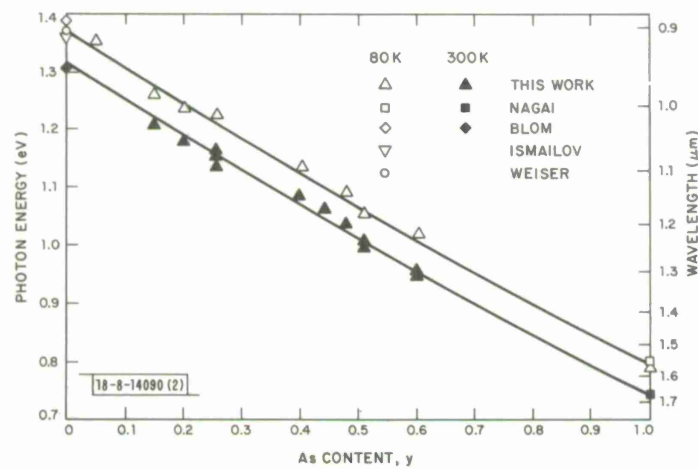


Fig. III-6. Emission wavelength and corresponding photon energy as a function of composition parameter y for DH diode lasers with $\text{Ga}_x\text{In}_{1-x}\text{As}_y\text{P}_{1-y}$ active region lattice-matched to InP.

the lattice-matched alloys. Although scattered experimental data are available, no systematic determination of these relationships has been reported. We have now carried out such a determination.

To determine the x - y relationship for lattice-matched $\text{Ga}_x\text{In}_{1-x}\text{As}_y\text{P}_{1-y}$ alloys, LPE layers 2 to 3 μm thick were grown on (111)B- or (100)-oriented single-crystal InP substrates by a supercooling technique, described previously,¹⁰ which uses a high-purity graphite slider boat. The alloy composition is a sensitive function of the composition of the growth solution, the degree to which the solution is supercooled, and the orientation.¹¹ An InP buffer layer was grown immediately before the alloy epilayer in order to minimize imperfections due to thermal etching of the substrate during heating. The lattice constant of the alloy was found by using an x-ray diffractometer, employing Cu K_α radiation, to measure the angular position of the (444) or (600) diffraction line, depending on whether the orientation was (111)B or (100). The corresponding line of the InP substrate was used as an internal standard. The growth parameters were adjusted until the lattice mismatch $\Delta a/a$ (where Δa is equal to the lattice constant of the alloy epilayer minus the lattice constant of InP, $a = 5.8685 \text{ \AA}$) was 0.06 percent or less. The composition of the alloy was then measured by using electron microprobe analysis to determine the concentrations of all four elements, employing GaAs and InP as standards.

The measured compositions of the lattice-matched $\text{Ga}_x\text{In}_{1-x}\text{As}_y\text{P}_{1-y}$ epilayers are shown in Fig. III-5, where x is plotted as a function of y . The open and closed squares were obtained for epilayers with $0 \leq \Delta a/a \leq +0.06$ percent and $0 \geq \Delta a/a \geq -0.06$ percent, respectively. Three data points obtained by Antypas and co-workers^{12,13} for compositions close to InP are also shown, using the same convention for open and closed points. For the P-free limit ($y = 1$) of the lattice-matching range, the value of x is 0.465, in good agreement with the value of 0.47 quoted in the literature.^{14,15} The data are well-represented by the solid curve shown, which corresponds to the expression $x = 0.40y + 0.067y^2$. This curve lies slightly below the dashed straight line drawn between the end points at $y = 0$ and $y = 1$.

The composition-wavelength relationship for lattice-matched $\text{Ga}_x\text{In}_{1-x}\text{As}_y\text{P}_{1-y}$ layers was determined by measuring the emission wavelengths of broad-area DH diode lasers operated under pulsed conditions. To prepare the lasers, an InP buffer layer, a lattice-matched $\text{Ga}_x\text{In}_{1-x}\text{As}_y\text{P}_{1-y}$ active region 0.2 to 0.5 μm thick, and an upper InP barrier layer were grown successively by LPE on (111)B- or (100)-oriented InP substrates. The active region was doped with Sn to $3 \times 10^{17} \text{ cm}^{-3}$, and the upper InP layer was doped with Zn to $3 \times 10^{18} \text{ cm}^{-3}$. Figure III-6 shows the wavelengths and corresponding photon energies of the laser emission peaks measured at 300 and 80 K as a function of the value of y for the active region. (It has been assumed that this value is the same as that measured by electron microprobe analysis for a layer 2 to 3 μm thick, with $\Delta a/a \leq 0.06$ percent, grown under the same conditions.) For $y = 0.05$ and $y = 1$, laser emission was obtained at 80 K but not at 300 K. Figure III-6 also includes the results reported by Weiser and Levitt¹⁶ and by Ismailov *et al.*¹⁷ for InP ($y = 0$) homojunction diode lasers operated at 80 K, by Blom and Woodall¹⁸ for spontaneous emission of InP LEDs at 300 and 80 K, and by Nagai and Noguchi¹⁵ for laser emission at 80 K and spontaneous emission at 300 K of DH $\text{Ga}_x\text{In}_{1-x}\text{As}/\text{InP}$ diode lasers. Over the whole composition range, the data are well-represented by two parallel curves, with the curve for 80 K lying 57 meV above the one for 300 K. The photon energies at 300 K are given by $h\nu \text{ (eV)} = 1.307 - 0.60y + 0.03y^2$. The emission energies for DH $\text{Ga}_{0.47}\text{In}_{0.53}\text{As}/\text{InP}$ diodes are close to the photon energies for this

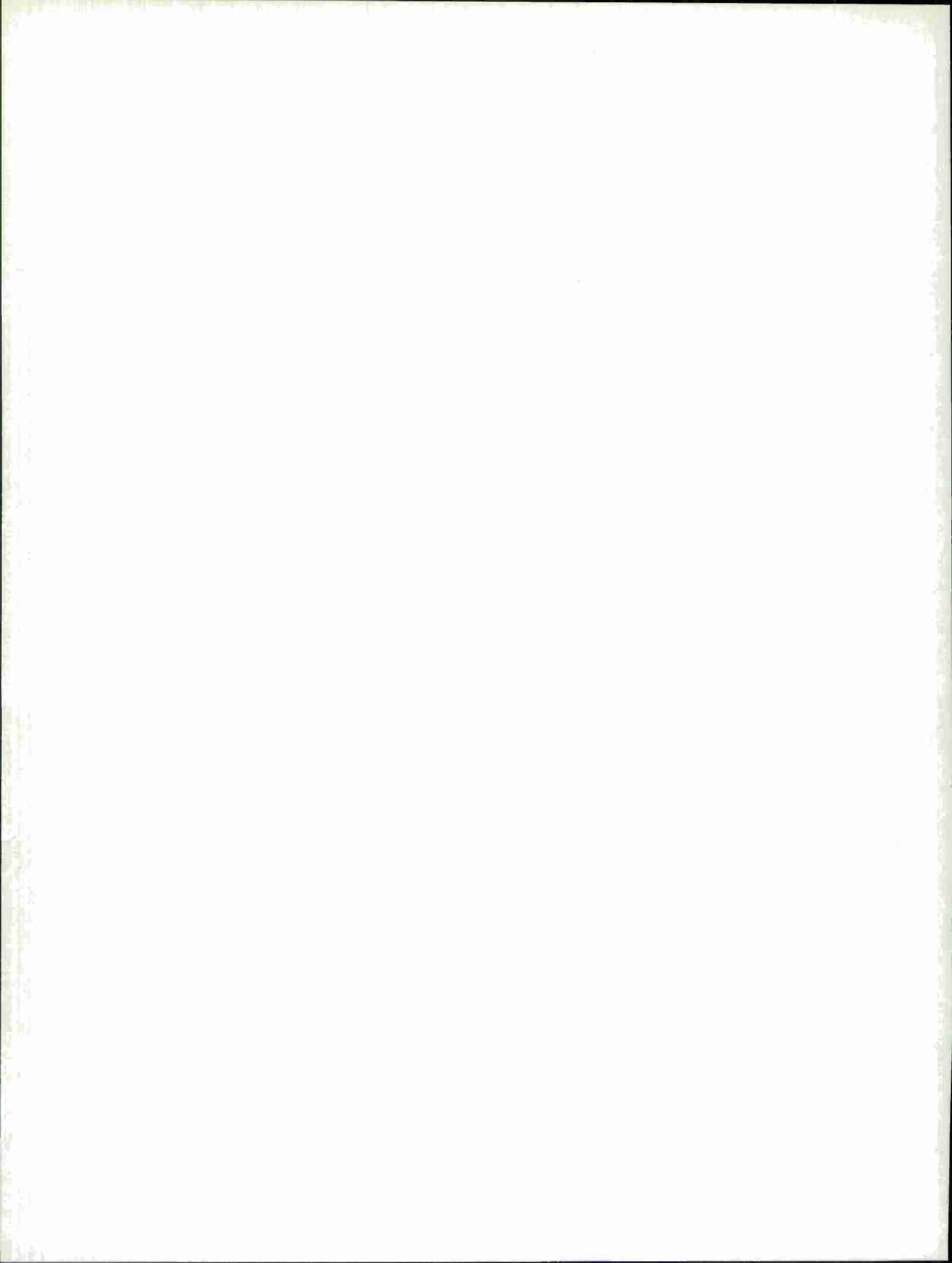
ternary composition interpolated from published curves¹⁹ based on infrared transmission and photoluminescence data for $\text{Ga}_{1-x}\text{In}_x\text{As}$ alloys.

The curves in Fig. III-6 give the photon energies for laser emission of InP at 300 and 80 K as 1.307 and 1.364 eV, respectively. These values are lower by 44 and 50 meV, respectively, than the energy gap values for InP at these temperatures determined by optical absorption and photoluminescence measurements.²⁰ These differences suggest that the emission of DH $\text{Ga}_x\text{In}_{1-x}\text{As}_y\text{P}_{1-y}$ /InP diode lasers is due to a band-impurity transition. In particular, they are consistent with a transition between the conduction band and Zn acceptors, which are reported to have an ionization energy of 43 meV (Ref. 21). Although the active regions in these devices are doped with Sn donors during LPE growth, Zn is probably the dominant impurity, since electron-beam-induced-current measurements on lasers with even thicker active regions indicate that these regions are p-type, presumably due to diffusion of Zn during growth of the upper InP barrier layer.

J. J. Hsieh
M. C. Finn
C. C. Shen

REFERENCES

1. I. F. Johnson, H. J. Guggenheim, and R. A. Thomas, *Phys. Rev.* **149**, 179 (1966).
2. O. Kubaschewski, E. L. Evans, and C. B. Alcock, *Metallurgical Thermochemistry* (Pergamon Press, Oxford, England, 1967), p. 413.
3. T. C. Ehlert, R. A. Kant, and J. L. Margrave, *J. Am. Chem. Soc.* **86**, 5093 (1964).
4. H. J. Guggenheim, *J. Appl. Phys.* **34**, 2482 (1963).
5. T. B. Reed and R. E. Fahey, *Rev. Sci. Instr.* **37**, 59 (1966), DDC AD-633183.
6. J. Ferguson, H. J. Guggenheim, H. Kamimura, and Y. Tanak, *J. Chem. Phys.* **42**, 775 (1965).
7. J. S. Escher, G. A. Antypas, and J. Edgecumbe, *Appl. Phys. Lett.* **29**, 153 (1976).
8. J. J. Hsieh, J. A. Rossi, and J. P. Donnelly, *Appl. Phys. Lett.* **28**, 709 (1976), DDC AD-A028550/2.
9. C. C. Shen, J. J. Hsieh, and T. A. Lind, *Appl. Phys. Lett.* **30**, 353 (1977).
10. J. J. Hsieh, *J. Cryst. Growth* **27**, 49 (1974), DDC AD-A008298/2.
11. J. J. Hsieh, M. C. Finn, and J. A. Rossi, Symposium on GaAs and Related Compounds, St. Louis, Missouri, 27 September 1976 (to be published); Solid State Research Report, Lincoln Laboratory, M.I.T. (1976:4), p. 36, DDC AD-A039175.
12. G. A. Antypas and J. Edgecumbe, *J. Cryst. Growth* **34**, 132 (1976).
13. G. A. Antypas and L. Y. L. Shen, Symposium on GaAs and Related Compounds, St. Louis, Missouri, 27 September 1976 (to be published).
14. R. Sankaran, R. L. Moon, and G. A. Antypas, *J. Cryst. Growth* **33**, 271 (1976).
15. H. Nagai and Y. Noguchi, *Appl. Phys. Lett.* **29**, 740 (1976).
16. K. Weiser and R. S. Levitt, *Appl. Phys. Lett.* **2**, 178 (1963).
17. I. Ismailov, A. Sadiev, R. Altynbaev, and N. Shokhudzhaev, *Sov. J. Quant. Electron.* **5**, 451 (1975).
18. G. M. Blom and J. M. Woodall, *Appl. Phys. Lett.* **17**, 373 (1970).
19. T. Y. Wu and G. L. Pearson, *J. Phys. Chem. Solids* **33**, 409 (1972).
20. W. J. Turner, W. E. Reese, and G. D. Pettit, *Phys. Rev.* **136**, A1467 (1964).
21. E. W. Williams, W. Elder, M. G. Astles, M. Webb, J. B. Mullin, R. Straughan, and P. J. Tufton, *J. Electrochem. Soc.* **120**, 1741 (1973).



IV. MICROELECTRONICS

A. CHARGE-COUPLED DEVICES (CCDs): PROGRAMMABLE TRANSVERSAL FILTER

In preceding reports^{1,2} a high-speed CCD programmable transversal filter structure was described. In the prototype version, the digital reference was set by external switches. In the version which is now being fabricated, the reference is to be stored on-chip in n-channel MOS shift registers. During the past quarter, processing experiments have been completed to determine the optimum channel-stop implants and field-oxide growth conditions so that the fabrication process will be suitable for both the CCDs and the MOS transistors.

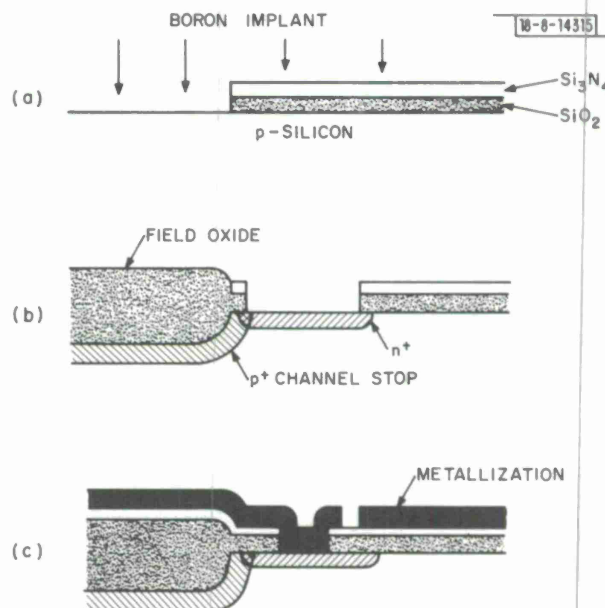


Fig. IV-1. Sequence of steps used to form n-channel MOS transistor for shift registers. In (a), an $\text{SiO}_2/\text{Si}_3\text{N}_4$ layer is used as an implant mask for channel stop, and (b) same layer is an oxidation mask for thick field oxide. n^+ diffusion for source and drain is then made. In (c), the original $\text{SiO}_2/\text{Si}_3\text{N}_4$ layer has been removed and new gate SiO_2 is grown and capped with Si_3N_4 layer. Contact and metallization steps complete this device.

Figure IV-1(a-c) illustrates the sequence of those steps which form the enhancement-mode MOS transistors. An $\text{SiO}_2/\text{Si}_3\text{N}_4$ layer is patterned by photolithography to delineate the channel-stop regions, and the wafer is implanted with boron to form the channel stop as shown in Fig. IV-1(a). The $\text{SiO}_2/\text{Si}_3\text{N}_4$ film serves both as an implantation mask and as an oxidation mask during the prolonged oxidation which forms the thick field oxide shown in Fig. IV-1(b). As a result, the channel stop and field oxide are automatically aligned. In order to minimize area requirements for these devices, it is standard practice to allow the n^+ source and drain diffusion to abut the p^+ channel stop. This contrasts with our previous practice of allowing 0.3 mil spacing between the two. Under these circumstances, the junction breakdown voltage can be unacceptably low unless the p^+ dopant level is carefully controlled. This strong dependence is shown in Fig. IV-2 where the breakdown voltage of a one-sided step junction is plotted as a function of the doping concentration on the lightly doped side of the junction.³ An additional constraint on the channel-stop doping is that it must be high enough to prevent unwanted conducting channels from forming under the field-oxide regions. The metallization which runs over the field-oxide

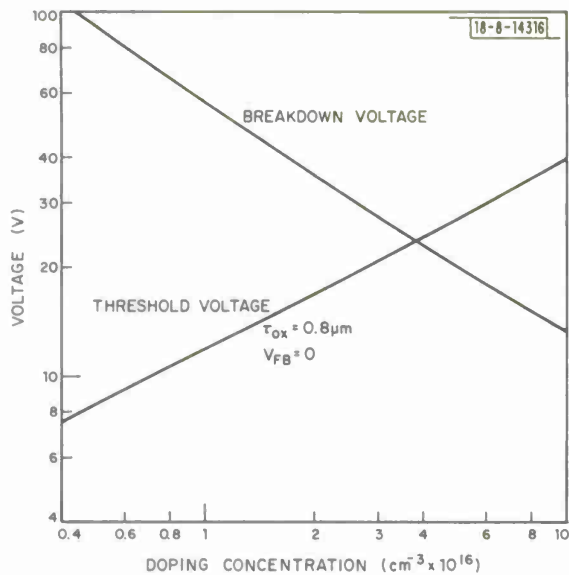
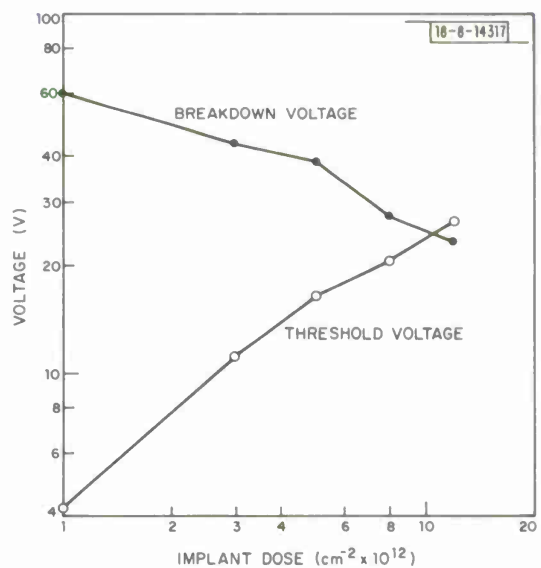


Fig. IV-2. Plot of breakdown voltage of one-sided step junction and of threshold voltage for $0.8\text{-}\mu\text{m}$ oxide having $V_{\text{FB}} = 0$ as a function of doping level of substrate.

Fig. IV-3. Measured values of breakdown and threshold voltages on MOSFETs with boron-implanted channel stops. Ordinate is boron-implant dose, and implant was done at an energy of 200 keV.



regions [Fig. IV-1(c)] can invert the channel stop if the metal has a bias greater than the threshold voltage V_T given by⁴

$$V_T = V_{FB} + 2\phi_{FP} + \frac{(4\epsilon_s q N_A \phi_{FP})^{1/2}}{C_o} \quad (IV-1)$$

where V_{FB} is the flatband voltage, C_o is the oxide capacitance per unit area, ϕ_{FP} is the Fermi potential in the p-channel stop, ϵ_s is the permittivity of the silicon, q is the charge on the dopant, and N_A is the dopant concentration. This equation is plotted in Fig. IV-2 for the case $V_{FB} = 0$ and an oxide thickness of 0.8 μm . The two curves in this figure define the range of acceptable channel-stop dopant levels. The calculations show that a concentration of $3.8 \times 10^{16} \text{ cm}^{-3}$ will result in an optimum condition where both breakdown and threshold voltages are 24 V.

Experiments were first performed to determine if the 0.8- μm field oxide could be grown with a suitably low flatband voltage. The 0.8- μm thickness was chosen as a compromise between a minimum step between the gate and field oxides and an oxide thick enough so that high values of V_T could be easily achieved. A 4-hr steam oxidation at 1000°C followed by an 1100°C gate oxidation process consisting of 18 min. dry O_2 plus 3% HCl and 15 min. N_2 anneal gave $V_{FB} = -4 \text{ V}$, a value sufficiently small to obtain the required values of V_T .

A second experiment was performed to determine the optimum implant dose. A problem with the oxidation process described above is that during the prolonged oxidation the boron implant can be consumed by the oxide. To avoid this, the boron was implanted at the maximum available energy of 200 keV, placing it at a projected range about 0.65 μm into the silicon. The steam oxidation temperature was chosen to minimize thermal diffusion of the implant and keep it well away from the oxide-silicon interface. During subsequent heat treatments, oxide growth was either very slow or inhibited by an Si_3N_4 layer applied after the gate oxidation.

An analytic solution exists⁵ for the calculation of an implant profile capped with an oxide after an annealing step in a non-oxidizing ambient, and this was used to estimate the implant dose needed to achieve the desired acceptor concentration at the surface. Test MOSFETs were fabricated using a range of implant doses from 1×10^{12} to $1.2 \times 10^{13} \text{ cm}^{-2}$ and having field oxides under the gates. The measured values of breakdown and threshold voltages are shown in Fig. IV-3, and suggest that the optimum condition of 24-V threshold and breakdown voltages can be met with an implant dose of about $1 \times 10^{13} \text{ cm}^{-2}$. Since we estimate the required operating voltage for these devices (which must be less than both the breakdown and threshold voltages) to be no more than 15 V, the results of Fig. IV-3 show that a fairly broad range of implant doses will satisfy this requirement.

B. E. Burke	D. J. Silversmith
A. M. Chiang	R. W. Mountain
D. L. Smythe, Jr.	

B. CHARGED-COUPLED DEVICES: IMAGERS

Fabrication of several wafers of the 100- \times 400-cell CCD imaging devices for the GEODSS (Ground Electro-Optical Deep Space Surveillance) Program has been proceeding for several months. The latest run of six wafers is partially completed, and static tests to date on three wafers have demonstrated an overall yield of 14 percent.

The first device run, described in a previous report (see p. 53 in Ref. 1), consisted of devices fabricated through the interconnect metallization step which was sufficient for complete

electrical evaluation. Two additional masking steps are required for the final device and have been incorporated in the recent device runs. These steps are part of a process to create an integral light shield for the input and output registers and the output circuitry. The procedure consists of first depositing a 1.5- μm layer of phosphorous-doped SiO_2 on the finished wafer, a standard practice for providing a protective coat for integrated circuits. A second level of aluminum is subsequently deposited and patterned to form the light shield. The final masking step opens the phosphorous glass over the bonding pads. It is desirable that the glass be relatively thick in order to minimize the capacitance between the light shield and the output circuitry. Three wafers have been fabricated with this process, and a total of 12 devices out of 84 passed a DC probe test. These good devices will undergo dynamic electrical testing using drive circuitry mounted on a probe card. Devices which pass the dynamic test will be used to assemble a 2-chip prototype version of the hybrid imaging array described previously.⁶

B. E. Burke W. M. McGonagle
R. W. Mountain D. J. Silversmith

C. A TWO-LEVEL INTERCONNECT SYSTEM FOR CERAMIC HYBRID INTEGRATED-CIRCUITS' SUBSTRATES UTILIZING ALUMINUM-SILICON DIOXIDE-ALUMINUM

The integration of large numbers of complex, monolithic integrated circuit chips onto a single substrate often requires interconnects with two levels of metallization. It must be possible to have a high density of interconnects on both levels, adequate isolation between levels, and compatibility with the die-attach and wire-bond techniques that will be used in the assembly process. A technology has been developed which uses sputtered aluminum for both the top and bottom metallization levels, and either sputtered or chemical-vapor-deposited (CVD) silicon dioxide for the isolation between levels. The aluminum metallization is, of course, compatible with aluminum-wire ultrasonic bonding from chip to substrate, and can be used with epoxy die-attach. We have implemented two complex hybrid circuits with this technique: one an 8- \times 8-bit multiplier (see p. 61 in Ref. 1) utilizing eight commercially available 4- \times 2-bit multiplier chips on a 1- \times 1-in. substrate, the other a 16-chip CCD sensor array⁷ on a 2.1- \times 2.1-in. substrate. A detailed description of the fabrication process for the substrates for these two circuits will be given, and the particular problems associated with each discussed.

The ceramic blanks used in this process are 99.5-percent alumina with either an as-fired finish of from 3 to 4 $\mu\text{in.}$ or a polished finish of from 1 to 2 $\mu\text{in.}$ The as-fired substrates were used exclusively for the 1- \times 1-in. multiplier substrate, and both types were used for substrates for the CCD sensor, with the polished finish yielding somewhat better results. The blank substrates are cleaned in a hot, ultrasonically agitated detergent solution, and rinsed in flowing ultrasonically agitated DI water. After rinsing, the substrates are blown dry with clean, dry nitrogen and loaded into the sputtering chamber. Then, 1 μm of aluminum is deposited at 650 $\text{\AA}/\text{min.}$ using a conventional RF-diode sputtering unit with a power density of 1.6 W/cm^2 , a target-to-substrate spacing of 5.7 cm, and argon pressure of 1.33 Pa, and an argon flowrate of 50 scc/min. The aluminum is then photolithographically patterned using Shipley 1350J positive photoresist and an aluminum etch consisting of 970 parts phosphoric acid, 10 parts nitric acid, 30 parts water, and 1 g copper sulfate per liter of solution. The minimum line and spacing for both circuits is 0.13 mm.

The next step in the fabrication process is the deposition of the silicon dioxide which will isolate the two levels of aluminum. This has been done by sputtering, by low-temperature CVD,

and by a combination of both processes, resulting in a duplex film. However, whichever oxide deposition process is used, the preparation of the substrate for deposition is critical if reliable isolation is to be achieved. The only technique we found to be completely effective in removing all debris from the substrate after aluminum photolithography is to strip the resist with acetone, and then clean the substrate using a commercial wafer scrubber. The scrubber first sprays both the spinning substrate and a nylon brush with a dilute solution of ammonium hydroxide and detergent in water, and then scrubs the surface of the substrate with the brush. This procedure is repeated using DI water, and finally the substrate is sprayed with DI water and spun dry. At this point, the substrate is loaded into either the CVD reactor or the sputtering chamber for the deposition of $1.5\text{ }\mu\text{m}$ of silicon dioxide.

The sputtered oxide is deposited using the same parameters described above for the aluminum film except that the power is increased to 2.4 W/cm^2 at the SiO_2 cathode with a resulting rate of $125\text{ }\text{\AA}/\text{min}$. Also, the substrate is floated on a 0.76-mm -thick glass plate, which allows the substrate surface to reach temperatures in excess of 250°C during sputtering. The $1.5\text{ }\mu\text{m}$ of CVD oxide is deposited at approximately $1600\text{ }\text{\AA}/\text{min}$, using a substrate temperature of 450°C , a 5-percent silane-in-argon mixture flowing at 870 cc/min , O_2 flowing at 1510 cc/min , and N_2 as a carrier gas flowing at 40 l/min . The duplex films were deposited using the above parameters for both processes, depositing $0.75\text{ }\mu\text{m}$ of oxide by one process and then the other.

The evaluation of the substrates showed that both sputtering and CVD were capable of producing an oxide film that provided adequate isolation. However, the CVD film was clearly superior and had the very significant added advantage of being able to coat several substrates in a 1-hr run vs one substrate in 3 hr in the sputtering system. The duplex films offered no advantage over the CVD film and, therefore, were not further developed.

After depositing the isolation oxide, the via holes are etched using conventional photolithography. The substrate is coated with Kodak 747 photoresist exposed, developed, and baked at 120°C . This procedure is then repeated with a second coating of photoresist, and the vias opened with a commercial, buffered-HF etch. This second photoresist coating is necessary to prevent microscopic defects in the mask from creating pinholes in the oxide. Ideally, a second mask should be used with identical geometries but a different distribution of random defects. However, we found that the inevitable slight misalignment of the same mask from the first to the second exposure gives us the same effect. The oxide typically etches in from 5 to 6 min. Etching is terminated by observing the substrate in the buffered-HF under a low-power microscope, and noting when the aluminum at the bottom of the vias is being uniformly attacked over the entire substrate area.

After etching the vias, the photoresist is stripped, the substrates cleaned, and $1\text{ }\mu\text{m}$ of aluminum sputtered over the oxide using the parameters described above. This aluminum is then etched with the appropriate mask, the resist stripped, and the aluminum sintered at 500°C in N_2 for 15 min. Figures IV-4(a) and (b) and IV-5(a) and (b) show a CCD sensor substrate and a multiplier substrate, respectively. The CCD sensor substrate provides an especially rigorous test. A ground plane formed in the top-level metallization covers all the bottom-level metallization except in those small areas where wire bonds will be made and small discrete chips mounted as part of the buffer circuitry for each CCD chip [see Fig. IV-4(b)]. Thus, any defect in the isolation oxide which coincides with a line in the bottom level would result in a short to ground. On the multiplier substrate, a defect would have to coincide with a crossover to cause a short.

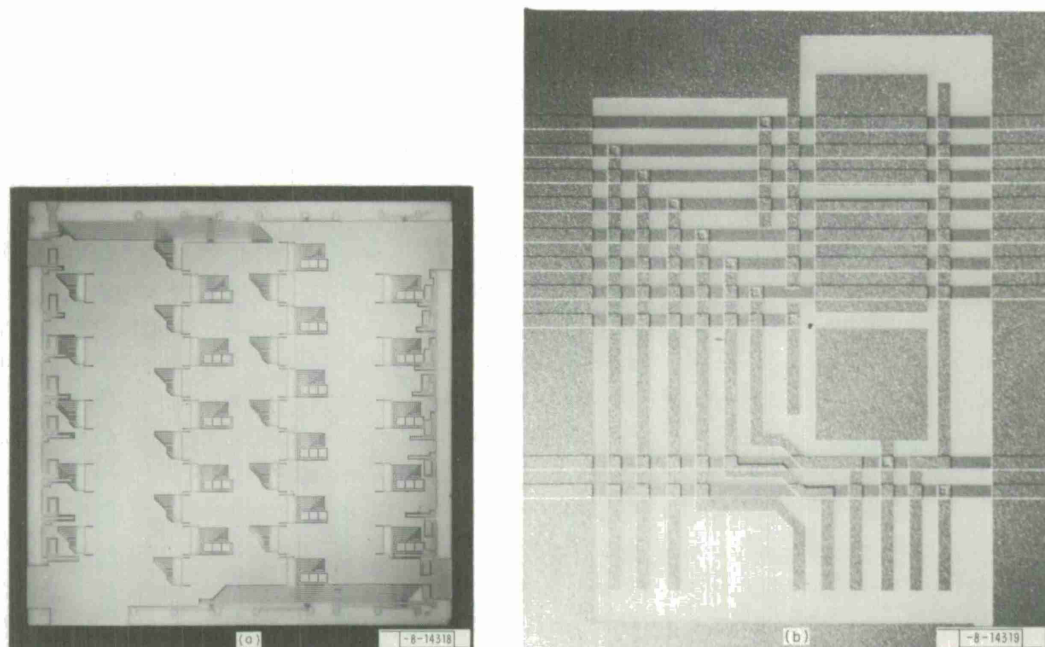


Fig. IV-4. (a) Interconnect substrate for 16-chip, CCD sensor array for GEODSS Program. Ceramic is $2.1 \times 2.1 \times 0.025$ in., 99.5-percent alumina polished to 1- to 2- μ in. surface finish. (b) Expanded view of bonding pad and transistor mounting pad area showing crossovers and vias. Area is surrounded by ground plane.

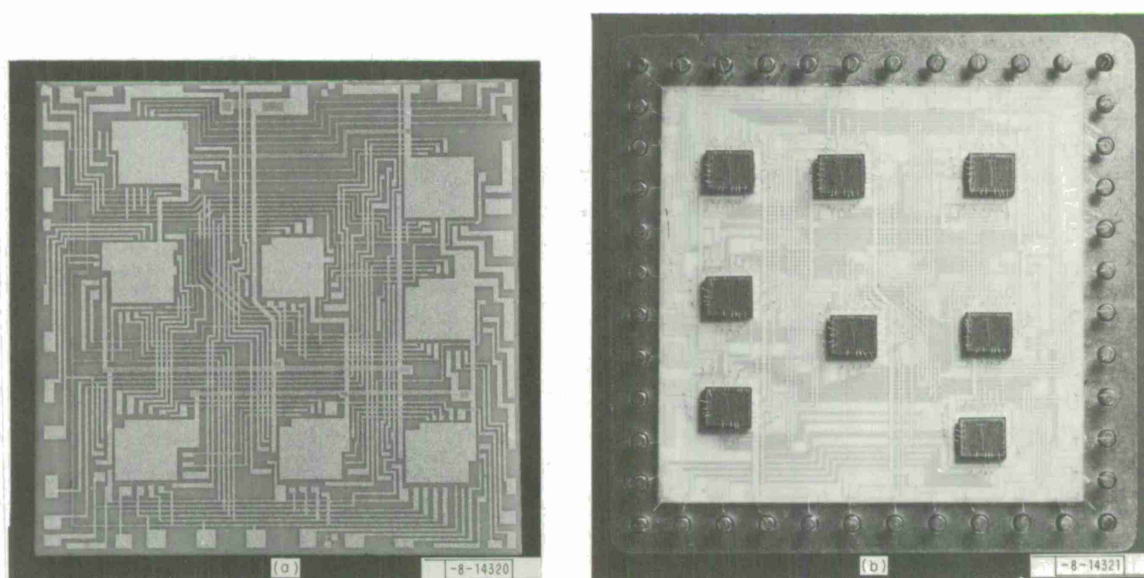


Fig. IV-5. (a) Two-level interconnect substrate for 8- \times 8-bit multiplier circuit with 16-bit output ceramic substrate is $1 \times 1 \times 0.025$ in., 99.5-percent alumina. (b) Completed circuit with eight 4- \times 2-bit multiplier chips mounted and wire-bonded. Substrate is mounted in flatpack and wire-bond interconnects made from the substrate to package pins.

Fortunately, the interconnections of the CCD sensor substrate are such that every line can be 100-percent tested for continuity, and for isolation from the other lines which it crosses and from ground. Testing of several substrates revealed that a typical substrate with CVD oxide would have from 2 to 5 shorts (typically to ground), and those substrates with sputtered oxide would have from 5 to 10 shorts. Continuity is not a problem. However, these shorts are almost always repairable (as described below), so that a large number of good substrates were fabricated. Later, using polished blanks with a 1- to 2- μ in. surface finish and CVD oxide, a substrate with no shorts was made, and indications are that producing substrates with at most one or two repairable defects will be routine.

Shorts whose resistance was ≥ 2 ohms could be eliminated using a simple technique on a curve tracer. Shorts with resistance < 2 ohms required too much power to eliminate, and either the line or the contact point of the probe would vaporize when the short was current-pulsed. Substrates with these low-resistance shorts were discarded. To eliminate a repairable short, the probes were located so that the total resistance between probes including the short was ≤ 10 ohms. The short was then pulsed with currents up to but not exceeding 1.5 A. After eliminating the short, the substrate was retested electrically, and visually inspected under a low-power microscope to insure that no damage had been done either to the metallization or the oxide. Approximately 50 percent of all substrates on both types of ceramic and with both sputtered and CVD oxide could be repaired. However, with the use of 1- to 2- μ in. polished substrates and CVD oxide, the yield was near 100 percent.

The multiplier substrate presented another problem because 100-percent testing is impossible. However, significant spot-checking for shorts and continuity is possible, and by discarding any substrate with even a single defect, those substrates committed to final assembly could be assumed to be perfect with a high level of confidence. The only method of completely testing the substrate is by testing the completed circuit [Fig. IV-5(b)], and not enough of these were made to give meaningful yield data. However, none of the substrates committed to final assembly were defective.

In summary, a technology has been developed for fabricating alumina interconnect substrates for hybrid integrated circuits which provides two levels of aluminum metallization separated by an insulating film of silicon dioxide. Best results were obtained when using 99.5-percent alumina substrates polished to a surface finish of 1 to 2 μ in., and by depositing the oxide using low-temperature CVD techniques. Substrates for an 8- \times 8-bit high-speed multiplier and a 16-chip CCD sensor array were fabricated with a high yield, and techniques were developed for repairing shorts without damage to the metallization or isolating dielectric.

F. J. Bachner	W. L. McGilvary
W. H. McGonagle	C. L. Doherty, Jr.
G. H. Foley	

REFERENCES

1. Solid State Research Report, Lincoln Laboratory, M.I.T. (1976:4), pp. 56-61, DDC AD-A039175.
2. Ibid. (1977:1), p. 29.
3. R. M. Warner, Jr. and J. N. Fordemwalt, Eds., Integrated Circuits: Design Principles and Fabrication (McGraw-Hill, New York, 1965), p. 67.
4. A. S. Grove, Physics and Technology of Semiconductor Devices (Wiley, New York, 1967), p. 333.
5. E. C. Douglas and A. G. F. Dingwall, IEEE Trans. Electron Devices ED-21, 324 (1974).
6. Solid State Research Report, Lincoln Laboratory, M.I.T. (1975:4), p. 46, DDC AD-A025489/6.
7. Ibid. (1976:2), p. 47, DDC AD-A030861/9.

V. SURFACE-WAVE TECHNOLOGY

A. POLYIMIDE-MEMBRANE X-RAY-LITHOGRAPHY MASK

X-ray-lithography masks consist of an absorber pattern on a thin membrane that is relatively transparent (i.e., ≤ 3 dB attenuation) to soft x-rays. Several materials have been used as transmitter membranes including: silicon (Refs. 1 and 2), Al_2O_3 (Refs. 3 and 4), $\text{SiO}_2/\text{Si}_3\text{N}_4$ (Refs. 5 and 6), mylar,⁷ and polyimide.⁸

We describe here a recently developed process for fabricating polyimide-membrane x-ray-lithography masks with thicknesses ranging from 0.5 to several micrometers. The process produces large-area rugged x-ray masks suitable for use at the $13.3\text{-}\text{\AA}$ Cu_L wavelength, as well as at the $44.7\text{-}\text{\AA}$ C_K and $8.34\text{-}\text{\AA}$ Al_K wavelengths. The polyimide surface is optically smooth, and the membrane is transparent to visible radiation. This latter feature enables it to be used with a newly developed interferometric alignment apparatus.⁹

In the first step of the process, a glass substrate is coated with a film of polyamic acid (Dupont product PI-2530) using a conventional spinning technique. Thicknesses of 0.5 to 5 μm are readily obtained by varying the spin speed and/or the dilution of the polyamic acid. For a film thickness of 1 μm , a dilution of 4 parts PI-2530 in 1 part N-methyl-2-pyrrolidone and 1 part acetone, and a spin speed of 6000 rpm are used. The polyamic acid is converted to polyimide by curing at 150°C for 15 min., and at 250°C for 60 min. The desired x-ray-absorber pattern is then formed in gold on top of the polyimide by using any lithographic means such as photolithography, electron-beam, or holographic lithography. An important feature of the process is that the polyimide membrane remains attached to a glass substrate during fabrication of the absorber pattern. The glass serves as a heat sink and thus avoids the problem of heating during ion-beam etching or other processes. The polyimide is relatively inert and stands up to most chemical-etching environments.

A support ring and a copper tube are bonded to the polyimide using epoxy as indicated in Fig. V-1(a). The glass substrate is then etched by immersing the assembly in a solution of hydrofluoric acid as shown in Fig. V-1(b). During etching, the copper tube is filled with isopropyl alcohol to provide a positive pressure against the polyimide and to prevent damage from entry of acid through pinholes or diffusion through the membrane. After etching of the glass substrate, the support ring is separated from the copper tube by cutting the polyimide between the two. Figure V-2 is a cross-sectional schematic of a completed x-ray mask. The aluminum contact is evaporated onto the mask after the glass etching. It acts as an infrared reflector and as an electrical contact in an electrostatic mask-contacting scheme.

We are in the process of measuring the inhomogeneous distortion of patterns on polyimide membranes using moiré and angle-of-diffraction methods. For many applications, this distortion should be less than 1 part in 10^5 , which is a difficult specification to meet. These measurements will be covered in a future report.

D. C. Flanders
H. I. Smith
M. Dalomba

B. INTEGRATING CORRELATOR

A new surface-acoustic-wave (SAW) device which has been under investigation is the integrating correlator. The basic operation of this device, as shown in Fig. V-3, is similar to a

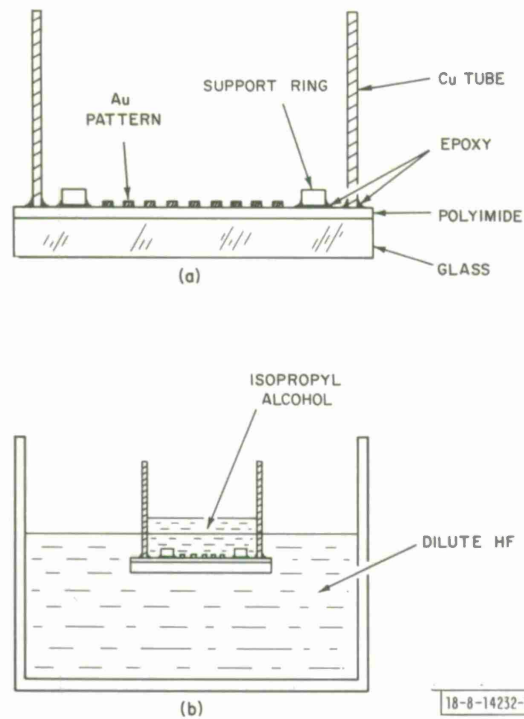


Fig. V-1. Fabrication of a polyimide-membrane x-ray-lithography mask. (a) Cross-sectional illustration showing support ring and copper tube bonded to polyimide membrane. (b) Method used to protect absorber pattern during etching of glass substrate under polyimide membrane.

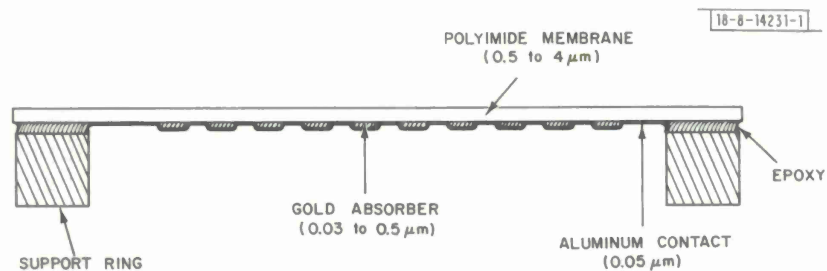


Fig. V-2. Cross-sectional illustration of polyimide-membrane x-ray-lithography mask.

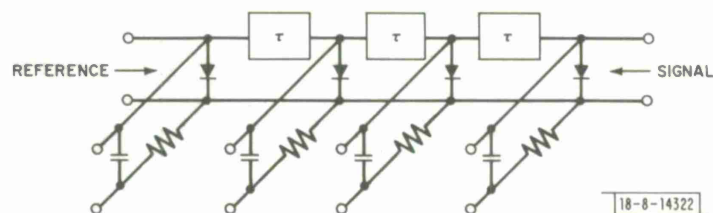


Fig. V-3. Schematic diagram of circuit which yields equivalent of a number of correlation receivers operating in parallel. In this example, four receivers operate in parallel.

correlation receiver.¹⁰⁻¹² An incoming signal and a locally generated reference waveform, both centered at frequency ω_0 , are launched into the delay line from opposite ends. Every point along the delay line represents a different differential delay between signal and reference, and the distributed diodes provide nonlinear mixing of the two waves. The local product signal generated by the mixing action is integrated over time by each of the diodes. At the end of the correlation interval or integration time, the integrated charge in each diode capacitance represents a point of the correlation function between signal and reference. The spatial distribution of the integrated charge represents a segment of the correlation function. This spatial distribution can be read out in time by sequentially addressing each of the output taps. Such a device performs the function of a large number of correlation receivers operating in parallel.

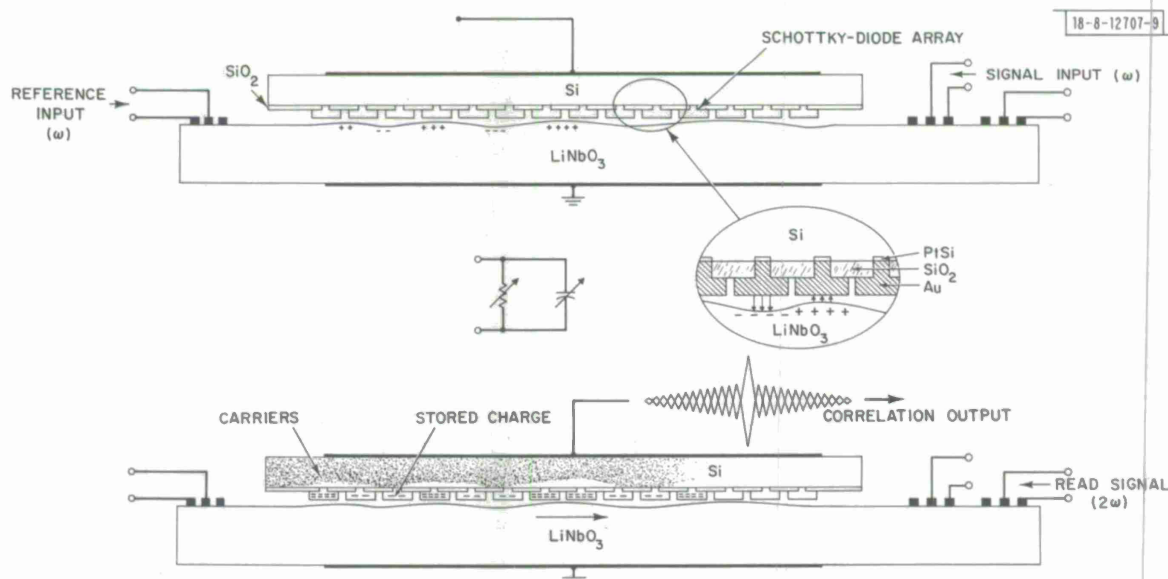


Fig. V-4. Schottky-diode integrating correlator. Upper: mixing and integration for signal and reference at frequency ω . Lower: readout of correlation with short readout signal at 2ω .

The SAW integrating correlator is shown in Fig. V-4. The SAW delay line provides the varying differential delay for reference and signal, while the Schottky-diode array held in close proximity ($\sim 300\text{-}\mu\text{m}$ gap) to the delay line provides the nonlinear mixing of the two counterpropagating SAWs. Under conditions of reverse bias, either resulting from a voltage pulse prior to the mixing or from their own self-biasing behavior, the diodes can be modeled as a parallel RC network. Thus, each diode is capable of performing its own integration function and can retain the stored charge for up to 100 msec (corresponding to dark currents of about 30 nA/cm^2) after the reference and signal are terminated. After integration, the resultant stored charge on the diodes produces a depth modulation in the depletion layer of the silicon. When this depth modulation is interrogated with a short SAW burst generated at one end of the delay line, the correlation function between reference and signal appears across the silicon.

The spatial periodicity of the stored charge is $\lambda_0/2$, and hence the interrogating acoustic wave must have a frequency of $2\omega_0$. In order that sufficient samples be taken so as to properly

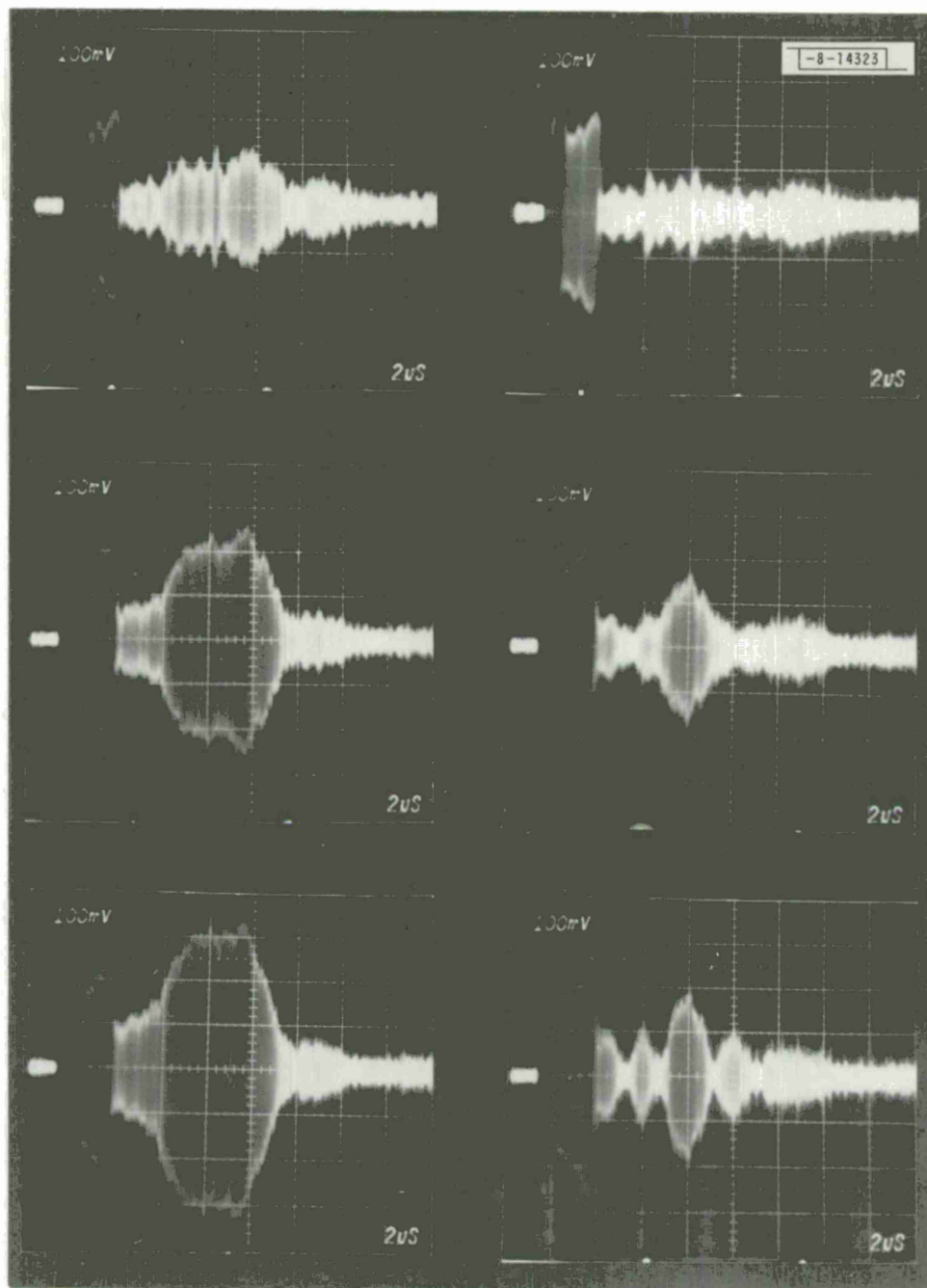


Fig. V-5. Response of integrating correlator. Left: autocorrelation of two CW bursts. Right: autocorrelation of a 3-chip code. Photos from top to bottom are for 1, 10, and 100 integrations, respectively.

reconstruct the correlation function, the diodes should be spaced $\leq \lambda_0/4$. For a reference and signal input at 100 MHz, this corresponds to a periodicity of approximately 8 μm for an LiNbO_3 delay line.

Experiments have been performed to verify the operation of the device using a diode array with a periodicity of 3.8 μm which was prepared for a memory correlator.¹³ In the experiments, the actual integration process was observed, and a method of controlling the integration time was studied. Figure V-5 shows the autocorrelation functions generated by two different waveforms. On the left-hand side of the figure, 10- μsec bursts of 70-MHz signal and reference were repeatedly entered into the device. On the right-hand side, a simple 3-bit phase-coded waveform with a 3.3- μsec bit time was used. The integrated correlation function was read by a 3.3- μsec read pulse at 140 MHz after 1, 10, and 100 integrations, reading from top to bottom of the figure. After 10 integrations, the correlation peak of the coded waveforms is beginning to appear, and after 100 integrations the sidelobe structure is evident. The correlation of the CW waveforms fills the entire length of the diode array, which has saturated after about 10 integrations.

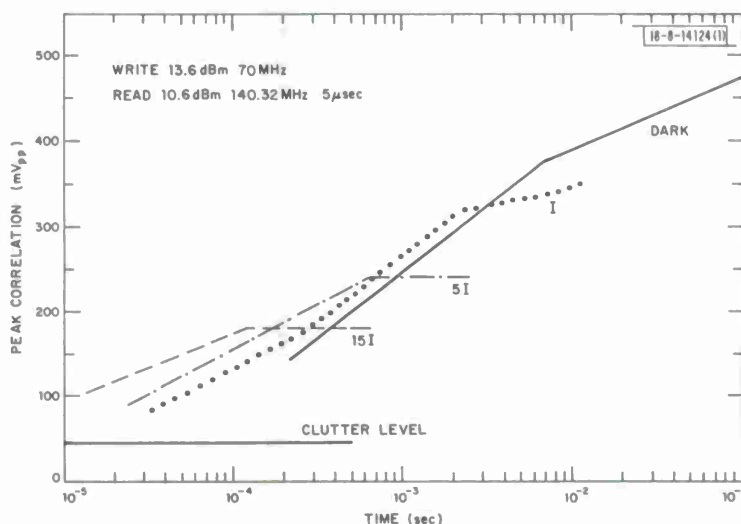


Fig. V-6. Variation of integrating-correlator time constant by varying level of illumination by LEDs. Quantity I is an uncalibrated unit of illumination intensity.

Light can be used to alter the diode resistance and thus control the integration time. The effect of LED illumination on the diodes is shown in Fig. V-6 where it can be seen that the time constant, as indicated by the amount of time required to reach a saturation level, can be varied by about two orders of magnitude by varying the LED illumination. The approximate 6-dB decrease in the output signal with increased illumination is due to the increased acoustoelectric loss resulting from a greater number of carriers in the silicon.

The present device uses a delay line with a bandwidth of 20 MHz which, combined with an integration time of 10 msec, implies potential correlation gain as high as 50 dB. It is desirable to increase the bandwidth to 100 MHz for future devices in order to obtain even greater processing gain. One of the major problems which prevents maximum performance of this device is the

spurious bulk waves produced by both the writing and read signals. The effect of bulk waves is evident as a distortion of the waveforms in Fig. V-6. The elimination of this interference is a major goal for this program.

D. H. Hurlburt
R. W. Ralston
E. Stern

REFERENCES

1. D. L. Spears and H. I. Smith, Solid State Tech. 15, 24 (1972), DDC AD-759257.
2. S. E. Bernacki and H. I. Smith, IEEE Trans. Electron Devices ED-22, 421 (1975), DDC AD-A016697/5.
3. P. A. Sullivan and J. H. McCoy, IEEE Trans. Electron Devices ED-23, 412 (1976).
4. T. Funayama, Y. Takayama, T. Inagaki, and M. Nakamara, J. Vac. Sci. Technol. 12, 1324 (1975).
5. R. Feder, E. Spiller, and J. Topalian, J. Vac. Sci. Technol. 12, 1332 (1975).
6. Solid State Research Report, Lincoln Laboratory, M.I.T. (1976:3), p. 51, DDC AD-A034647/8.
7. D. Maydan, G. A. Coquin, J. R. Maldonado, S. Somekh, D. Y. Lou, and G. N. Taylor, IEEE Trans. Electron Devices ED-22, 429 (1975).
8. J. S. Greeneich, IEEE Trans. Electron Devices ED-22, 434 (1975).
9. S. Austin, D. C. Flanders, and H. I. Smith, "A New Interferometric Technique for Multiple-Mask Alignment," Proc. 14th Symp. on Electron Ion and Photon Beam Technology, 25-27 May 1977, Palo Alto, California.
10. O. Menager and B. Desormiere, Appl. Phys. Lett. 27, 1 (1975).
11. B. J. Darby and J. D. Maines, "The Tapped Delay Line Active Correlator: A Neglected SAW Device," 1975 Ultrasonics Symposium Proceedings (IEEE, New York, 1975), p. 193.
12. J. D. Maines, "Surface Acoustic Wave Devices: Past Successes and Future Prospects," 1974 Ultrasonics Symposium Proceedings (IEEE, New York, 1974), p. 136.
13. Solid State Research Report, Lincoln Laboratory, M.I.T. (1976:4), p. 73, DDC AD-A039175.

UNCLASSIFIED

SECURITY CLASSIFICATION OF THIS PAGE (When Data Entered)

REPORT DOCUMENTATION PAGE		READ INSTRUCTIONS BEFORE COMPLETING FORM	
1. REPORT NUMBER ESD-TR-77-110	2. GOVT ACCESSION NO.	3. RECIPIENT'S CATALOG NUMBER	
4. TITLE (and Subtitle) Solid State Research		5. TYPE OF REPORT & PERIOD COVERED Quarterly Technical Summary 1 February - 30 April 1977	
		6. PERFORMING ORG. REPORT NUMBER 1977:2	
7. AUTHOR(s) Alan L. McWhorter		8. CONTRACT OR GRANT NUMBER(s) F19628-76-C-0002	
9. PERFORMING ORGANIZATION NAME AND ADDRESS Lincoln Laboratory, M. I. T. P. O. Box 73 Lexington, MA 02173		10. PROGRAM ELEMENT, PROJECT, TASK AREA & WORK UNIT NUMBERS Program Element No. 65705F Project No. 649L	
11. CONTROLLING OFFICE NAME AND ADDRESS Air Force Systems Command, USAF Andrews AFB Washington, DC 20331		12. REPORT DATE 15 May 1977	
		13. NUMBER OF PAGES 76	
14. MONITORING AGENCY NAME & ADDRESS (if different from Controlling Office) Electronic Systems Division Hanscom AFB Bedford, MA 01731		15. SECURITY CLASS. (of this report) Unclassified	
		15a. DECLASSIFICATION DOWNGRADING SCHEDULE	
16. DISTRIBUTION STATEMENT (of this Report) Approved for public release; distribution unlimited.			
17. DISTRIBUTION STATEMENT (of the abstract entered in Block 20, if different from Report)			
18. SUPPLEMENTARY NOTES None			
19. KEY WORDS (Continue on reverse side if necessary and identify by block number) <div style="display: flex; justify-content: space-between;"> <div> solid state devices quantum electronics materials research microelectronics </div> <div> surface-wave technology photodiode devices lasers laser spectroscopy </div> <div> imaging arrays infrared imaging surface-wave transducers </div> </div>			
20. ABSTRACT (Continue on reverse side if necessary and identify by block number) <p>This report covers in detail the solid state research work of the Solid State Division at Lincoln Laboratory for the period 1 February through 30 April 1977. The topics covered are Solid State Device Research, Quantum Electronics, Materials Research, Microelectronics, and Surface-Wave Technology. Funding is primarily provided by the Air Force, with additional support provided by the Army, ARPA, NSF, and ERDA.</p>			

DD FORM 1473 EDITION OF 1 NOV 65 IS OBSOLETE
1 JAN 73

UNCLASSIFIED

SECURITY CLASSIFICATION OF THIS PAGE (When Data Entered)

Printed by
United States Air Force
Hanscom Air Force Base
Bedford, Massachusetts

